Antiperovskite Oxide $Sr_{3-x}SnO$: Discovery of Superconductivity and Its Evolution with Deficiency

Ph.D Thesis
2018

Department of Physics, Graduate School of Science,
Kyoto University, Kyoto, Japan

Mohamed Oudah

Abstract

In this thesis, we report the discovery of a new class of oxide superconductors, the antiperovskite oxides[1], and optimize the condition for synthesis of superconducting $Sr_{3-x}SnO$ [2]. We clarify the dependence of superconductivity on deficiency x in $Sr_{3-x}SnO$ [3] and theoretically propose the possibility of topological superconductivity even in deficient samples [1, 4].

Antiperovskite oxides A_3BO (A = Mg, Ca, Sr, Ba, Yb, Eu; B = Si, Ge, Sn, Pb) have recently been demonstrated to exhibit Dirac electronic dispersion near the Γ point in the Brillouin zone based on first-principles calculations. Charge balance in this class of material, assuming a typical A^{2+} and O^{2-} valences, leads to $(A^{2+})_3(B^{4-})(O^{2-})$, where the B ions have an unusual 4− state. Such negative valance ions are consistent with theoretical calculations. Furthermore, antiperovskite oxides with heavier elements have been predicted as topological crystalline insulators due to the energy inversion of the conduction d band of A^{2+} and the valance p band of B^{4-}. Finding superconductivity emerging in such an unusual electronic state would be interesting and an important step towards understanding of superconductivity in topologically nontrivial materials.

To this goal, we synthesized various antiperovskite oxides, including Ca_3SnO, Ca_3PbO, Sr_3SnO, and Sr_3PbO. These antiperovskite oxides are air-sensitive, so we developed various techniques to handle them during measurements that minimize their exposure to air.

Finally, we discovered the first superconductivity among the antiperovskite oxides in the hole-doped $Sr_{3-x}SnO$ [1] with evidences of zero resistivity and diamagnetic Meissner signal below the critical temperature T_c of 5 K. The initial superconducting samples we synthesized suffered from uncontrolled evaporation of Sr, and it was difficult to quantify the exact composition required for superconductivity.

We overcame this hurdle by modifying various parameters and optimized the synthesis of $Sr_{3-x}SnO$ [2]. With the optimized synthesis, we successfully tuned the amount of strontium deficiency, and the volume fraction of superconductivity at 5 K reached up to 100% with the optimal deficiency of approximately $x = 0.5$ [3]. We calculated band structures of various "$Sr_{2.5}SnO$" and found that the shape of the bands are not altered significantly by the Sr deficiency, but the chemical potential is shifted substantially [4]. Interestingly, this compound exhibits double superconducting transitions with T_c's of approximately 5 and 1 K, as observed in the zero field AC susceptibility measurements [3]. These T_c's at 5 and 1 K do not change significantly as a function of x.

Mössbauer spectra provide some evidence for a Sn^{4-} state in $Sr_{3-x}SnO$, which is the first microscopic evidence for 4− metal ions in antiperovskite oxides. Furthermore, an unusual paramagnetic Meissner effect was observed in some $Sr_{3-x}SnO$ samples. The NMR results reveal an unusual $1/T_1$ behavior for stoichiometric non-superconducting samples, which may originate from the Dirac nature of Sr_3SnO.

We believe these results show that $Sr_{3-x}SnO$ and antiperovskite oxides are strong candidates for investigation of interesting physics. The superconductivity realized in $Sr_{3-x}SnO$ make this class of materials a candidate for future investigation of topological superconductivity.

Contents

List of Figures

List of Tables

Chapter 1

Introduction

In this chapter, I will first stress the impact of discovering a new class of superconductors. Next, I introduce topologically nontrivial materials in general, then discuss theoretical predictions made in the antiperovskite oxides, and briefly review superconductivity in topologically nontrivial materials. Also, the motivation and purpose of this thesis will be presented.

1.1 The Impact of Discovering a New Class of Superconductors

Oxides with perovskite-based structures have played a central role in condensed-matter research for decades. In particular, the discoveries of high-temperature superconductivity in cuprates [5] and unconventional superconductivity in the ruthenate Sr_2RuO_4 [6] have driven the science community to deepen the concepts of strongly correlated electron systems substantially. Sr_2RuO_4 and high T_c cuprates are layered perovskite oxides. The discovery of high temperature superconductivity in iron pnictides [7], another layered material, also played a similar role to the discovery of high T_c in cuprates.

Cubic perovskite oxides, ABO_3 where A and B are metal ions, are the building blocks for layered perovskite oxides. Research efforts have also lead to the discoveries of novel phenomena in cubic perovskite oxides. Examples include colossal magnetoresistance [8], multiferroicity [9], and superconductivity with transition temperature T_c of up to 30 K reported for

$Ba_{0.6}K_{0.4}BiO_3$ [10]. The discovery of high T_c cuprates and iron pnictides initiated work on topics such as strong correlation and multi-orbital effects in d-electron systems. Clarification of the composition dependence of various ordered phases serves as an important basis toward pioneering such novel fields. Indeed, in both copper oxides and iron pinctides, the establishment of composition phase diagrams have been playing key roles in understanding the origin of the superconductivity [11, 12, 13]. These histories tell us that the finding of a new class of oxide superconductors has potential to initiate unexplored research fields.

Perovskite oxides have their counterparts, antiperovskite oxides A_3BO (or "BOA_3"), in which the position of metal and oxygen ions are reversed. Antiperovskite oxides crystalize in cubic or pseudo-cubic structures with reverse occupancy of metal and oxygen relative to their perovskite counterparts. Moreover, a recent study expanded antiperovskite oxides beyond the elements mentioned above [14]. Antiperovskite oxides A_3BO (A = Mg, Ca, Sr, Ba, Eu, Yb and B = Si, Ge, Sn, Pb) have the perovskite crystal structure but with O^{2-} ions occupying the center of the octahedron formed by A^{2+} ions, as illustrated in Fig. 1.1 for Sr_3SnO. To satisfy the charge-neutrality relation, the B ions, Sn in Sr_3SnO, take an unusual 4− oxidation state and, as a consequence, their p orbitals are almost filled [15, 14].

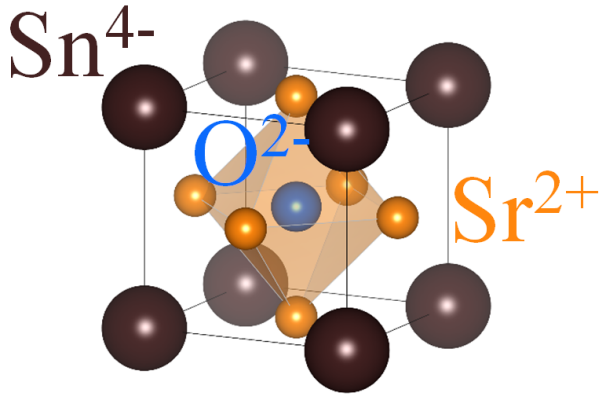

Figure 1.1: Crystal structure of Sr_3SnO with the oxidation state of each atom. Figure produced with VESTA [16].

This unusual electronic configuration can lead to interesting properties. Indeed, theoretical works on Ca_3PbO predicted a 3D Dirac dispersion in the electronic band [17, 18]. This Dirac dispersion originates from the band inversion of the empty Ca-3d and filled Pb-6p bands near the Γ point, as well as from the avoided hybridization between these bands due to crystal symmetry. The Dirac point has a small gap in the order of $\sim$ 10 meV [17], due to higher-order interactions originating from the spin-orbit coupling. This gapped state was later predicted to be a topological cryrstalline insulator state [19]. By changing the A and B ions, one can control the strength of the spin-orbit coupling and band mixing and eventually tune the system from the topologically trivial

insulator to the topological crystalline insulator [20]. The parent compound of this study, Sr_3SnO, is located in the vicinity of the topological transition but is still in the non-trivial regime [19]. Recently, a number of 3D Dirac materials have been extensively studied theoretically and experimentally including Au_2Pb [21], Cd_3As_2 [22, 23] and Na_3Bi [24].

Here, we present the first superconducting antiperovskite oxide Sr_3SnO with the transition temperature of around 5 K. Sr_3SnO possesses Dirac points in its electronic structure, and we propose from a theoretical analysis a possibility of a topological odd-parity superconductivity analogous to the superfluid ^{3}He-B in moderately hole-doped Sr_3SnO. We envision that this discovery of a new class of oxide superconductors will lead to a rapid progress in physics and chemistry of antiperovskite oxides consisting of unusual metallic anions. Also, it was not clear how the superconductivity emerges from the parent 3D Dirac compound with Sr deficiency x. We followed the initial discovery by clarifying the dependence of superconductivity on deficiency x in $Sr_{3-x}SnO$ system and revealed that the optimal x is located around $x = 0.5$.

1.2 Topological Materials

Topological materials are those with band structures that are topologically nontrivial that results in unusual effects in these materials that are invariant under topolgical trasnformation. In recent years, topological effects in materials have come to the spotlight of the condensed matter community after the successful prediction and experimental verification of topological insulating states in materials. In 2016, David J. Thouless, F. Duncan M. Haldane, and J. Michael Kosterlitz were awarded the Nobel Prize in physics “for theoretical discoveries of topological phase transitions and topological phases of matter” [25]. However, topological effects in materials were first experimentaly reported in the 1980’s after the discovery of the quantum Hall effect in silicon based samples by Klaus von Klitzing [26]. This was followed by the theoretical work connecting the quantized conductivity with the quantized charged transport by Robert Laughlin [27], and the effect was further explained based on material topology, lead by theorists such as David Thouless [28]. These initial quantum effects, such as the quantization of the hall conductance, were only observable in the presence of a strong magnetic field, and it was only in 2007 that topological effects in the absence of magnetic field were predicted by two separate groups of theorists [29, 30]. This prediction was made in insulators with heavy elements that have strong interactions between the electrons and atomic nuclei that result in internal magnetic fields in these materials. The electrons on the surface of such materials are in “topologically protected states” that are robust against scattering by defects and nonmagnetic impurities. This theoretically predicted class of materials was referred to as topological insulators, where the bulk dispersion of electrons has a gap but the surface/edge contains gapless states. These gapless surface/edge states are robust and protected against scattering.

Dirac materials are another group of topologically nontrivial materials, and graphene is the most well known example, where the electrons in this 2D material follow the Dirac equations [31].

Dirac electrons appear in topologically nontrivial materials in three instances, either in the bulk states of Dirac semimetals (DSM) and Weyl semimetals (WSM), illustrated in Fig. 1.3, or in the surface/edge states of topological insulators (TI). Both, DSM and WSM, have origins related to the prediction of a substance between metals and dielectrics predicted in 1970, where such a prediction in 3D materials can be described by Dirac equations with four-fold degenerate points [32]. WSM have minimal overlap between the filled and empty bands, where this touching appears at two touching points, called Weyl points, with two-fold degeneracy at each point. The appearance of two-fold degenerate points at two distinct points in the Brillouin zone is a result of the breaking of time-reversal or inversion symmetry [33]. However, where both time-reversal and inversion symmetry are preserved, the Weyl points would occur at the same point, as Kramers pairs, annihilating the Weyl points. In special cases, energetically degenerate Weyl points with opposite charges can be stabilized at the same crystal momentum, where a fourfold degenerecy at a one point singularity. Unlike the case of WSM, where mixing would annihilate points and gap the electronic spectrum, the mixing is forbidden in DSM due to space group symmetry and the nodes remain in the band structure. In graphene, spin-orbit coupling destroys the Dirac points and gaps out the Dirac crossing; however, in DSM's, it survives even in the presence of spin-orbit interactions [34].

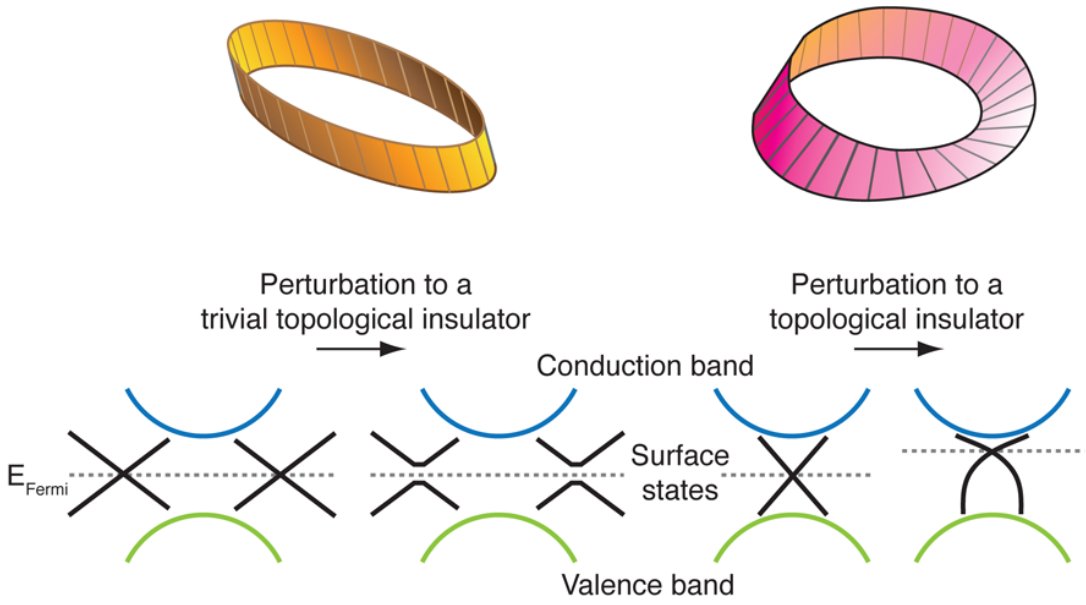

Figure 1.2: Schematic of band structure of topological and trivial insulators [35]. When we think of topology, we normally think of objects that cannot be simply transformed into each other such as a rubber band or a Möbius strip (top). The metallic surface of a topological insulator is different from an ordinary surface because its metallic nature is protected by certain symmetry invariants. In this sense, it cannot be simply transformed into the surface of a normal insulator. The sketches (bottom) show the electronic structure (energy versus momentum) for a "trivial insulator (left) and a strong topological insulator (right). In both cases, there are allowed electron states (black lines) introduced by the surface that lie in the bulk band gap (the bulk valence and conduction bands are indicated by the green and blue lines, respectively). In the trivial case, even a small perturbation (e.g., changing the chemistry of the surface) can open a gap in the surface states, but, in the nontrivial case, the conducting surface states are protected. Note that in the topological insulator, the surface states are linear in momentum and meet at an odd number of points in the k-space.

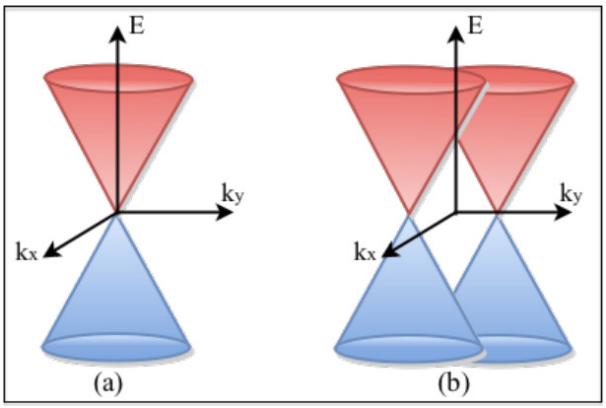

Figure 1.3: Linearized band dispersion of (a) Dirac and (b)Weyl semimetals [36].

In contrast to conventional insulators where the bands are separated by a gap around the Fermi level, topological insulators are those with gaps in the bulk but with surface states that cross the Fermi level. Topological insulators that arise from crystal symmetry rather than time-reversal-symmetry are called topological crystalline insulators (TCI's). These are relevant to the theoretical work performed on the antiperovskite oxides described in 1.2.2. However, formalism of topological insulators and topological crystalline insulators are discussed in more detail in Chap. 2.

1.2.1 Superconductivity in Topologically Nontrivial Materials

The prediction of topological superconductivity was made in a heterostructure of topological insulator in proximity to an *s*-wave superconductor [37]. This section addresses superconductivity found in topologically nontrivial materials, but whether this superconductivity is topological in nature is not always certain. In some of these materials, the topological nature of the band structure was proven from observation of surface states using angle-resolved photoemission spectroscopy (ARPES). The superconductivity in these materials is proven, but whether the superconductivity originates from the surface states is still under progress. This may be due to the low T_c of these materials or that superconductivity appears under pressure, which limits the number of techniques that can be used to probe the superconducting state. Techniques such as ARPES, can directly probe the band structure of a material. Materials with topologically nontrivial band structure that exhibit superconductivity include Bi_2Se_3, Cd_3As_2, WTe_2, and Au_2Pb [38, 39, 23, 40, 21].

In this section, the work on Bi_2Se_3 class of materials will be briefly presented. The superconductivity in other topologically nontrivial materials will be further discussed in 2.2.4.2. The structure of Bi_2Se_3 is composed of a 2D layer of Bi sandwiched between two Se layers, and this Se-Bi-Se layers are stacked along the *c* direction such that the Se and Se layers are connected through van der Waals forces [38]. The surface states in Bi_2Se_3 were demonstrated through

ARPES measurements, shown in Fig. 1.4, and the case for Bi_2Se_3 being a topological insulator was clear prior to any sign of superconductivity. This initial work on the parent compound included related work on Sb and Te substitution for Bi and Se, respectively. The work by people in different fields had established methods for synthesizing and handling these materials, and driven by promising properties of these materials, such as their favorable thermoelectric properties.

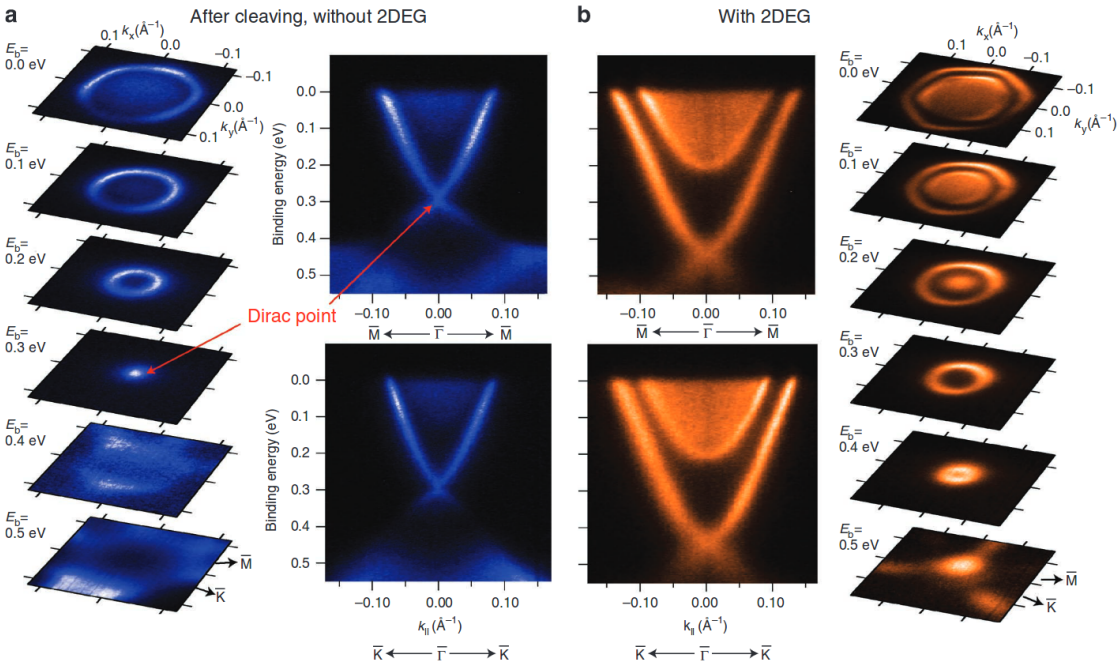

Figure 1.4: Development of a surface 2DEG in Bi_2Se_3 [41].(a) Electronic structure of Bi_2Se_3 approximately 30 minutes after cleaving the sample. The Dirac-like dispersion of the topological surface state is clearly shown. (b) After three hours in vacuum, the chemical potential shifted, probably due to defect formation. The sharp rim around the conduction band is the spectral signature of the 2DEG near the surface in real space.

The first discovery of superconductivity in this class of topological insulators came with Cu-intercalation between the van der Waals-connected Se layers. Here, the interstitial Cu atoms provide doping to the Bi-Se layer and push the layers apart, thereby increasing the c spacing. In this $Cu_xBi_2Se_3$, superconductivity was reported with a T_c of 3.8 K shown in Fig. 1.5. It is known that the intercalation of Sr or Nb can lead to superconductivity in Bi_2Se_3 with similar T_c values [42, 43].

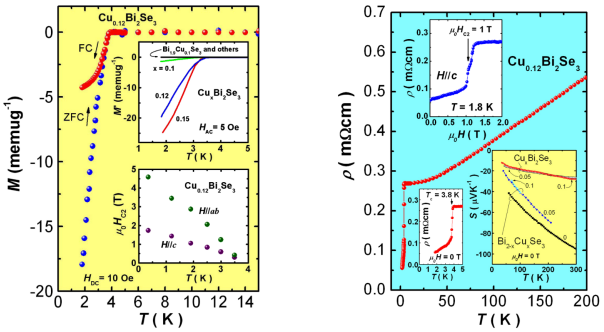

Figure 1.5: Temperature and magnetization evidence for superconductivity in $Cu_{0.12}Bi_2Se_3$ [38]. $T_c \sim 3.8$ K is observed from both measurements.

The superconductivity in $Cu_xBi_2Se_3$ originates from the bulk as evidenced by specific heat data [44], and the topologically nontrivial nature was not clear at first. A number of superconducting gap structures were suggested based on the nontrivial band structure in $Cu_xBi_2Se_3$, and some of these included an energy gap minimum, as shown in Fig. 1.6 [44].

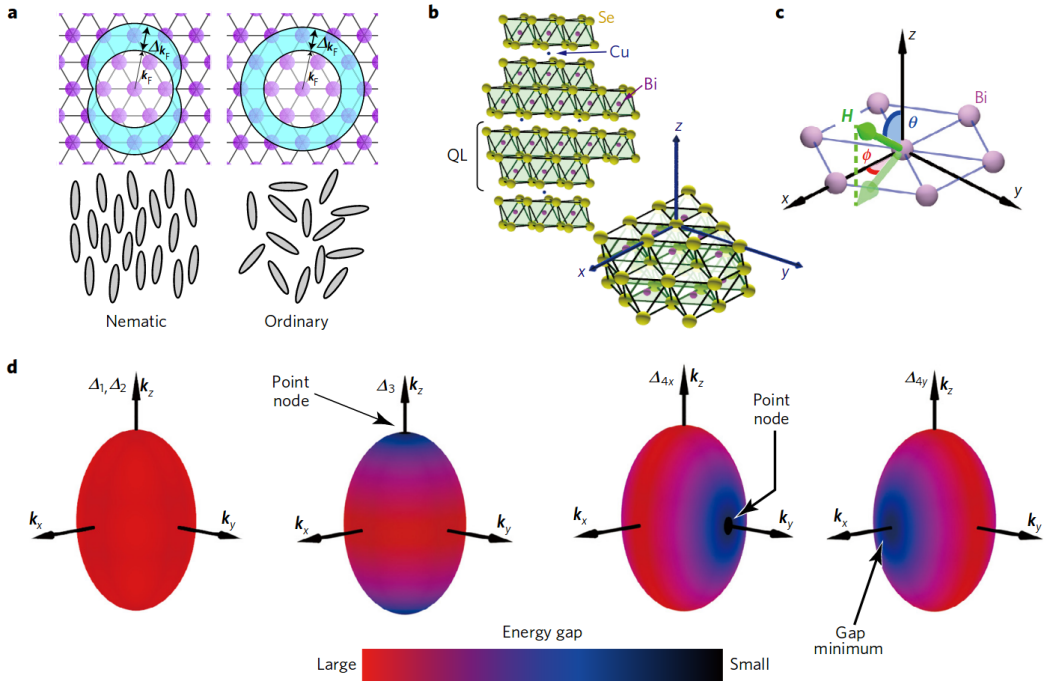

Figure 1.6: Candidate material for nematic superconductivity: $Cu_xBi_2Se_3$ [44]. (a) Comparison of nematic and ordinary superconductivity in a hexagonal crystal system, with a nematic liquid-crystal phase and an ordinary liquid phase. The thickness of the blue region in the top panels illustrates the superconducting gap amplitude in the reciprocal space. The grey ovals in the bottom panels represent molecules in a liquid-crystal system. (b) Crystal structure of $Cu_xBi_2Se_3$ with $x \sim 0.3$. The structure of the quintuple layer (QL) is shown in the right bottom figure. (c) Definitions of the axes and field angles with respect to the crystal structure. The purple spheres represent Bi atoms. (d) Schematic description of SC gap structures Δ_1, Δ_2, Δ_3, Δ_{4x}, and Δ_{4y} proposed for $Cu_xBi_2Se_3$. The ovals are Fermi surfaces, whose surface colour represents the gap magnitude, with black indicating $\Delta_k = 0$.

The gap structures in the $Cu_xBi_2Se_3$ single crystals were assessed by performing measurements in varying magnetic field direction perpendicular to the c axis. The results of magnetic field direction dependence of NMR [45] and specific heat [44] provide strong evidence for the so-called Δ_4 gap structure, a consequence of the nontrivial topology of superconducting state. However, the NMR results imply a Δ_{4x} gap structure [45], while the specific heat results suggest a Δ_{4y} gap structure [44]. Investigation with more samples will be needed before the actual SC gap structure is concluded in $Cu_xBi_2Se_3$.

These results provide strong evidence for the topological nature of superconductivity in $Cu_xBi_2Se_3$, providing evidence that intercalation of Cu does not destroy the topological nature of the parent compound Bi_2Se_3. Experimental work on antiperovskite oxides is scarce, but these ox-

ides have been explored theoretically. Recent predictions of interesting physics in antiperovskite oxides have triggered the interest of experimental physicists; an overview of these theoretical predictions is presented in the next section.

1.2.2 Theoretical Predictions in the Antiperovskite Oxides

The theoretical work on antiperovskite oxides began with data-mining work predicting strong topological insulating stats in a number of inorganic compounds, including some antiperovskite oxides [46]. At about the same time, band structure calculations on Ca-containing antiperovskite oxides predicting some of their structural, elastic, and thermal properties [47]. Closely after, theoretical work on Sn-containing antiperovskite oxides predicting some structural and electronic properties appeared [48], and here the typical perovskite oxides and antiperovskite oxides containing the same elements are compared. The small direct band gap in these Sn-based antiperovskite oxides is emphasized, as shown in Fig. 1.7 for Ca_3SnO, and the gap is shown to decrease with heavier elements in A_3SnO (A = Ca, Sr, Ba) [48].

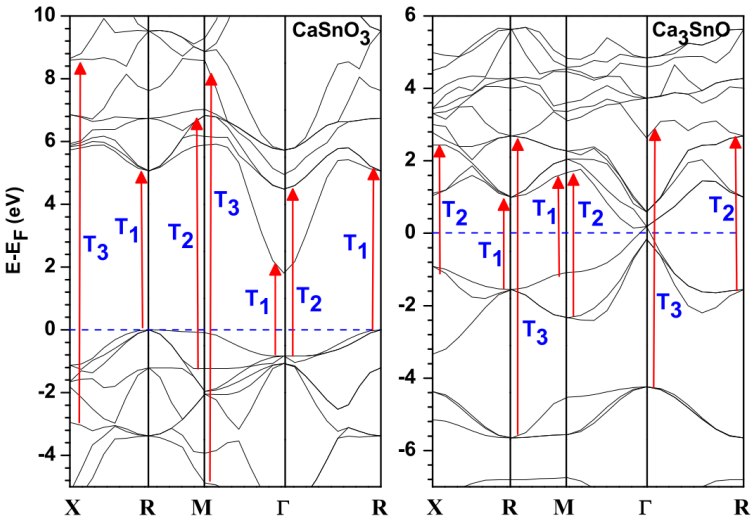

Figure 1.7: Calculated band structure of Ca_3SnO and $CaSnO_3$ compounds [48].

However, this class materials gained significant attention after prediction of three-dimensional Dirac electrons near the Fermi energy of Ca_3PbO, show in Fig. 1.8(b) [17]. This Dirac dispersion in the bulk band structure of Ca_3PbO is slightly gapped near the Fermi level, making this compound an insulator. The Dirac electrons predicted in this compound is expected to result in high mobility of electrons, similar to the high mobility of Dirac electrons in Graphene[49].

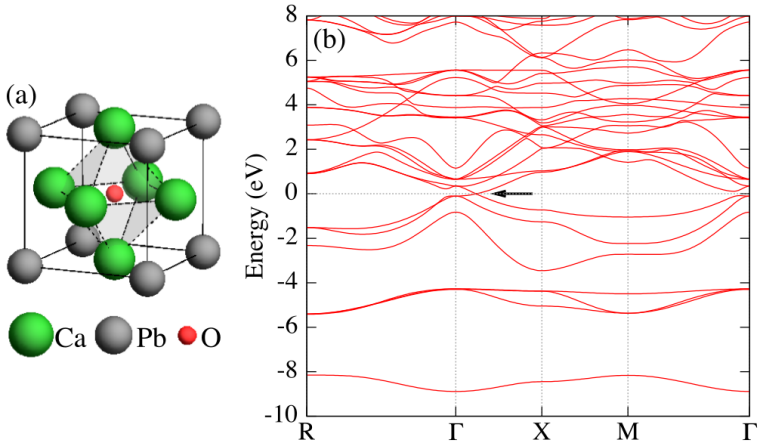

Figure 1.8: (a) Cubic inverse-perovskite structure of Ca_3PbO. (b) The calculated band structure of Ca_3PbO along the high symmetry lines in the Brillouin zone. The location of one of the Dirac points is marked with an arrow [17].

The appearance of the Dirac dispersion in the bulk electrons of Ca_3PbO is a consequence of energy inversion of Pb $6p$ valence band and Ca $3d$ conduction band. A charge balanced formula of $Ca_3^{2+}Pb^{4-}O^{2-}$ is expected, which is in accordance with the filled $6p$ orbital of Pb from band calculations. Band inversion and bands crossing the Fermi level is visible along the Γ-X line, and are evident in the Ca $d_{x^2-y^2}$ and Pb p illustrated in Fig. 1.9(c) and (e), respectively. Again, although this crossing along Γ-X line resembles a massless Dirac behavior, first-principles calculations and tight-binding calculations that include all Ca orbital contributions result in a gap near the Fermi level and massive Dirac electrons.

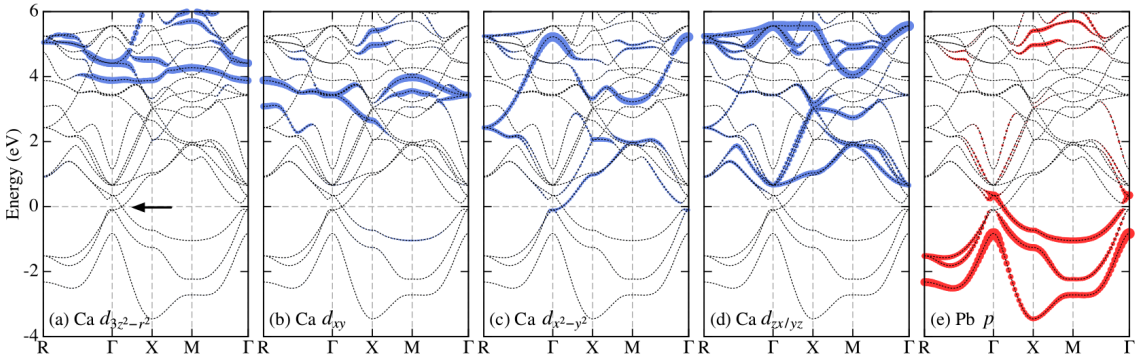

Figure 1.9: Orbital weight distributions on the bands obtained in the first-principles calculation of Ca_3PbO. (a)(e) show the distributions of the Ca $d_{3z^2-r^2}$, Ca d_{xy}, Ca $d_{x^2-y^2}$, Ca $d_{zx/yz}$, and Pb p orbital weights, respectively. The orbital weights are represented as the widths of the corresponding bands [18].

A gap appears near the Fermi level in the bulk bands of Ca_3PbO and other antiperovskite oxides, making the pristine compounds insulators. In some antiperovskite oxides, topological crystalline insulating states were predicted with gapless metallic surface states. These surface states are expected to be robust against disorder much like the surface states in topological insulators. Some antiperovskite oxides, such as Ca_3SnO, are trivial insulators (Fig. 1.10(c)), while others with heavier elements, such as Sr_3PbO, are topological insulators (Fig. 1.10(a)). Sr_3SnO is close to the border of topological to trivial insulator transition; however, is on the topological side and is expected to host a topological crystalline insulating state.

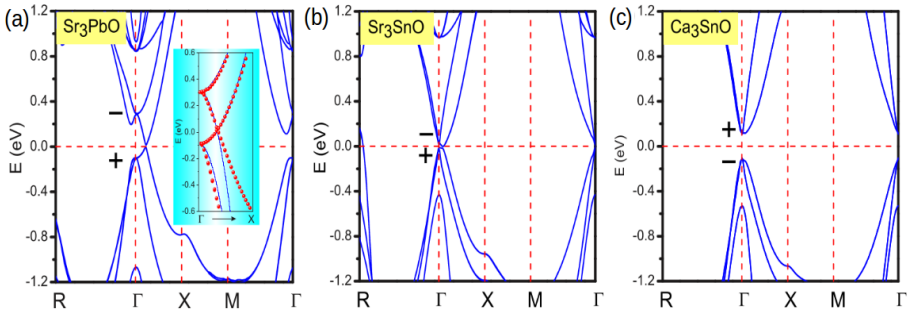

Figure 1.10: (a) Crystal structure of the antiperovskite A_3BX. (b) Band structure of TCI Sr_3PbO in which the orbital character of valence and conduction bands within a Dirac octet is inverted (± denotes the parities of the band orbitals). There is a small avoided crossing along the Γ-X direction. (c) Sr_3SnO is near a topological phase transition with gap closing at Γ.(d) Ca_3SnO is a trivial insulator [19].

The appearance of Dirac crossing in the bulk band structure of antiperovskite oxides is closely related to the emergence of topological crystalline insulating states. Such a Dirac crossing in antiperovskite oxides is the result of two factors: the band overlap based on the energy of bands and spin-orbit-coupling (SOC). Substituting A = Ca, Sr, and Ba in A_3SnO leads to an increase in band overlap with heavier atoms. No Dirac crossing appears for the light Ca_3SnO while one Dirac crossing appears for Sr_3SnO at the Fermi level, and two crossings appear for Ba_3SnO. The effect of SOC is demonstrated by comparing the band structure of Ca_3SnO, with no Dirac crossing, to that of Ca_3PbO, where the stronger SOC due to Pb results in a Dirac crossing. The evolution of band topology between different antiperovskite oxides A_3BO, with A = Ca, Sr, Ba and B = Sn, Pb, as function of band overlap and SOC is demonstrated in Fig. 1.11.

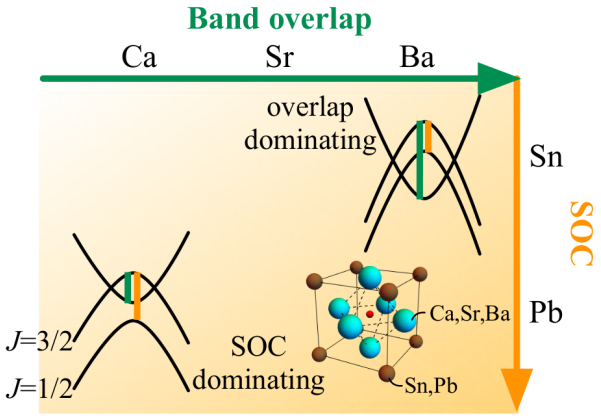

Figure 1.11: Schematic description of the evolution of the band topology as a function of the magnitude of the band overlap and spin-orbit coupling. The crystal structure is shown as the inset [20].

These theoretical results demonstrate that antiperovskite oxides are Dirac and topological systems that are tunable by substitution. The topological nature of some antiperovskite oxides make properties of these materials worthy of investigation in the normal state. Also, superconductivity in antiperovskite oxides has the potential to be topologically nontrivial and sets this class of materials as a hub for investigating topological systems that can lead to the eventual realization of a topological superconductor.

1.3 Motivation and Purpose

Motivated by the prospect of finding a new superconductor in a class of materials with new and interesting physics, we considered a number of materials that included Dirac and Weyl semimetals, honeycomb compounds, topological insulators, and Mott-Insulators.

The antiperovskite oxides had theoretical predictions of DSM and TCI states in them, so we were motivated to investigate their properties in general. We also had strong motivation to find superconductivity in this class of materials. Initially, we synthesized various A_3BO compounds including A = Ca, Sr, Yb & B = Sn, Pb. While samples with a mainly A_3BO phase were being synthesized, and their magnetic properties down to 0.10 K were being investigated, we found superconductivity in Sr_3SnO.

Upon discovery of the superconductivity in Sr_3SnO, the focus of the project shifted to characterizing this superconductivity and identifying the composition resulting in its superconductivity. This included identifying the H_{c2}-T phase diagram and magnetization curve, H-M. $Sr_{3-x}SnO$ samples were successfully synthesized and were suspected to contain some deficiency in Sr, but

we could not predict x precisely with the initial synthesis method. The synthesis method was later improved, $Sr_{3-x}SnO$ samples with controlled deficiency x were synthesized, and we achieved the goal of identifying the dependence of superconductivity on deficiency x.

Samples exhibiting superconductivity included Sr deficiencies, resulting in hole doping and lowering of the Fermi level from the Dirac point; theoretical calculations were performed to identify the nature of the Fermi surface and identifying the possible Cooper pairing in hole doped samples. Furthermore, band structure calculations on "$Sr_{2.5}SnO$" superlattices were performed to identify the effect of deficiencies in different distributions on the band structure. High-energy X-ray diffraction experiments at various temperatures were performed; we looked for superlattice peaks in low T measurements, and performed high T measurements to observe the decomposition of Sr_3SnO.

The oxidation state of Sn in our material was not confirmed yet, so we performed Sn Mössbauer spectroscopy on our samples, and found evidence supporting the Sn^{4-} state predicted theoretically. Also, some NMR measurements were performed on our superconducting and non-superconducting samples to guide us in the right direction. Furthermore, we observed paramagnetic Meissner effect in some samples, and tried to characterize this effect.

1.4 Thesis Overview

The overall plan of this thesis is as following. In Chap. 2, I will review topological materials and superconductivity, with focus on topological crystalline insulators and significance of realizing superconductivity in topological materials. Description of various experimental techniques is presented in Chap. 3. In Chap. 4, description of synthesis of various antiperovskite oxides and the optimization of Sr_3SnO is shown. Chap. 5 includes a description of the discovery of superconductivity in the antiperovskite oxide $Sr_{3-x}SnO$ and various measurements performed to characterize the nature of the superconducting state. In Chap. 6, the effect of deficiency x in $Sr_{3-x}SnO$ on properties and superconducting phase diagram based on deficiency is presented; the appearance of two superconducting transitions in all superconducting $Sr_{3-x}SnO$ is emphasized. Results of room temperature Mössbauer spectroscopy are also presented. In Chap. 7, the paramagnetic Meissner effect observed in some $Sr_{3-x}SnO$ samples, NMR results, and low temperature Mössbauer spectroscopy are summarized. In Chap. 8, I present a summary and conclusion of the work on antiperovskite oxides.

Chapter 2

Literature and Theory Review

Before presenting our experimental results, a review of theories on topological materials and superconductivity, where topological superconductivity will also be discussed. Finally, an overview of the current state of antiperovskite oxides in literature.

2.1 Topological Phases

Topologicaly phases, or more accurately topologically nontrivial phases, can only be understood on a global picture of a solid. This makes topological phases rather featureless, and difficult to identify using a local probe, and the difference between topological phases and trivial phases does not arise from a local order parameter. Subtle differences between topological phases and trivial phases do exit and a topological phase can be observed using a global measures, or a topological phase can be detected by placing it in contact with a trivial phase. Topological phases are difficult to detect in experiment, but one of the first topological phases was the observation of quantum Hall effect by Klaus von Klitzing and collaborators in 1980.[26] In this experiment, the behavior of a two dimensional electron gas at low temperature and high magnetic field, perpendicular to the plane of the electron gas, and it was found that the Hall conductivity is quantized for intervals of magnetic field (Fig. 2.1).

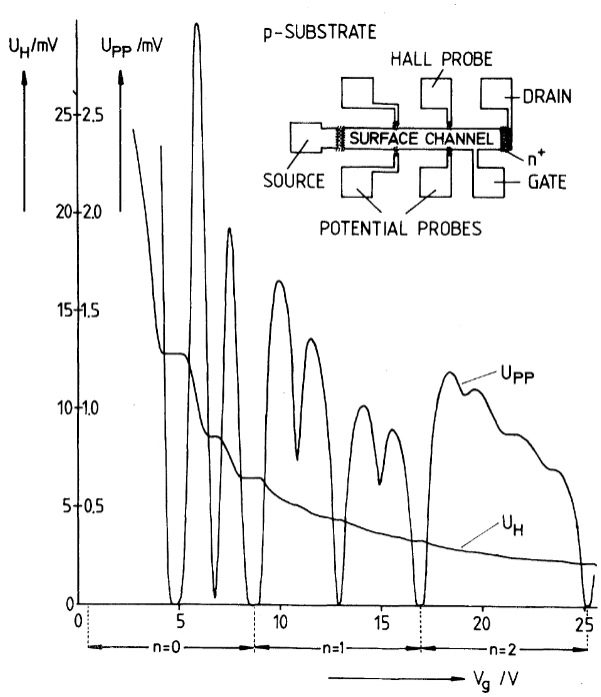

Figure 2.1: Discovery of quantized Hall voltage, $U - H$ in figure, as a function of gate voltage. Measurement under a magnetic field of 18 T and current of 1 μA [26].

To understand the quantization of Hall conductivity, it was required to expand the understanding of matter to include idea from the field of topology and to characterize matter based on a global property. The Chern number was introduced as a topological invariant derived from the band structure of electrons [30]. The Chern number dictates the quantized Hall conductivity, and has implications when the system has a boundary, the number of unidirectional gapless modes propagating around the boundary is dictated by the Chern number. Considering the topology near the high symmetry points in the Brillouin zone is important to clarify the topological nature in many materials. One can write a low energy effective theory near high symmetry points, so lets take a two dimensional material as an example, the effective two-band theory can written as:

$$H(k_x, k_y) = m\sigma_z + \nu(k_x\sigma_x - k_y\sigma_x), \tag{2.1}$$

where σ is a set of Pauli matrices, and m, ν are parameters; $\sigma_z = \pm 1$ indicates the valence and conduction bands. The Chern number of the system changes by one when m changes signs, and this will be further explained in 2.1.1. Furthermore, at the boundary between $m > 0$ and $m < 0$ systems, a gapless mode localized at the boundary will appear. This means that a gapless mode will appear at a boundary between a Chern number 1 and a Chern number 0 system (can be

vacuum). The nonzero Chern number and presence of gapless mode originates from the change in sign of m, which is due to the so-called "band inversion", further explained in 2.1.1.

After the discovery of the quantum Hall state, theories of topological phases in real materials were advancing towards a model where a topological phase can appear in the absence of magnetic fields and at room temperature. In this regard, a leap forward was acheived by Duncan Haldane in 1988 [31] after introducing a two dimensional electron model where the Chern number arises from the phases that the electrons accucumulate as the move through the lattice, rather than from an external magnetic field. This model described a class of insulators, now termed "Chern insulators", whose ground state is described by a nonzero Chern number. This Haldane model only considered orbital motion of electrons to be crucial in realizing topological phases; Charles Kane and Gene Mele expanded the idea to include spin considerations in 2005 [50]. In their model, an imagined scenario where spin up electrons occupy a band with positive Chenr number and spin down electrons occupy a band with negative Chern number, such that in a one-dimensinoal boundary of the system will have spin-up electrons propagating in one direction and spin down electrons moving the other way. These gapless edge states are robust features of this "quantum spin Hall" phase, and are protected against scattering as long as time-reversal symmetry is preserved.

2.1.1 Topological Insulators and Z_2 Classification

Topological insulators (TI), bulk insulators that have gapless edge states protected by time reversal symmetry, are now realized in two and three dimensions in real materials. These topological insulating states are allowed in materials with "band inverstion", where in the vacinity of a high symmetry point the Bloch wavefunctions of the valence and conductions bands becomes switched. This is akin to a Mobius strip in k space, where the electron can move from the valence band to the conduction band and back to the conduction band due to the presence of gapless states that cross the Fermi level. If we consider the case of SnTe, where band inverstion exists at the L point, in contrast to the trivial insulator PbTe.[29] In the effective low energy theory (Equation 2.1), the band inversion leads to a change in the sign of m, making boundary between SnTe and PbTe topologically nontrivial or boundary of SnTe with with vacuum (a trivial insulator). Spin-orbit coupling typically contributes to such band inversion by lifting degeneracies in bands in a nontrivial way. This is illustrated in the origin model for the quantum spin Hall phase with a conserved s_z component of spin, where spin orbit coupling results in spin up being in a specific Chern number band and spin down in the opposite Chern number band. These topological insulating materials have gained interest in the fields of thermoelectrics, spintronics, and quantum computing. The potential of topological insulators in spintronics application comes from the electron's spin being locked with the direction of motion in the gapless edge states, which is realized in the ideal quantum spin Hall state and extends to topological insualtors in two and three dimensions. This could lead to information processing with spin current rather than electric current. A material with surface states where spin-momentum locking allows propogation of spin-up and spin-down electrons in specific directions can have applicatin for spintronics. Also, a material with surface states

carrying current and an insulating bulk, where phonons have short mean free path, can lead to the "ideal thermoelectric" typically described as phonon-glass electron-crystal. In fact, the topological insulator Bi_2Se_3 is known to exhibit properites ideal for thermoelectric applications [51]. With various applications possible and robust properties, the search for new topological materials is warrented and this included the theoreteical efforts to realizing topological insulators beyond those protected by time-reversal symmetry. Now, topological insulating phases have been realized with a number of symmetries and in different dimensions [52].

Stepping back a little, we can look at the topological invariant called Chern number, which was demonstrated to dictate the experimentally observed Hall conductivity. This Chern number can be defined for a band structures with a gap and a single occupied band below a gap. All Bloch states $|u_k\rangle$ are labeled by a momentum k defined on a torus due to reduced translational symmetry of the lattice. One can then define a $U(1)$ connection in momentum space:

$$A_k = i \langle u_k | \nabla_k | u_k \rangle \tag{2.2}$$

This connection is termed "Berry connection" and essentially compares the $U(1)$ phase of Bloch states at two infinitesimally separated momenta. A different gauge can be used to define these $U(1)$ phases, so it is more meaningful to talk about the 'Berry curvature', which is gauge invariant, and defined as:

$$F_k = \nabla_k \times A_k \tag{2.3}$$

For a two dimensional case, integration of the Berry curvature over the entire Brillouin zone gives a quantized number - the Chern number:

$$n = \frac{1}{2\pi} \int d^2k F_k \tag{2.4}$$

Typically for topological materials, the nature, trivial or nontrivial, of the occupied bands can be determined by examining the low energy theory of valence and conduction bands near the high symmetry points. With such simplification, we can apply formulation on Dirac fermions from field theory to an effective theory of a lattice model. The effective Hamiltonian describing a single valley of graphene, described earlier, is common building block of topological states.

$$H(k_x, k_y) = m\sigma_z + v(k_x\sigma_x + k_y\sigma_x), \tag{2.5}$$

If we consider the case of $m > 0$, a vector field tilts in momentum space with changing k. The Chern number defined via Berry curvature above will be $1/2$. Similarly, for $m < 0$, the Chern number can be defined via the Berry curvature and will be $-1/2$. Although the value is $1/2$ in each of these cases, the integer nature of the Chern number maintained due to an even number of Dirac valleys in the Brillouin zone. However, it should be emphasized that the absolute values of these Chern numbers are not meaningful, since we ignored the Berry curvature away form $k = 0$

in our effective theory, but we can assume that the Berry curvature does not change scientifically away from $k = 0$ as m changes sign. The difference between the Chern numbers of the $m > 0$ and $m < 0$ cases is 1.

At the boundary of two phases with Chern numbers differing by 1, we have a gapless edge state. If we consider an interface of two systems with mass having opposite sign, a chiral mode localized to the point where the two phases meet and propagating perpendicular to the direction where the mass change occurs. This propagating state are the edge state of Chern insulators/quantum Hall systems, and this formalism can be extended to other topologically nontrivial phases.

The model for two-dimensional topological insulator by Kane and Mele[50] included a definition of a Z_2 invariant, which allows us to distinguish a topologically trivial phase from a topologically nontrivial one. If we consider the tight binding model on a honeycomb lattice, such as:

$$H = \sum_{<ij>\alpha} t c^{\dagger}_{i\alpha} c_{j\alpha} + \sum_{<<ij>>\alpha\beta} i t_2 v_{ij} s^z_{\alpha\beta} c^{\dagger}_{i\alpha} c_{j\beta} \tag{2.6}$$

Where α, β label the spin of electron and s^z is the Pauli spin matrix. The usual nearest neighbor hopping is represented by the first term, while the second term represents a spin-dependent second neighbor hopping. We have $v_{ij} = \pm 1$ for elecrong moving clockwise or counterclockwise after hopping twice, which leads to spin-up and spin-down electrons picking up opposite phases after hopping to second neighbors. The model without spin was considred by Haldane [31], which breaks time reversal symmetry and leads to band structure with Chern number 1. On the other hand, the Kane-Mele model described in the equation above restores time reversal symmetry by restricting spin-up and spin-down electrons to two different bands with opposite Chern numbers.

Time reversal symmetry is necessary to protect the gapless edge states by first considering that for spin-1/2 electrons the time reversal symmetry squares to -1. Kramers' theorem states that all eigenstates are doubly degenerate (at least), and the Bloch states must come in pairs at time reversal invariant momenta (TRIM) in the Brilloiun zone (such as $k = (0, 0), (\pi/a, 0)$ where a is lattice spacing). If edge states do exist between bulk band gap, these states must be twofold degenerate at each TRIM. With such a constraint, we have two ways of connecting edge states between TRIM points (Fig.xx). In one case, the edge states cross the Fermi energy an even number of times, and in the other case an odd number of times. This number of crossings is a Z_2 invariant, and can be used to determine if the system is a topological insulator, with odd number of crossings, or a trivial insulator, with an even number of crossings. In the case of even number of crossings, the Fermi level can be shifted to a position with no crossings, such that no gapless edge conduction can propagate.

One typically defines a Z_2 quantity at each of the special momenta in the Brillouin zone, and the product of these Z_2 invariants gives the bulk Z_2 invariant. This bulk Z_2 invariant gives allows us to distinguish a topological insulator from a trivial one. In topological insulators with inversion symmetry, the nature of the topology can be concluded by analyzing the parity of the occupied

bands [29]. We have demonstrated topological insulators in two dimensions, but topological insulators can also exist in three-dimensions, which can also be classified using a bulk Z_2 invariant. In three dimensions, it is possible to have a "weak" topological insulator, where the Z_2 invariant along specific directions reflects a nontrivial topology, while the Z_2 invariant representing the overall bulk indicates a topologically trivial state. This will be further discussed in the next section on topological crystalline insulators.

2.1.2 Topological Crystalline Insulators

Topological crystalline insulators (TCI), as the name suggests, are those protected by crystalline symmetry rather than time-reversal symmetry. This class of topological materials was first realized in SnTe material class[52], where mirror reflection symmetry protects gapless boundary states. TCIs, similar to Chern insulators and TIs, are characterized by bulk topological invariants, and these are RELATED to the gapless boundary modes. These modes are Dirac fermions like the TIs, but are distinct in that an even number of gapless Dirac cones appear on the surface of TCIs compared with an odd number in TIs. Also, in TIs these Dirac cones are pinned to high symmetry points, while in TCI's they are not necessarily. The gapless boundary states of TCIs can be manipulated easier than those of TIs, because crystal symmetry can be broken more easily than time-reversal symmetry. The first TCIs were predicted theoretically and confirmed experimentally in IV-VI semiconducors SnTe, $Pb_{1-x}Sn_xSe$, and $Pb_{1-x}Sn_xTe$ [52]. Following the work on these TCIs, many efforts were initiated to classifying the topological phases in different crystal symmetry classes, which lead to the realization of TCIs in the antiperovskite oxides.

2.2 Superconductivity

The success in liquefying helium in 1908 by Heike Kamerlingh Onnes made it possible to perform experiments approaching absolute zero. In April 1911, Onnes saw that the resistivity of mercury disappeared at 4.2 K, marking the first discovery of superconductivity. Measurements on lead and tin followed, and resistivity dropped to zero at 7.2 K and 3.8 K, respectively. It was concluded from these results that the resistivity of some materials drops to zero at a critical temperature (T_c), and this phenomenon was called superconductivity.

In 1933, Meissner and Ochsenfeld discovered the second important property of superconductors. If a superconductor placed in a weak magnetic field and cooled below T_c, then the magnetic flux is expelled from the interior of the material. After these two important properties were clarified in these initial few years, efforts to explain these properties of materials theoretically were underway. However, it was only in 1957 that the first theory explaining superconductivity was presented by Bardeen, Cooper, and Schrieffer.

The superconducting state is a thermodynamic state, and the transition from normal state to superconducting state is a phase transition, which is reflected in the jump seen in specific heat

accompanying this transition. As such, measuring the specific heat of a material can provide information about the superconducting state; typically the normalized specific heat results is used to characterize the superconducting material.

2.2.1 BCS Superconductivity

The microscopic theory presented by Bardeen, Cooper, and Schrieffer is commonly called BCS theory. Central to this theory is that conduction electrons form Cooper pairs due to k-independent phonon mediated attractive interaction. The Cooper pairs condense into a ground state with an isotropic s-wave superconducting gap structure, and superconductors that follow this formalism are called "conventional".

When a BCS superconductor is cooled below T_c, electrons with opposite momentum and spin are weakly coupled. This coupling can be understood in the following, as an electron moves through the lattice it attracts positively charged lattice ions, which causes them to move towards the electron. The electron travels much faster than the positive ions, so it is no longer near the positive ion moving towards its previous position, but this movement of positive ions creates a positive net charge in the lattice that attracts a second electron. This coupling of positive ion movement and electrons is called electron-phonon coupling. The Cooper pairs move in a single coherent motion, and the distance between the two electrons is called the coherence length ξ, which is much larger than distance between one of those electrons and the nearby electrons. In BCS, the Cooper pair takes a ground state wave function as follows:

$$|\Psi_{BCS}\rangle = \prod_k (u_k + v_k c^\dagger_{k\uparrow} c^\dagger_{-k\downarrow}) |0\rangle \tag{2.7}$$

where $c^\dagger_{k\uparrow}$ and $c^\dagger_{-k\downarrow}$ are creation operators for a pair of electrons with zero relative momentum and opposite spin. $|0\rangle$ is the vacuum state. u_k and v_k are complex coefficients with total probability 1. The Hamiltonian of such Cooper pair can then be reduced using second quantization, which would reveal an attractive interaction originating from motion of ions. This motion of ions screen the repulsion between electrons due to electrostatic Coulomb force. More details on this formulism is described by Tinkham [53].

The result lead to to realizing the energy of a superconductor based on wave vector k and the energy gap Δ, as follows:

$$E_k = \sqrt{\left(\frac{\hbar^2 k^2}{2m} - \mu\right)^2 + \Delta^2} \tag{2.8}$$

The energy gap depends on temperature according to BCS theory, and a superconductor with gap symmetry that follows the BCS prediction is known to have an s-wave pairing symmetry. As already mentioned, superconductors with s-wave pairing symmetry are called "conventional" BCS superconductors. A finite sized spherical energy gap for single particle excitations appears throughout the entire Fermi surface, known as the superconducting gap. A superconductor that

with symmetry that deviates from this s-wave like symmetry is considered "unconventional". The angular momentum in such a superconductor is $L = 0$.

BCS theory descibes superconductivity observed in the elements at ambient pressure and thousands of compounds, where electron-phonon coupling is significant for superconductivity. Also, the superconductivity observed at 203 K in H_3S under high pressure is explained by a conventional BCS theory. The highest T_c for a BCS superconductor under ambient condition is 39 K found in MgB_2[54]. Higher T_c is found in some unconventional superconductors, which will be discussed in the next section.

2.2.2 Unconventional Superconductivity

Unconventional superconductors typically have stronger Coulomb repulsive interaction between electrons, so the Cooper pairs with non-zero angular momentum is favored to minimize the total energy. Superconductors with p-wave pairing, such as the layered oxide Sr_2RuO_4, will form Cooper pairs with relative orbital angular momentum $L = 1$ from a spin-triplet state. Cuprate high-T_c superconductors have a d-wave pairing symmetry with relative angular momentum $L = 2$ from a singlet state. In such superconductors, the energy gap will diminish at certain locations on the Fermi surface, such that a nodal structures for the energy gap forms. Cooper pairs with orbital state that have p and d-waves are analogous to the atomic p and d orbitals, respectively. Pauli exclusion principle allows spin-singlet pairs for s and d orbital states, and spin-triplet pairs for p orbital state. In this sense, Sr_2RuO_4 and high-T_c cuprates are "unconventional" with respect to their gap symmetry. In cuprates, the undoped material is insulating, and after doping we have metallic behavior and superconductivity in these layered compounds. The copper oxide layer in the cuprates is believed to be responsible for the conduction in these materials.

Heavy-fermion compounds, containing magnetic $4f$ or $5f$ ions, were shown to exhibit unconventional superconductivity. In these compounds, the ions exhibit Kondo effect, and the conduction electrons form a bound resonance with the localized f electrons of the magnetic ions. The "Kondo" lattice of magnetic ions formed in these compounds results in electronic specific heat coefficient 1000 times that of conventional metals, and this is reflected in the specific heat jump at the superconducting transition in these compounds. d-wave pairing is suspected in some heavey fermion superconductors due to non-degenerate order parameter, characteristic of a singlet pairing, but this is still to be investigated with phase-sensitive measurements. Organic superconductors show some similarities to the cuprates, with some evidence of d-wave state in this class of materials.

Iron-based superconductors have a metallic parent compound, in contrast to the cuprates, but the layered structure in this class of superconductors allows us to draw parallels with the cuprates. Thermal conductivity and other measurements for certain doping suggest a d-wave like gap in these iron based superconductors, but with weaker correlation between electrons than that observed in the cuprates. However, angle-resolved photoemission measurements show isotropic gaps around the Fermi surface, which is proposed to be the result of order parameter with $s\pm$

state. Strong nematic effects have been observed in the normal state in both cuprates and iron-based superconductors.

2.2.3 Topological Superconductivity

Topological superconductivity, in a broad definition, is one with non-trivial wavefunction describing the superconducting state. This can be achieved with proximity effect, first proposed in a heterostructure of a TI with an s-wave superconductor, or in some unconventinoal superconducting states, such as the chiral $p_x \pm ip_y$ state in Sr_2RuO_4. Drawing a parallel with topological insulators, one can define a number of topological numbers for superconductors based on dimensions and symmetries of the system. If one of these topological numbers is nonzero, then the superconductor can be called topological. Many unconventional superconductors have nodal superconducting gaps, and the nodes are associated with a nonzero topological numbers, making these superconductors topological [55].

In a topological superconductor, the bulk is fully gapped in the superconducting state, but gapless surface (or edge) states are topologically protected. The particle-hole symmetry in the low-energy Hamiltonian of topological superconductors leads to the surface states where the particles are identical to their own antiparticle, called Majorana fermions. Where the surface states are pinned to zero energy, they are called Majorana zero modes, and these do not obey Fermionic or Bosonic statistics. These Majorana zero modes obey non-Abelian statistics, and have potential for application towards quantum computing [56].

Initially, the concept of topology was considered for fully gapped systems only, but it has recently been expanded to include gapless systems (i.e. gaps with nodes) [57]. This has led to an increase in the number of superconducting materials with potential to host topological superconductivity, and now includes nodal systems such as the cuprate, heavy fermion, and organic superconductors to name a few [56].

Experimental work on $Cu_xBi_2Se_3$ demonstrating the nodal gap structure of the superconducting state provides some evidence of topological superconductivity [56], as highlighted in the previous chapter. In other topological materials, the superconducting gap is not necessarily nodal, and other way of providing evidence for the topological nature of the superconductivity are needed.

2.2.4 Superconductivity in Materials

Tens of thousands of compounds and alloys have been shown to exhibit superconductivity, and a number of these compounds have been discussed in the previous sections of this thesis. To have a more comprehensive view of the progress in the field of superconductivity towards useful applications, we can look at the increase in T_c of materials plotted as a function of year of discovery. Besides the improved T_c demonstrated in this figure, work on these classes of superconductors

have uncovered important physics, such as Mott physics, and motivated the developments of new experimental techniques, such as the SEM.

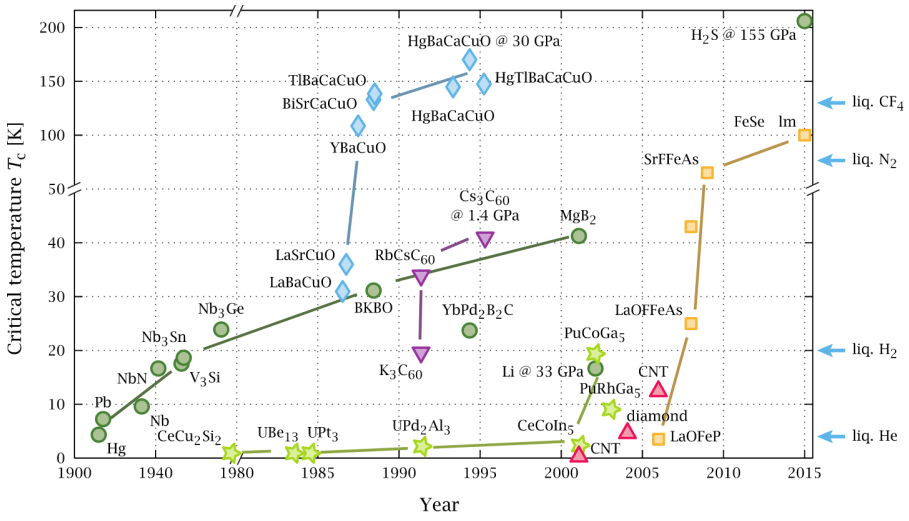

Figure 2.2: Timeline of critical temperature (T_c) of superconducting materials as a function of year of discovery [58].

Upon discovery of a new superconducting material, exploration of doping and substitution effects have led to significant increases in T_c and provided hints about the nature of the superconductivity. The discovery of superconductivity in the cuprates was followed by work on the effect of substitution and dopings, as well as studies on the effect of oxygen deficiency on the T_c in some cuprates. A similar set of studies were performed on the iron pnictide based superconductors, initially with a T_c of 5 K in LaOFeP[59], and later work on related iron pnictides resulted in increase of T_c to 26 K in $LaO_{1-x}FxFeAs$[7]. Seeing the importance of doping and substitution studies on these previously discovered superconductors, warrants investigation of such effects in any newly discovered superconductor.

2.2.4.1 Superconductivity in Sr-Sn Alloys

The focus of this thesis is on superconductivity in the antiperovskite oxide $Sr_{3-x}SnO$, so it is important to highlight superconductivity in the Sr-Sn-O system. The work on Sr-O and Sn-O binary compounds do not include any reports of superconductivity in these systems, and generally these binary oxides are insulating in nature. We don't find any reports of superconductivity in the Sr-Sn-O ternary compounds, and this leaves us with Sr-Sn alloys. In the Sr-Sn phase diagram we have three reports of superconductivity: β-Sn, $SrSn_4$, and $SrSn_3$, which have T_c's of 3.7, 4.8, and 5.4 K, respectively [60, 61, 62].

Superconductivity in Sn is reported with a T_c of 3.7 K [60], and was one of the first superconductors discovered by Onnes in 1911. Superconductivity in $SrSn_3$ was demonstrated from magnetization measurement [61], which shows a T_c of 5.4 K from zero-field-cooling (ZFC) and field-cooling (FC) measurements, shown below.

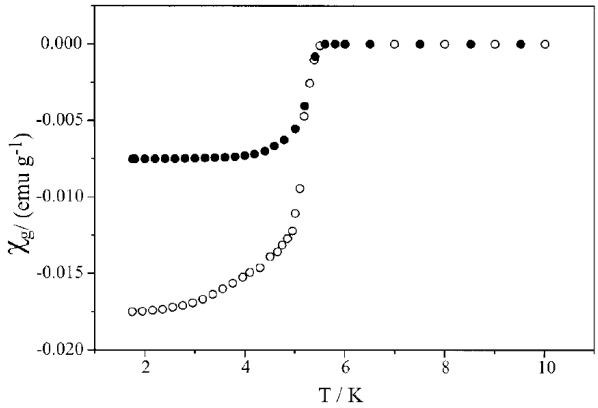

Figure 2.3: Magnetization results in zero-field-cooling (open circle) and field-cooling (closed circle) conditions of $SrSn_3$ as a function of temperature (H_{ext} = 10 G) [61].

Superconductivity in bulk $SrSn_4$ was reported from magnetization data with a T_c of 4.8 K from ZFC and FC curves [62]. The superconducting properties were later reported in single-crystals of $SrSn_4$ with a comparable value of T_c. Resistivity of $SrSn_4$, shown below, is metalic in nature and drops to zero sharply at about 4.9 K [63].

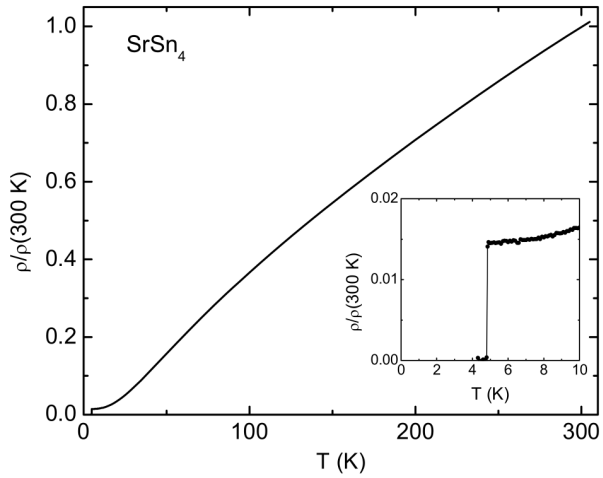

Figure 2.4: The temperature-dependent, normalized resistivity of $SrSn_4$ [63]. Inset: low temperature data showing the superconducting transition.

The resistivity of $SrSn_4$ for different magnetic fields applied along the $H||b$ axis and $H||ac$ plane shows clear anisotropy, reflecting the anisotropy of the crystal structure. The T_c estimated from onset and offset of resistivity and from magnetization measurement for fields applied $H||b$ and $H||ac$ are shown in the figure below. The upper critical field of $SrSn_4$ is estimated to be well below 10 kOe at $T = 0$, and this superconductivity is different from that of Sn (T_c = 3.7 K and H_c = 305 Oe) used as flux in growing these single-crystals.

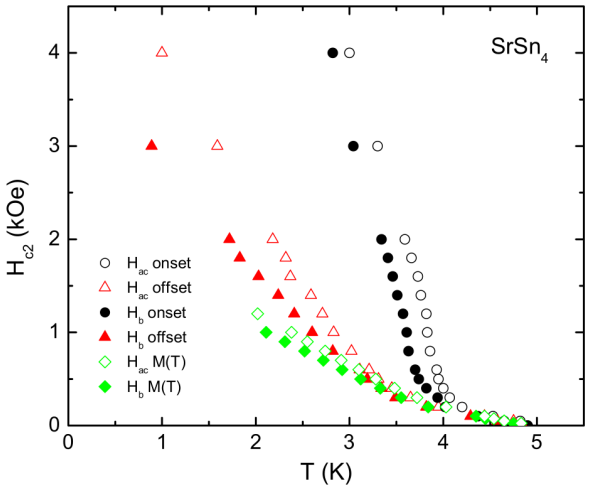

Figure 2.5: Anisotropic upper critical field of $SrSn_4$ from magnetization and magnetotransport measurements [63].

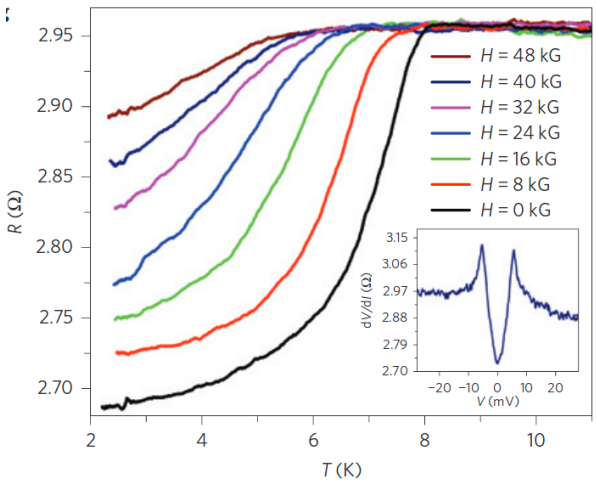

Figure 2.6: Magnetic field dependence of the $R(T)$ curves for a point contact formed on a Cd_3As_2 sample [23] (the in-field data have been given vertical shifts to match the normal state resistance). The inset shows the corresponding dV/dI vs. V spectrum at zero field.

2.2.4.2 Superconductivity in Topological Materials

In this section, we can look at superconductivity found in materials with topologically nontrivial band structure. Some topological superconductivity emerges in materials that are topologically trivial in the normal state; some of these materials are highlighted in Table 2.1, but the specific examples discussed in this section are for materials with nontrivial topology in the normal state.

Cd_3As_2 is a 3D topological Dirac semimetal as demonstrated by ARPES and scanning tunneling spectroscopy, which has been shown to exhibit superconductivity in point contact experiments [23, 39]. The use of Ag metal tip on the surface of Cd_3As_2, both Ag and Cd_3As_2 are not superconductors, results in superconductivity as evidenced by sudden drop in resistivity, shown in Fig. 2.6. The T_c of this transition decreases with increasing magnetic field, evidencing superconductivity in this point contact experiment.

WTe_2 is proposed to be a Weyl semimetal, explaining its extremely large magnetoresistance [64]. Superconductivity has been reported under pressure in WTe_2 with highest T_c of 7 K at about P = 16.8 GPa [40]. With further increase in P, the T_c decreases monotonically. The resistivity as a function of temperature $R(T)$ at different applied fields for WTe_2 at P = 24.6 GPa are shown in Fig. 2.7(a). The estimated T_c-H phase diagram is shown in Fig. 2.7(b), with a black curve is a line of best-fit used to estimate the upper critical field, $H_{c2}(0)$ = 2.72 T.

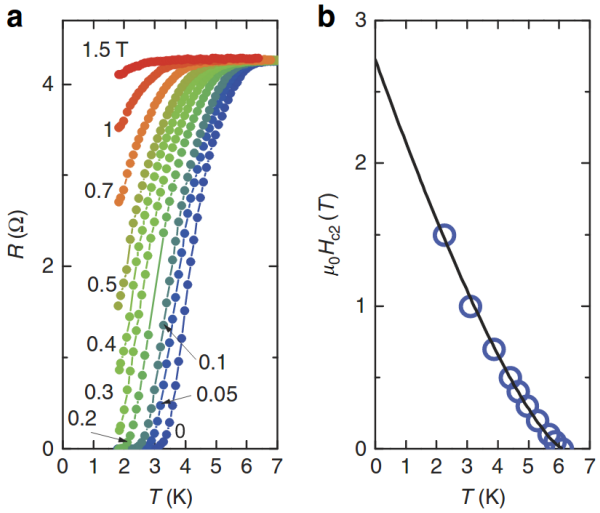

Figure 2.7: Resistance of WTe_2 under different pressures [40] (a)Temperature dependence of the resistance of WTe_2 under different fields up to 1.5 T at 24.6 GPa. (b)The T_c-H phase diagram at 24.6 GPa. The black curve is the best-fit line.

Table 2.1: Summary of candidate material for topological superconductivity.

Bulk/Proximity	Topology of Normal State	Gap nodes	Material	Possible Pairing State	Surface States	Remarks
Bulk	Topologically Trivial	Full gap	Sr_2RuO_4	Chiral-p	Observed	
			^{3}He; B phase	3D p	Observed	
			SrPtAs	Chiral-d		
		Nodal gap	^{3}He; A phase	3D chiral-p		Weyl superfluid
			UPt_3; B phase	3D chiral-f		Heavy fermion trigonal,Weyl superconductor
			URu_2Si_2	3D chiral-d		Heavy fermion tetragonal, Weyl superconductor
			UBe_{13}			
			YPtBi, RPdBi (R=Rare earth)	$j = 3/2$ pairing?		Non-centrosymmetric cubic, BTRS by theory
			High-Tc cuprates	Q2D $d_{x^2-y^2}$	Observed	
			$CePt_3Si$, CeTSi$_3$ (T = Rh, Ir)	Q2D $p + s$		
			Li_2Pt_3B	3D $p + s$		
	Topologically Non-Trivial	Full gap	$Sn_{1-x}In_xTe$	3D	Observed	
			$A_xBi_2Se_3$ (A = Cu, Sr, Nb, Tl)	Q2D (3D?) p or f	Observed	
		Nodal Gap	$Cu_x(PbSe)_5(Bi_2Se_3)_6$	Q2D nodal		
		Unknown	Au_2Pb			
			Cd_3As_2			Point Contact
			WTe_2			Under Pressure
Proximity	Topologically Non-Trivial		Heterostructure of Topological Insulator/s-wave superconductor Inducing superconductivity in a topologically non-trivial material.			

2.3 Review of Antiperovskite Oxides

The first report on antiperovskite oxides was in 1980 by Widera and collaborators, where in an attempt to synthesize Sr_3Sn, they found the compound was only stable with some oxygen inclusion, leading them to identify Sr_3SnO and other antiperovskite oxides [15]. Our interest for working on antiperovskite oxides was sparked by the theoretical work on these materials, especially those by Kariyado and Hsieh [17, 19].

I will briefly review the history of the appearance of antiperovskite oxides in theoretical work, which started with data-mining work [46] and theoretical predictions on Ca-based antiperovskite oxides [47]. This was followed by work on Sn-containing antiperovskite, including Sr_3SnO, showing band structure and describing the ionic-covalent nature of bonds in these compounds [48]. The early reports on these compounds, include the pioneering work predicting Dirac semimetal states in Ca_3PbO and other antiperovskite oxides [17, 18]. Some details of this early work were already mentioned in Chap. 1. The slight gap mentioned by earlier work on the antiperovskite oxides allows us to classify these compounds insulators.

Prediction of topological crystalline insulating states in some antiperovskite oxides by Hseih and collaborators brought further attention to this class of materials. This prediction meant that some of these slightly gapped compounds contained gapless surface states. The existence of TCI states is a related to the band inversion near the Γ point, which is related to the mirror Chern number for the material. This Chern number is related to the sign of m, which controls the band inversion, and the velocities v_1 and v_2 that appear in the four-band Hamiltonian $H_{\pm i}(k_y, k_z)$ defined within a mirror subspace of the cubic point group [19]. Using the linear combination of these velocities $v_d = v_1/2 - v_2$ and $v_s = v_1 + v_2/2$, the topological phase diagram of these materials can be plotted as a function of m and $R = |v_d/v_s|$, as shown in Fig. 2.8. The region with $m > 0$ contain trivial phase such as in Ca_3SnO, while the region of $m < 0$ contains TCI phase such as in Ca_3PbO and Sr_3SnO [19].

The nontrivial band topology emerges in antiperovskite oxides as a fucntion of spin-orbit-coupling (SOC) and band overlap. The relative size of SOC and band inverstion in controlled in antiperovskite A_3BO by substitution of A (Ca, Sr, Ba) and/or B (Sn, Pb) atoms, as shown in Fig.1.11 [20]. When band overlap dominates over SOC, the resulting nontrivial band contains two Dirac cones, as demonstrated for Ba_3SnO, as shown in Fig. 2.9 [20]. In the case where SOC dominates over band overlap only one Dirac cones appears in the band structure, as in the case for Ca_3PbO shown in Fig. 2.9.

Recent first-principles electronic calculations of pristinte and intrinsic vacancy containing Sr_3SnO make predictions for the vacancy dependence of magnetic properties. The Sr and O vacancy containing Sr_3SnO is non-magnetic, while Sn vacancy containing Sr_3SnO results in stable ferromagnetism, as shown in Fig. 2.10 by spin polarized partial density of states (DOS) [65]. These results provide a possible explaination for ferromagnetism observed in thin-films of Sr_3SnO, which was explained in the initial report due to O vacancies [66, 67].

Another first-principles calculations study of mechanical, thermal transport, and supercon-

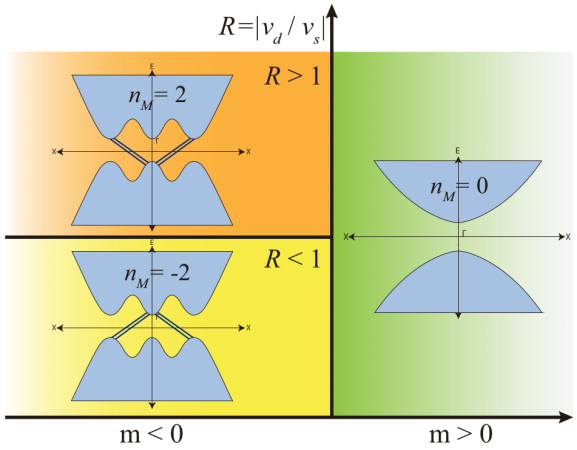

Figure 2.8: Topological phase diagram for the minimal quadratic kp theory describing a Dirac octet, for the (100) mirror plane. The three phases have different mirror Chern numbers (n_M). Each inset is a schematic band structure depicting bulk states in light blue and surface states in dark blue, cutting through the bulk gap. The existence of the surface states is dictated by n_M.[19]

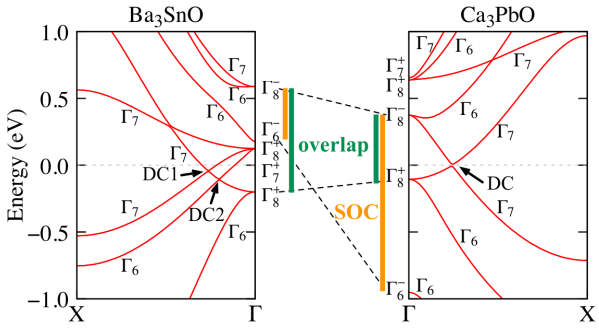

Figure 2.9: Band structures on the $\Gamma - X$ line along with the irreducible representations of the bands. The left (right) panel shows the band structure of Ba_3SnO (Ca_3PbO). The Dirac points are marked with arrows [20].

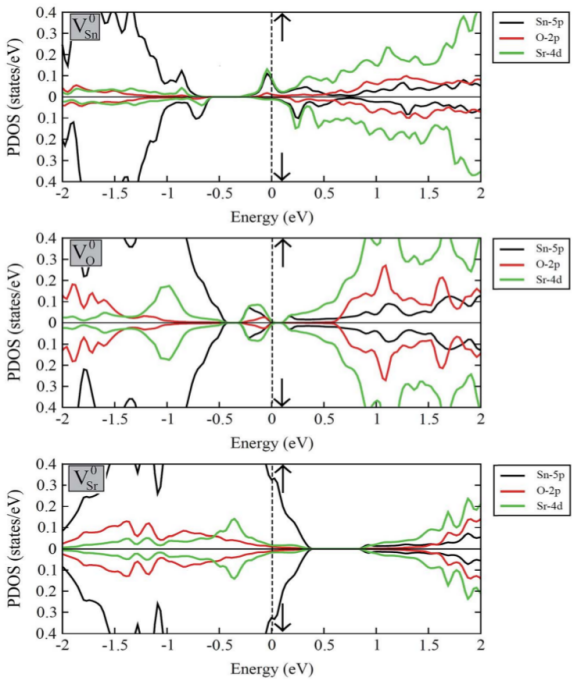

Figure 2.10: The spin-polarized partial DOS plots of V^0_{Sn} ,V^0_O and V^0_{Sr} containing $2 \times 2 \times 2$ superlattice of Sr_3SnOcalculated with the inclusion of SOC. The majority and minority spin channels are represented by up and down arrows, respectively. [65]

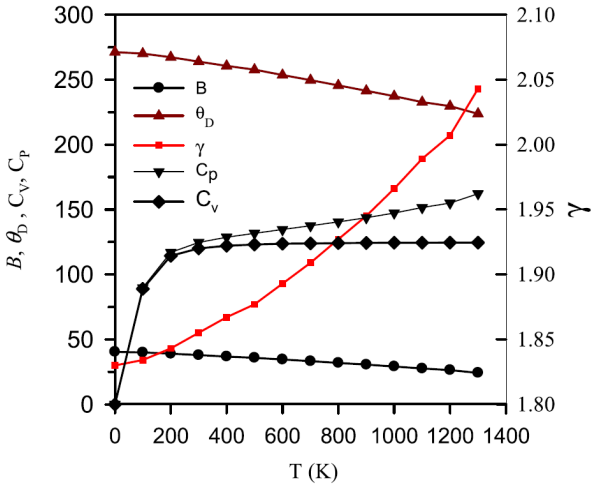

Figure 2.11: Variations of different thermodynamic parameters, Debye temperature θ_D in K, Grneisen parameter g, specific heat at constant volume C_V in J/mol.K, specific heat at constant pressure C_P in J/mol.K, as well as bulk modulus (B) in GPa, with temperature T (K).[68]

ducting properties of Sr_3SnO predicts properties shown in Fig. 2.11 [68]. Furthermore, a T_c of 8.38 K is predicted for the superconductivity in Sr_3SnO, which is similar to that T_c measured experimentally in our work.

Taking a step back, we can look at the experimental work on antiperovskite oxides, which started with the discovery of Sr_3SnO [15] and placing it within the Sr-Sn phase diagram [69]. Sr_3Sn is not stable, which is missing in the phase diagram shown in Fig. 2.12. However, the inclusion of O in Sr_3Sn stabilizes the cubic structure, and this tendency can be generalized to other antiperovskite oxides. The Sr-Sn alloy $SrSn_4$ is not shown in this original phase diagram, and was later added in an updated phase diagram [70].

The initial report on antiperovskite oxides A_3BO inlcuded the combination of A = Ca, Sr, Ba and B = Sn, Pb [15]. This list of antiperovskite oxides was later expanded to include A = Ca, Sr and B = Si, Ge, as well as Yb_3BO where B = Si, Ge, Sn, Pb [71]. The list was expanded once more to include Eu-containing Eu_3BO where B = Sn, In. The magnetic properties of Eu containing antiperovskite oxides is shown in Fig. 2.13, where an antiferromagnetic transition is observed in Eu_3SnO at $\sim$ 30 K [72]. Considering the absolute values of resistivity, Eu_3InO is described as a metal, while Eu_3SnO is most likely a heavily doped degenerate semiconductor or semimetal [72].

The thermoelectric properties of bulk Ca_3SnO and Ca_3PbO were recently reported, and a positive Seebeck coefficient for both compounds is positive, suggesting the dominance of hole carriers [73]. The Hall resistivity ρ_H increases linearly for Ca_3SnO, as shown in Fig. 2.14, and a positive Hall coefficient is reported, consistent with hole-carriers dominating. A mobility

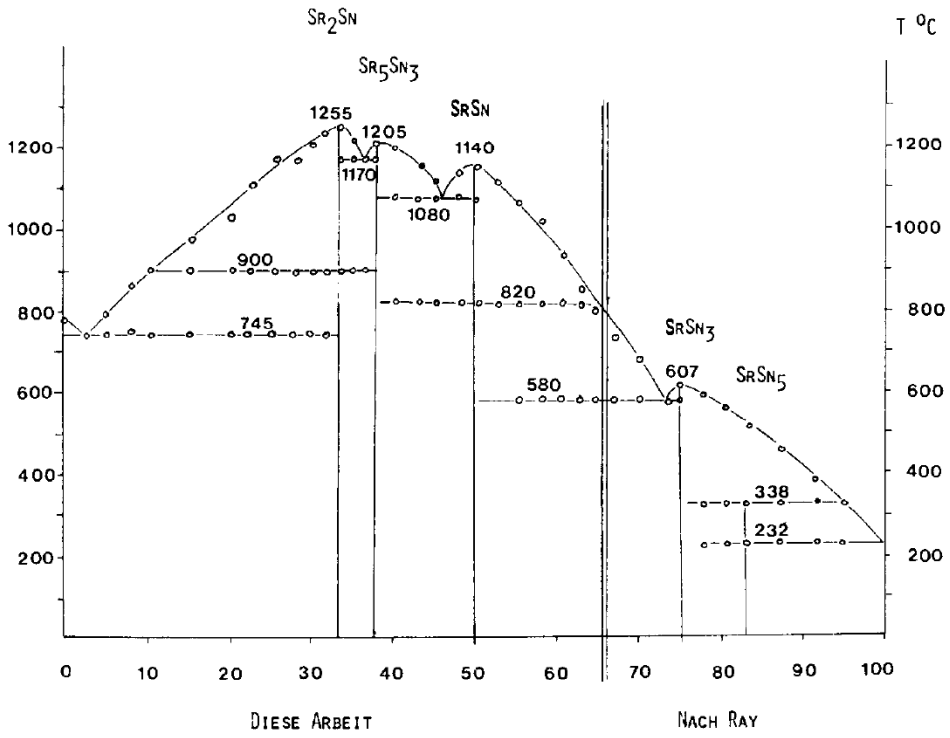

Figure 2.12: Sr-Sn composition phase diagram [69].

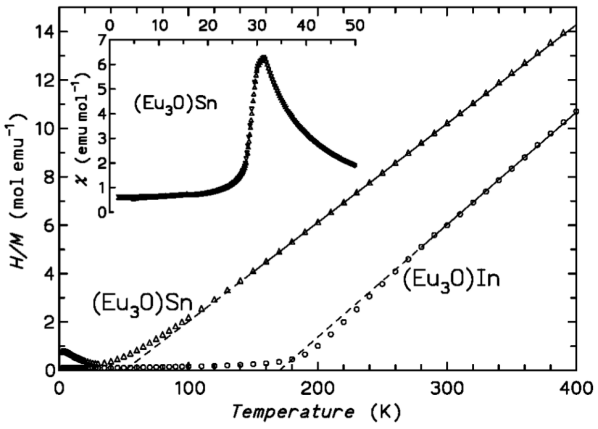

Figure 2.13: Inverse magnetic susceptibility H/M of (Eu_3O)In and (Eu_3O)Sn. The Curie-Weiss fits (continuous lines) and their extrapolations (dashed lines) are show. The inset displays $\chi(T) = M/H$ of (Eu_3O)Sn for $H = 100$ Oe around the antiferromagnetic transition temperature. [72].

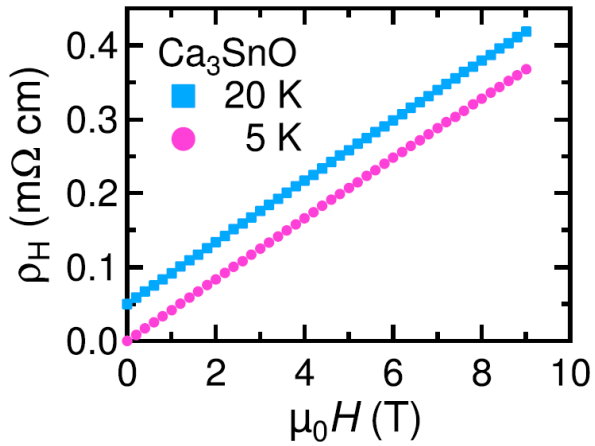

Figure 2.14: Hall resistivity ρ_H of the Ca_3SnO polycrystalline sample measured in magnetic fields up to 9 T taken at 5 and 20 K. The 20 K data are shifted by 0.05 mΩ cm for clarity [73].

$\mu \sim 79$ cm^2 V^{-1} s^{-1} is estimated for these polycrystalline samples, which is lower than high-mobility semiconductors but much higher than metals [73]. This relatively high mobility may be a consequence of linear dispersion near the Γ point in the band structure of Ca_3SnO, where no crossing happens in this trivial insulator.

Thin-films of antiperovskite oxides have been reported for Ca_3SnO, Sr_3SnO, and Sr_3PbO, where Sr_3SnO exhibits semiconducting properties as shown in Fig. 2.15. The Sr_3SnO thin-films, grown using multi-target pulse laser deposition, are ferromagnetic even at room temperature, making them potential dilute magnetic semiconductors. This ferromagnetism was shown to depend on the oxygen pressure during the anealing, where annealing in vacuum enhanced the room temperature ferromagnetism, while oxygen annealing reduces it [67]. The Sr_3PbO thin-films were grown using molecular beam epitaxy show metallic temperatuere dependence that changed in absolute value as a funciton of Sr/Pb flux ratio during growth, illustrated in Fig. 2.16(a). The carrier density and mobility based on Hall measurement at 10 K n_{Hall} and μ_{Hall} as a function of Sr/Pb flux ratio are shown in Fig. 2.16(b). With increasing Sr/Pb, both n_{Hall} and μ_{Hall} decrease, where the n_{Hall} is explained by catio/anion ratio effects and μ_{Hall} is explained by the amount of disorder introduced with different Sr/Pb raios [74]. The Hall coefficient in all the Sr_3PbO thin-films in this report are dominated by holes, which is explained by deficiency in Sr or excess in Pb or O.

The report on Ca_3SnO thin-films grown by pulsed laser deposition includes x-ray photoemission spectroscopy (XPS) resuls, shown in Fig. 2.17, with unusual XPS spectra for Sn [75]. XPS spectra of compound with Sn^{4-} are not reported in literature. The results for Ca are consistent with a 2+ state and result for O are consistent with 2− state, which suggests the unusual spectra of Sn to originate from a 4− state.

Angle-resolved photoemission spectroscopy (ARPES) study on Ca_3PbO demonstrate a band

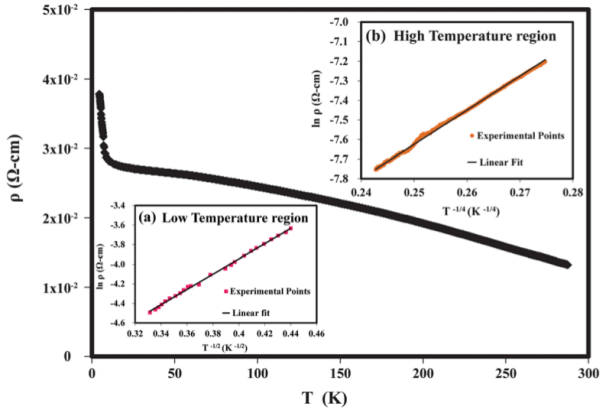

Figure 2.15: Resistivity as a function of temperature (5 K-285 K). Bottom left inset (a): lnρ vs. $T^{-1/2}$ at low temperature (5-10 K). Top right inset (b): lnρ vs. $T^{-1/4}$ at high temperature (170-285 K) along with best fit results obtained by least-square fitting [66].

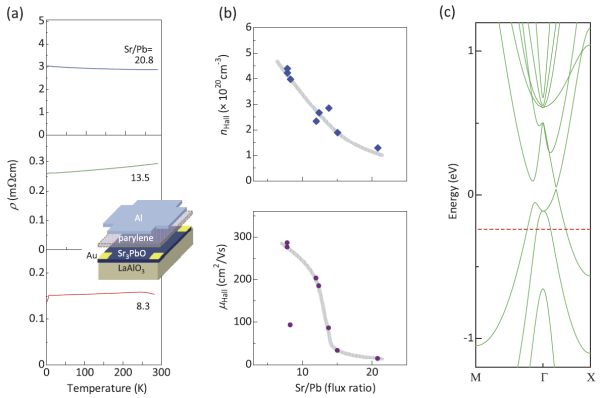

Figure 2.16: (a) Temperature dependence of resistivity for Sr_3PbO films grown with different Sr/Pb flux ratio. The inset in the middle panel shows schematic structure of Sr_3PbO film with contacts and capping layers. (b) At 10 K, n_{Hall} (top panel) and μ_{Hall} (bottom panel) versus Sr/Pb flux ratio. Gray solid lines are guide to the eye. (c) Band diagram based on first-principles calculation (green solid line) and estimated position of E_{F} using an input from n Hall (red dashed line) [74].

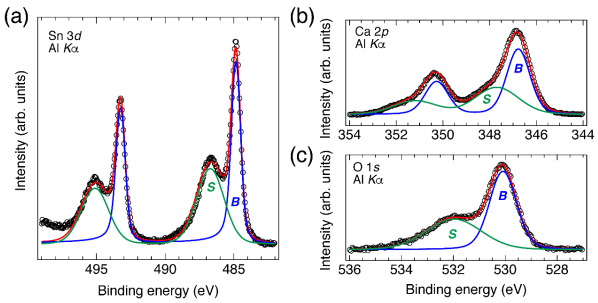

Figure 2.17: (Color online) XPS spectra from the Ca_3SnO film for (a) Sn-3*d*, (b) Ca-2*p*, and (c) O-1*s* core levels. The fitting results are overlaid by green, blue, and red curves, which correspond to the surface component (S), bulk component (B), and their summation, respectively [75]

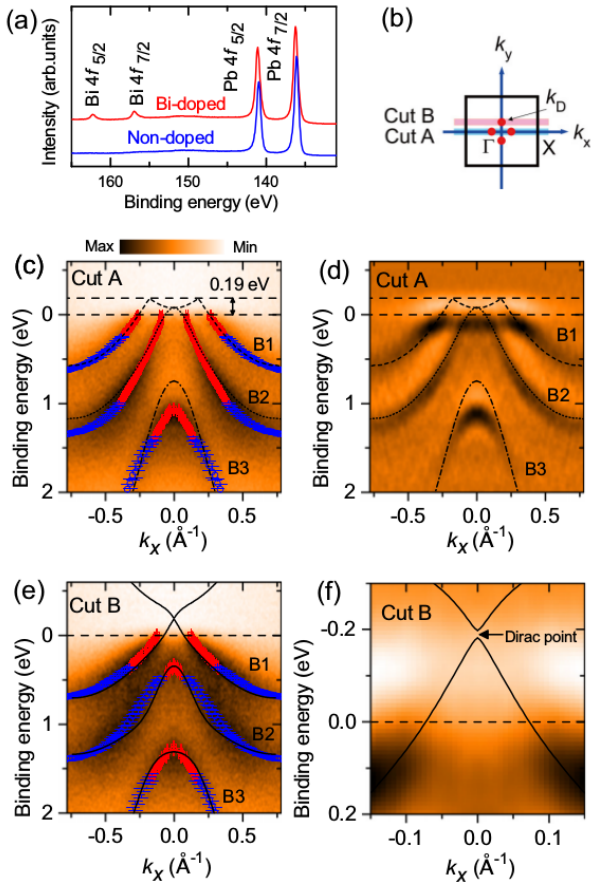

Figure 2.18: (a) Core-level photoemission spectra of Ca_3PbO and $Ca_3Pb_{0.92}Bi_{0.08}O$. (b) 2D cross section of the BZ of Ca_3PbO. Red dots represent the four 3D Dirac points in the plane, denoted as k_D. (c), (e) ARPES intensity plots along cuts A and B, respectively, measured for a Bi-doped crystal. The peak positions of the momentum distribution curves (MDCs) and energy distribution curves (EDCs) are plotted by the red open squares and blue open circles, respectively. (d), (f) Second-derivative ARPES spectra along cuts A and B, respectively. Black dashed and solid lines illustrate the results of band structure calculations for cut A and B, respectively [76].

disperssion near the Fermi level that does not contradict the band structure calculations, but the Dirac crossing was not clearly observed in Ca_3PbO [76]. Doping Bi at the Pb site shifts the Fermi level up slightly upwards, and reveals one of the crossings as demonstrated in Fig. 2.18. Surprisingly, the doping of Bi for Pb does not alter the electronic structure. These results push the antiperovskite oxide system, including Sr_3SnO, as a promising platform to investigate 3D Dirac systems.

Chapter 3

Experimental Setup

In this chapter, I will explain our experimental procedure, excluding sample preparation as it will be discussed in detail in the next chapter. The experimental setup of various physical measurements, magnetization, transport, and heat capacity will be discussed. Although mainly performed by collaborators, the Mössbauer and NMR set up will be discussed briefly, as results of these measurements are relevant to various chapters in this thesis. As Sr_3SnO is air-sensitive, the precautions to assure the protection of the samples during the measurements will be mentioned in each section of this chapter.

3.1 Physical Characterization

3.1.1 Powder X-ray Diffraction (XRD)

Powder X-ray diffraction (XRD) was measured at room temperature using a commercial diffractometer (Bruker AXS, D8 Advance) utilizing CuK_α radiation equipped with a nickel monochrometer and a one-dimensional array of detectors. The antiperovskite oxide samples were unstable in air, so a technique was developed to maintain the samples under inert environment using 12.5-μm-thick polyimide film (Kapton sheet, DuPont) attached to the sample stage using a ring of vacuum grease (Dow Corning Toray, high vacuum grease) around the sample, as shown in Fig. 3.1. Samples prepared in this fashion were stable in air for a few hours, before they slowly decomposed into tin and $Sr(OH)_2$. A typical pXRD measurement times was 30 to 220 min. The samples were not spun during the measurement to avoid tearing the Kapton sheet due to contact with

anti-scatter blade. The collected data was fitted using the program Topas 4.3. The various instrument parameters were calibrated using a standard reference of Al2O3, provided by National Institute of Standards and Technology. A plastic dome was also used to keep the samples under inert environment, but this required removing the anti-scatter blade, resulting in large background noise.

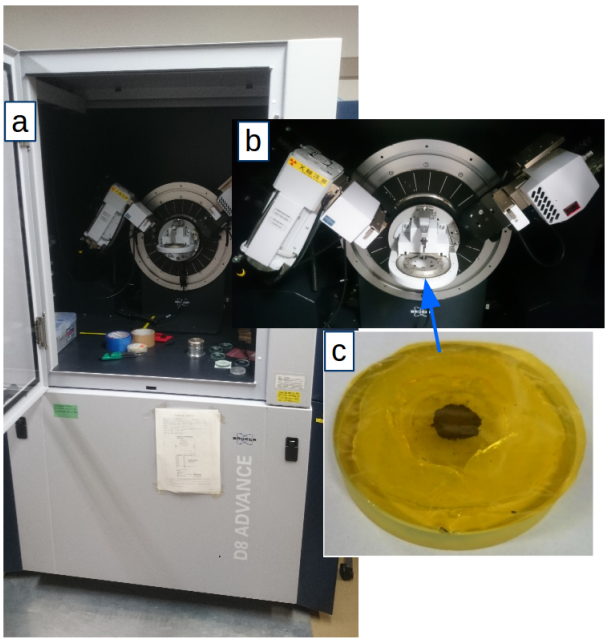

Figure 3.1: (a)Bruker AXS, D8 Advance used for XRD diffraction experiment. (b) The X-ray source on the left and detector on the right, and sample holder goes in the middle. (c) Typical glass sample holder setup for air sensitive samples with powdered sample in middle (black), Kapton sheet on top, and vacuum grease between the glass and the Kapton sheet.

3.1.2 High Energy XRD

High-energy XRD measurement at various temperatures were performed using a DebyeScherrer camera at the beam line BL02B2 of the synchrotron facility SPring-8. Two detectors were used for the measurement, one for lower angles (0-35) and one for higher angles (30-80). Each of the detectors collects data for the time specified to the machine consecutively (not simultaneously), meaning that t = 120 s implies an actual measurement of t = 240 s when considering both detectors. The wavelength of X-ray used was λ = 0.42073 nm, which was calculated by using CeO_2 as a standard. Sample powder was sealed in a plastic/quartz capillaries, inner diameter 0.5 mm, under nitrogen atmosphere to prevent decomposition of the air-sensitive $Sr_{3-x}SnO$ samples. Samples measured at room temperature only were sealed in plastic capillaries, while those measured

at low and high temperatures were sealed in quartz capillaries. The capillaries were rotated during measurements to reduce preferential orientation of crystallites, if such a preferential orientation exits. Helium gas was used to measure the XRD down to 30 K, while nitrogen gas was used for high temperature measurements up to 1000 K. Low temperature data was collected at 90, 60, and 30 K, while high temperature data were collected at 100 K intervals between 400 and 1,000 K. Measurements in the absence of control gas were assumed to be done at 300 K for analysis, which is approximately the room temperature. Jana2006 was used to perform structural refinements on some of the collected diffraction patterns.

3.1.3 SEM/EDX

Energy-dispersive X-ray spectra were collected using a commercial detector (AMETEK Inc, model: Element) equipped on a scanning electron microscope (SEM; KEYENCE, model: VE-9800), shown in Fig. 3.2 below. In a glove box filled with argon, the sample powder was placed on a metallic stage with a conductive double-sided tape made from carbon and aluminum (Nisshin EM Co., Ltd., catalog number: 7321). The samples were exposed to air during the evacuation inside the SEM, which likely results in decomposition on the surface of the sample. The Sr:Sn ratio in a larger area should reflect the ratio in the sample prior to decomposition. Incident electrons with an energy of 15 keV and spot size of 16 were used. To construct the element mappings, we integrated 16 frames for each sample. Every pixel of a frame was obtained by collecting the emitted X-ray for 100 ms.

Figure 3.2: SEM with commercial X-ray detector.

3.2 Magnetization Measurements

3.2.1 AC Susceptibility

AC susceptibility measurements were performed with a commercial physical properties measurement system (Quantum Desing, PPMS) using a set of coils developed by S. Yonezawa *etal*. [77] and a commercial puck for measurements down to 1.8 K. Measurements down to 0.1 K were performed using an adiabatic demagnetization refrigerator and the same set of coils. The $Sr_{3-x}SnO$ samples were covered with grease, or inserted into a sample holder and sealed with grease, inside an argon glovebox before placing inside the coil for measurement.

3.2.2 SQUID Magnetometry

A commercial superconducting quantum interference device (SQUID) magnetometer (Quantum Design, MPMS) was used to measure the direct current magnetization M. Samples were covered with grease in an argon environment, then placed inside the straw for measurement. Some samples were sealed inside a capsule with kapton tape, which allowed us to recover the sample for other measurements after the M measurement. However, the capsule/Kapton tape setup resulted in a stronger background paramagnetic signal. Degaussing was performed prior to measurement to ensure the accuracy of the applied field. Furthermore, the remnant field inside the MPMS was occasionally measured using a reference sample (Pb, 99.9999%), and found to be $\leq$ 0.1 mT after degaussing. The M of Pb sample at 2 K was measured at different fields between -1 mT to 1 mT to determine the remnant field. Typically low fields were used in this measurements to observe the superconducting state of $Sr_{3-x}SnO$ samples, and only a few measurements were performed under large magnetic fields to observe the samples in the normal state. The sequences used with the MPMS include zero-field-cooling (ZFC) and field-cooling (FC) with different heating/cooling rates.

3.3 Transport Measurement

The transport measurements performed on $Sr_{3-x}SnO$ samples include resistivity and Hall measurements. The resistivity measurement was performed using a four-probe method from 1.8 to 300 K. A fifth wire was attached to the samples to perform Hall measurement. A sample with a typical size of 2.0×2.0×0.6 mm^3, and 50-μm-diameter gold wires were attached using silver epoxy (EPOXY TECHNOLOGY, H20E) inside an argon filled glovebox. A layer of vacuum grease (Apiezon, N-grease) was applied over the samples inside the glovebox to protect them from contact with air. The samples were cooled during resistivity and hall measurement using a commercial apparatus (Quantum Design, PPMS). The orientation of the sample with respect to direction of magnetic field was taken note of when Hall measurement was performed.

Figure 3.3: $Sr_{3-x}SnO$ sample with five gold wires attached using silver epoxy for resistivity and Hall measurement using PPMS. Sample was covered with N-grease before moving the device from glovebox to PPMS.

3.4 Heat Capacity

Specific heat C_P was measured with a thermal relaxation method using a commercial calorimeter (Quantum Design, PPMS model 6000) from 300 K to 0.35 K. A chunk of polycrystalline $Sr_{3-x}SnO$, showing superconductivity from M result, was used for C_P measurement. A ^{4}He calorimeter puck was used for measurements down to 1.8 K, while a ^{3}He calorimeter puck was used for C_P measurement down to 0.35 K. The samples were mounted to a 3 mm × 3 mm alumina platform, and fixed with Apizon N grease to provide good thermal contact with the platform. Thermometer and heater are attached on the back of this platform, which are controlled electrically by thin wires. These wires also provide thermal connection between the platform and the rest of the puck. The specific heat of the sample is evaluated by subtracting the background contribution from the total specific heat. This is achieved with a two step process, where the specific heat without the sample (platform, grease, etc.) is measured first, where a larger than usual amount of grease was added to the platform. In the second step, the sample is added to the puck for the total specific heat measurement. Antiperovskite oxide samples were covered with grease during transport from glovebox to the calorimeter puck, so some of the excess grease used in the background measurement was removed. This two step process of measuring specific heat was performed under different applied magnetic fields. A turbo molecular pump was used to maintain the pressure of the sample chamber below 10^{-5} Torr during the measurement.

The normal state C_P was collected under an applied field of 2 T, while the superconducting

state data was collected under no applied magnetic field. It should be noted that the superconducting transition of $Sr_{3-x}SnO$ samples was reflected with a small jump in C_P due to small γ at 0 K. A number of sequences were used to emphasize the transition at T_c, with varying the δT, measurement time, and the number of measurements included in the average $C_P(T)$ in the temperature interval T to $T + \delta T$.

3.5 Mössbauer Spectroscopy

The conventional transmissionMössbauer spectroscopy was performed using ^{119m}Sn γ-ray source in a $CaSnO_3$ matrix with a nominal activity of 740 MBq. The origin of the isomer shift was chosen to be that of $BaSnO_3$. Approximately 40 mg of $Sr_{3-x}SnO$ samples were mixed with BN and polyethylene, which was then pressed into a circular pellet. The pressed pellet was sealed inside multiple plastic bags and consecutively to limit contact with air. All sample preparation was done inside an argon filled glovebox first, then the samples were transported to the measurement apparatus. The measurement apparatus is composed of two main parts, the γ-ray source, $Ca^{119m}SnO_3$ in our case, and a detector on the other side of the sample. The source is moving with varying speed with respect to the sample, and the γ ray passing through the sample is absorbed at a specific velocity, the peak in the isomer shift. To measure the Mössbauer at low temperatures, samples were cooled using a He closed-cycle refrigerator. Measurements were performed by S. Kitao.

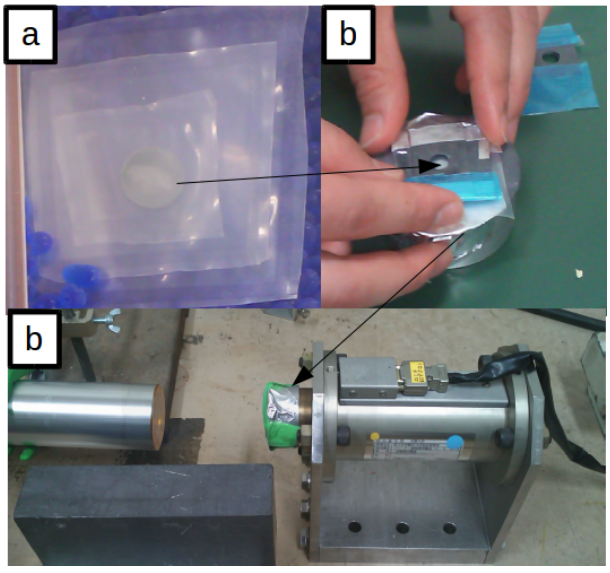

Figure 3.4: (a) Pellet of $Sr_{3-x}SnO$ and BN inside multiple polyethylene bags. (b) Sample placed inside holder for Mössbauer spectroscopy experiment. (c) Setup during Mössbauer spectroscopy measurement with γ-ray source, $Ca^{119m}SnO_3$, to the left and γ-ray detector to the right.

3.6 NMR

A conventional spin-echo technique was utilized for the NMR measurement of $Sr_{3-x}SnO$ samples. ^{119}Sn-NMR spectra (nuclear spin $I = 1/2$, and nuclear gyromagnetic ratio $\gamma/2\pi = 15.877$MHz/T) were obtained as a function of magnetic field in a fixed frequency. The NMR measurements were done at $\mu_0 H \sim 6$T. The Knight shift of the sample was calibrated by the Sn metal signals. The nuclear spin-lattice relaxation rate $1/T_1$ was determined by fitting the time variation of the spin-echo intensity after saturation of the nuclear magnetization to a theoretical function for $I = 1/2$.

The Knight shift K, which is the measure of the local susceptibility at the nuclear site, is defined as the ratio between the resonance frequency of an isolated nucleus $\omega_0 (= \gamma H_0)$ and the frequency difference due to the averaged hyperfine field $< H_{\rm hf} >$ at the nuclear spin $\Delta\omega = \omega_{\rm res} - \omega_0$, that is, $K = (\omega_{\rm res} - \omega_0)/\omega_0|_{H=H_0} = (H_0 - H_{\rm res})/H_{\rm res}|_{\omega=\omega_0}$ where the last term is expressed using resonant magnetic fields. Generally, the Knight shift is related to the bulk magnetic susceptibility $\chi = N_{\rm A}\gamma\mu_{\rm B} < s > /H_{\rm res}$ through the hyperfine coupling constant $A_{\rm hf}$. The relationship is expressed as, $K = A_{\rm hf}/(N_{\rm A}\gamma\mu_{\rm B})\chi$ where $N_{\rm A}$ is the Avogadros number and $\mu_{\rm B}$ is the Bohr magneton.

The nuclear spin-lattice relaxation rate $1/T_1$ is defined as the characterization rate at which the longitudinal M_z component of the nuclear magnetization vector recovers toward its thermodynamic equilibrium. In a FL state, $1/T_1$ can be expressed as $1/T_1 = (4\pi/\hbar)[(\gamma N\hbar A)^2/N_A^2]N^2(E_{\rm F})k_{\rm B}T$ where $N(E_{\rm F})$ is the density of states at Fermi Energy.

To prevent sample degradation by air and/or moisture, polycrystalline samples were mixed with stycast 1266, and the mixture was solidified with random crystal orientation. All procedures were done in a glove box filled with argon. Sample preparation was mainly by M. Oudah, while the measurement was performed by S. Kitagawa.

3.7 Band Structure Calculations

In order to investigate the band structure of $Sr_{3-x}SnO$, we performed first-principles calculations of the stoichiometric and deficient $Sr_{3-x}SnO$ using WIEN2k [78], which uses full-potential linearized-augmented plane-wave plus local orbitals method. As well as, AkaiKKR (also called Machikaneyama) [79], utilizing the Korringa-Kohn-Rostoker Green function method [80, 81]. A brief description of the parameters used in these calculations are described for each program below.

3.7.1 WIEN2k

For WIEN2k calculation, the Perdew-Burke-Ernzerhof (PBE) generalized gradient approximation [82] was used as the exchange-correlation functional and spin-orbit coupling effects were included in the calculation. Paramagnetic states were assumed for both Sr_3SnO and $Sr_{3-x}SnO$ and spin-polarized calculations were note performed. The crystalline structure reported exper-

imentally [14] was used for the calculation of Sr_3SnO. In the case of WIEN2k, the radius R of the muffin-tin sphere of each atom was set as the following: $R_{Sr} = R_O = 2.39$ bohr and $R_{Sn} = 2.50$ bohr. We set the plane-wave cut off $RK_{max} = 7.0$, the highest angular momentum plus one $l_{max} = 10$, maximum magnitude of the largest vector in charge density Fourier expansion $G_{max} = 12$, and separation energy between the valence and core states -6 Ry. To see the effect of the strontium deficiency, we tried calculation on hypothetical superstructures of $Sr_{3-x}SnO$ with different patterns of the deficiency. In one superstructure strontium atoms are missing in certain layers, while in the other superstructure the vacancies take alternating positions in consecutive layers, details shown in later chapter. The k meshes used in these $Sr_{3-x}SnO$ calculations are $10 \times 10 \times 10$ or $10 \times 10 \times 5$, depending on the size of the unit cell in the calculation. The k paths for band-structure plots are chosen based on the unit cell used in the calculation.

3.7.2 AkaiKKR

For AkaiKKR calculation, the PBE generalized gradient approximation [82] was also used as the exchange-correlation functional. Spin-orbit coupling effects were included in the calculation, and the muffin-tin radius R was set equal for all atoms $R_{Sr} = R_{Sn} = R_O = a/4$, where a is the lattice constant. The separation between the valence and core states was set to $E_{width} = 1.9$ Ry, and the imaginary part of the energy $E_\delta = 0.0003$ Ry. A k mesh of $8 \times 8 \times 8$ was used for the calculation of $Sr_{3-x}SnO$. For $x \neq 0$ case, calculations of randomly disordered deficiencies were performed using coherent potential approximation [83, 84]. A k path similar to the one chosen in WIEN2k calculation was chosen to allow for comparison. The band structures shown by this AkaiKKR method are a 2D representation of multiple 3D curves, and comparison between the band structures produced in each program can only be compared qualitatively. Some more details on this calculation method are included in a later chapter.

Chapter 4

Synthesis Optimization

In this chapter, I present an overview of the various synthesis methods attempted on antiperovskite oxides, and physical characterization data to demonstrate the quality of samples presented. A few relevant magnetization data are presented, since the search for superconductivity was one of the motivations of this work. The chapter begins with an overview of the work performed on various antiperovskite oxides. Then, the focus is shifted to highlighting the efforts to optimize the synthesis of superconducting $Sr_{3-x}SnO$.

4.1 Exploration of Antiperovskite Oxides

We synthesized various A_3BO compounds including A = Ca, Sr, Yb & B = Sn, Pb. The samples were typically heated to 800-900 °C, but different heating profiles were attempted for each combination of elements to improve the sample quality. We tried different heating/cooling rates and kept the samples at the highest temperature for different times. Good quality Sr_3SnO samples were produced by heating the samples from room temperature to 800 °C over 3 hours and keeping them at 800 °C for 3 hours, then cooling them through quenching in cold water. In these initial samples, stoichiometric amounts of Sr and SnO were loaded in an alumina crucible inside a glovebox, which was then sealed inside a silica tube under vacuum. Alumina crucibles, vacuumed silica tubes, and similar heating profiles were used to produce other antiperovskite oxides, but the starting materials were replaced with Ca, Yb, and PbO. Some of the equipments used for the synthesis of antiperovskite oxide samples are shown in Fig. 4.1. While samples with a mainly

A_3BO phase were being synthesized, and their magnetic properties down to 0.10 K were being investigated, we found superconductivity in Sr_3SnO. One of the initial samples showing signs of superconductivity is shown in Fig. 4.2. Here, the transition from AC magnetization measurement is broad, and the peak in the imaginary part of AC susceptibility is around 1.5 K. It was not clear in this initial sample whether the superconductivity originates from impure Sn after decomposition of the Sr_3SnO during preparation of the sample for the measurement. Nonetheless, we were motivated to further investigate the properties of Sr_3SnO and we improved the quality of samples that eventually led to discovery of the 5 K phase shown in the next section.

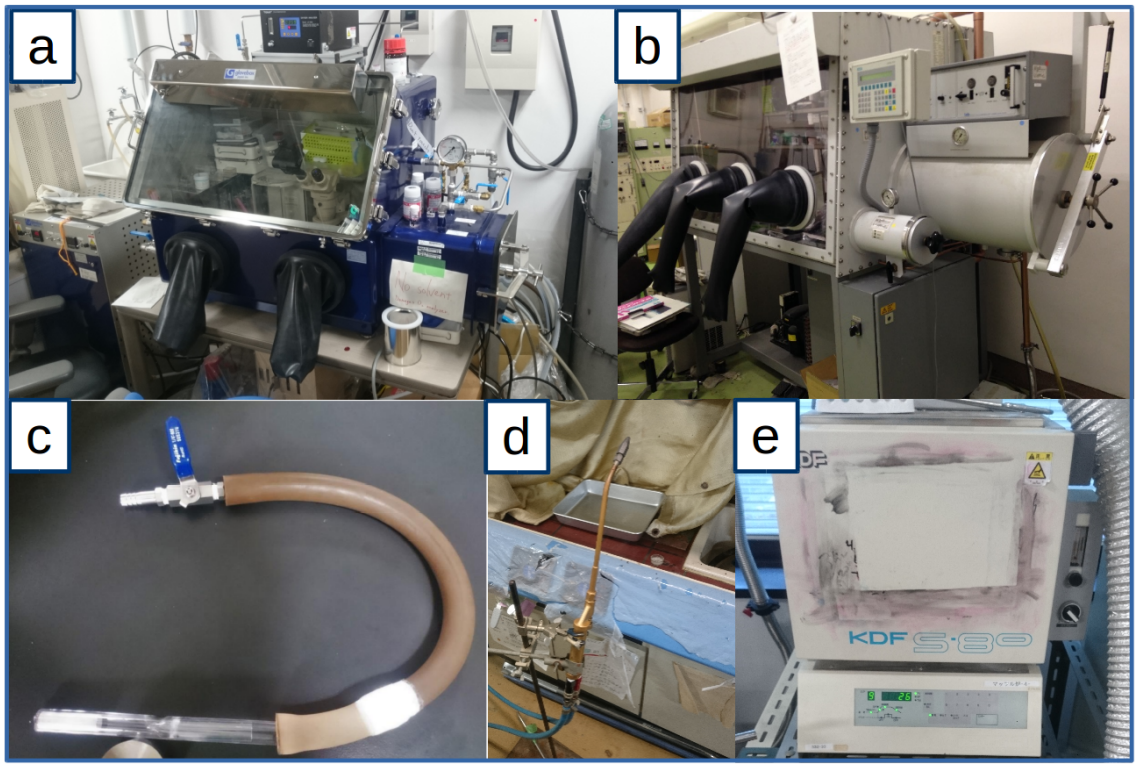

Figure 4.1: (a) Glovebox at Quantum Materials Lab. (b) Glovebox on the 2nd floor of Low Temperature Center (Yoshida-North Campus). (c) Silica tube and alumina crucible with rubber tube used for transporting to vacuum pump. (d) Oxygen-hydrogen torch used to seal silica tube. (e) Box furance used to heat samples up to 1000°C.

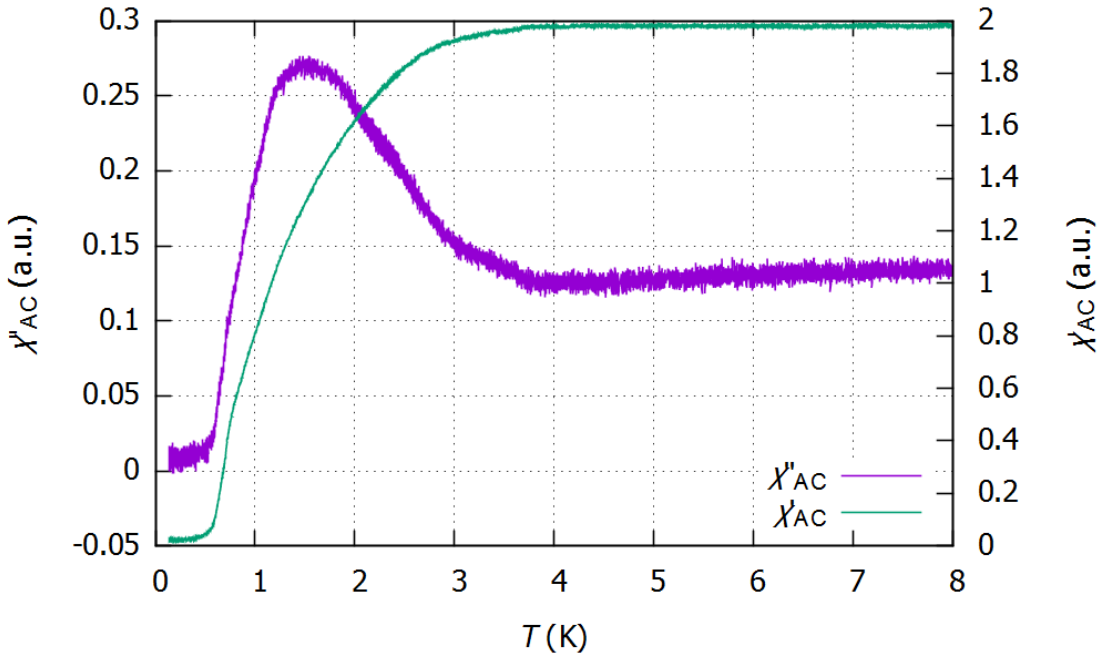

Figure 4.2: χ_{AC} of an initial sample with broad transition, which may originate from impure Sn. Nonetheless, this result motivated to further investigate Sr_3SnO, eventually leading to discovery of the 5 K phase.

4.2 $Sr_{3-x}SnO$ Optimization

Oxides related to the perovskite structure have been playing a leading role in the study of superconductivity during the last three decades. Many of the milestones in high temperature superconductivity were discovered in perovskite oxides such as $La_{2-x}Ba_xCuO_4$ [5, 85], $YBa_2Cu_3O_{7-x}$ [86] and $Bi_2Sr_2CaCu_2O_{8+\delta}$ [87], as well as discovery of the unconventional superconductor Sr_2RuO_4 [6] with evidence for spin-triplet superconductivity [88, 89]. However, the symmetrically equivalent, but oxidation state-inverted analogue, known as the inverse perovskite or antiperovskite (AP) oxide, was away from the focus of experimental investigation by the scientific community, most likely due to its instability in air. The first superconductor among AP oxides, $Sr_{3-x}SnO$, is the one reported in this thesis. This discovery may be the potential beginning of the emergence of a new promising family of AP oxide superconductors [90, 91, 92, 93, 94, 95, 96, 97, 98, 99].

A wide range of oxide compounds exist, including ones crystallizing in the AP and related structures. In general, two formulae for cubic AP oxides are known: $M_3^{1+}O^{2-}A^{1-}$ and $M_3^{2+}B^{4-}O^{2-}$

. In both cases, O^{2-} is octahedrally coordinated by six M, whereas A is cuboctahedrally coordinated by twelve M. In the first case, there are materials known in which M is an alkaline metal or silver and A is a halogen or gold [90, 91, 92, 93, 94, 95, 96, 97, 98, 99]. In the latter, there are materials known in which M is an alkaline earth metal or lanthanoid and B is an indium or a group 14 element [15, 69, 100, 101, 71, 72].

Band structure calculations of AP oxides of the latter formula, containing tin or lead as A and alkaline earth metals as M, have revealed the presence of six equivalent three dimensional Dirac electrons located in the vicinity of the Fermi level in some compounds such as Sr_3SnO or Ca_3PbO [17, 18]. The emergence of Dirac cones is related to a band inversion between the valence band, mainly originating from the p orbitals of tin or lead, and the conduction band, mainly originating from the d orbitals of the alkaline earth metal. These band structures imply nearly closed shell ionic compounds. This is consistent with the observed distances between the alkaline earth and oxygen ions in the crystal structures [1, 69]. Thus, the unusual ionic states of Sn^{4-} and Pb^{4-} are realized. Furthermore, it was predicted that a new topological phase, protected by mirror symmetry of the crystal, is present in some members of this family of AP oxides such as Sr_3SnO [19, 102]. Recently, conelike band dispersion in good agreement with the electronic structure calculations [19] were observed by soft x-ray angle-resolved photoemission spectroscopy of Ca_3PbO single crystals [76]. This strongly supports that some antiperovskite oxides host 3D Dirac fermions.

The first AP oxide superconductor, $Sr_{3-x}SnO$ with a transition temperature T_c of 5 K, was reported very recently by our group [1]. As the parity of the Cooper pairs reflects the orbital texture of the underlying Fermi surface, $Sr_{3-x}SnO$ is a candidate for topological superconductivity, due to the mixing of the Sn-5p and Sr-4d bands at the Fermi level. A recent first-priniciples study on the superconducting properties of Sr_3SnO predicted it to be a topological superconductor with a T_c of 8.38 K [68]. Early samples from our group, showing superconductivity with volume fractions of up to 32%, suffered from uncontrolled evaporation of strontium during synthesis [1]. In fact, the superconducting samples contained two cubic phases, in which the lattice parameters were different by only 0.02 Å . Later we found that the evaporation could be suppressed by synthesizing the samples under argon pressure.

Here details of the argon argon pressure to suppress strontium evaporation as well as the synthesis of Sr_3SnO at temperatures above its melting point. Furthermore, we present powder X-ray diffraction (p-XRD), energy-dispersive X-ray spectroscopy (EDX), direct current (DC) magnetization, and resistivity data for stoichiometric Sr_3SnO and deficient $Sr_{3-x}SnO$ samples. The analysis of the p-XRD data of these improved samples makes it possible to identify the two phases present in the reported superconducting sample that identified one as SrO and the other as $Sr_{3-x}SnO$. This is further supported by EDX measurements. The single-phase stoichiometric Sr_3SnO samples do not show any superconducting transition down to 0.15 K and exhibit semiconducting behavior in contrast to metallic behavior for the strontium deficient sample in the temperature dependent resistivity (Shown in Fig. 7.3 in 7.2). Further, we reveal a strong effect of small amounts of non-magnetic impurities in the strontium starting material on superconductivity.

The magnetic shielding of a strontium deficient $Sr_{2.5}SnO$ sample exhibits a diamagnetic volume fraction of approximately 100% at 2 K with a superconducting onset of 5.2 K.

The samples were synthesized following our procedure in section 4.1 (Method A) and with the modified methods B and C. For all procedures, the strontium (specification below) and the SnO powder (Furuuchi, 99.9%, 169.4 mg, defined as 1.0 molar equivalent) were loaded inside an argon-filled glovebox into a crucible. After sealing the crucible in quartz tubes under vacuum (pressure $P < 10$ Pa) or argon pressure, the quartz tubes were placed at an approximately 45°angle into a box furnace, and the appendant temperature program was applied. After water-quenching, the quartz tubes were opened, stored, and prepared for further experiments inside an argon-filled glovebox.

Method A. Synthesis under vacuum. The synthesis of samples A-1 and A-2 was performed in alumina crucibles (SSA-S, $11 \times 42 \times 1.5$ mm ^{3}) sealed in quartz tubes under vacuum. For the sample A-1 clean cut strontium chunks (Furuuchi, chunks stored in oil, 99.9%, 413.3 mg, 3.75 eq.) and for the sample A-2 clean cut strontium chunks (Furuuchi, chunks stored in oil, 99.9%, 330.6 mg, 3.0 molar equivalent) were used. The sealed quartz tubes were heated to 800 °C over 3 h and kept at 800 °C for 3 h before water-quenching. In both cases, a metallic shining black surface on the inside of the quartz tube wall could be observed, clearly indicating an evaporation of a compound outside of the crucible. For batches A, B, and C in Chap. 5, the synthesis was the same as for A-2. Batch E in Chap. 5 is synthesized same as A-1 above.

Method B. Synthesis under argon pressure. The synthesis of samples B-1, B-2 and B-3 was performed in alumina crucibles (SSA-S, $11 \times 42 \times 1.5$ mm ^{3}) sealed in quartz tubes under 30 kPa of argon pressure at room temperature. For the sample B-1 clean cut strontium chunks (Furuuchi, chunks stored in oil, 99.9%, 331.1 mg, 3.00 eq.), for the sample B-2 clean cut strontium chunks (Furuuchi, chunks stored in oil, 99.9%, 271.6 mg, 2.5 eq.)) and for the sample B-3 dendritic strontium pieces (Sigma Aldrich, dendritic pieces stored under argon, 99.99%, 271.6 mg, 2.5 eq.) were used. The sealed quartz tubes were heated to 825 °C over 3 h and kept at 825 °C for 3 h before quenching. Batch D in Chap. 5 is synthesized with dendritic strontium pieces (Sigma Aldrich, dendritic pieces stored under argon, 99.99%, 271.6 mg, 2.46 eq.). All of the samples presented in Chap. 6 were synthesized using this method and varying the ratio of Sr:Sn based on x in $Sr_{3-x}SnO$, and the total mass of the samples was approximately 0.5 g.

Method C. Synthesis at temperatures above the melting point of Sr_3SnO. The synthesis of the sample C was performed in tantalum crucibles (Japan Metal Service Co. Ltd., 99.95%, $14 \times 35 \times 0.5$ mm ^{3}) sealed under 23 kPa of argon pressure. Dendritic strontium pieces (Sigma Aldrich, dendritic pieces stored under argon, 99.99%, 341.6 mg, 3.1 eq.) were used, as shown in Fig. 4.4. The sealed quartz tubes were heated to 825 °C over 40 min and kept at 825 °C for 20 min. Subsequently, they were heated up to 1200 °Cin 30 min and kept there for 2.5 h to melt the Sr_3SnO before quenching in water. After water-quenching, the samples were heated up to 900 °C over 1 h and kept there for 48 h to improve the homogeneity and crystallinity before they were quenched in water for a second time.

Samples synthesized under vacuum, as in our initial method (Method A, as the on mentioned

in Section 4.1), show a metallic shiny black surface on the inside of the quartz tube, as shown in Fig. 4.3. Now we identified this black surface as different Sr_xSi_y phases by p-XRD. Therefore, evaporated strontium reduces the SiO_2 of the quartz tube to form this dark surface. The amount of evaporating strontium varies from 12% to 25% of the total strontium loading and makes it impossible to control the strontium content in the final product.

We increased the strontium loading to compensate for the evaporated material to synthesize a pure stoichiometric Sr_3SnO phase to compare its superconducting and electrical properties to the ones of $Sr_{3-x}SnO$ of our initial samples (Method A, stoichiometric starting materials). In sample A-1, the evaporation and excess of strontium compensated each other, as deduced from the final weight of product in the crucible. The p-XRD of this sample exhibits only one single cubic phase and no impurities. Therefore, it is considered as stoichiometric Sr_3SnO. However, most probably due to a low crystallinity the peaks are very broad, and hence the presence of an additional minor cubic phase with a slightly larger lattice parameter cannot be excluded with certainty.

Figure 4.3: Silica tubes with $Sr_{3-x}SnO$ samples synthesized in alumina crucibles under vacuum (left and middle pictures) showing varying evaporation of Sr. Synthesis with 0.3 atm argon pressure (right) shows almost no evaporation of Sr outside of crucible.

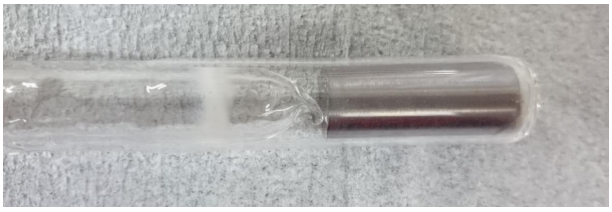

Figure 4.4: Tantalum crucible inside glass tube for synthesis of Sr_3SnO at 1200 °C.

The evaporation can be suppressed by sealing the quartz tubes under an argon atmosphere of 30 kPa at room temperature (Method B), corresponding to 111 kPa at 825 °C with the assumption of ideal gas behavior. The contrast in evaporation on the surface of the quartz tube for

Table 4.1: Summary of the most significant synthesis parameters and the superconducting volume fraction estimated from DC magnetization $M(T)$ data of six different representative batches. No demagnetization correction has been performed on the zero field cooling volume fraction.

Sample	Product	Starting Material	P_{Ar} (at T_{room})	T_{max} (^{o}C)	Sr purity (%)	Superconducting volume fraction at 2 K (%)
A-1	Sr_3SnO	3.75Sr + SnO	0.0 atm	800	99.9	<1.5
A-2	$Sr_{3-x}SnO$	3.0Sr + SnO	0.0 atm	800	99.9	23
B-1	Sr_3SnO	3.0Sr + SnO	0.3 atm	825	99.9	0.0
B-2	$Sr_{2.5}SnO$	2.5Sr + SnO	0.3 atm	825	99.9	64
B-3	$Sr_{2.5}SnO$	2.5Sr + SnO	0.3 atm	825	99.99	105
C	Sr_3SnO	3.1Sr + SnO	0.23 atm	1200	99.99	0.0

samples synthesized with Methods A and B is shown in Fig. 4.3. Due to the successful suppression, it is now possible to control the strontium content in the final product and to investigate the dependence of the superconductivity as well as the emergence of the second cubic phase on the strontium deficiency (Fig. 4.5(c)). Samples synthesized with 3 molar equivalents or more of strontium are single phased and show high crystallinity (Fig. 4.5(b)). Decreasing the strontium loading leads to the emergence of a second cubic phase with a 0.02 Å larger lattice parameter (Fig. 4.5(c)). The difference in the lattice parameters of both phases stays at 0.02 Å, independent from the strontium loading. The diffraction pattern of initial samples showed two similar cubic phases, and we suspected that this phase splitting is due to different strontium contents in the two different $Sr_{3-x}SnO$ phases. As improved quality samples synthesized under argon pressure have an improved crystallinity, resulting in narrower peak shapes in the p-XRD, the peaks belonging to the two different cubic phases overlap less and can be analyzed more carefully.

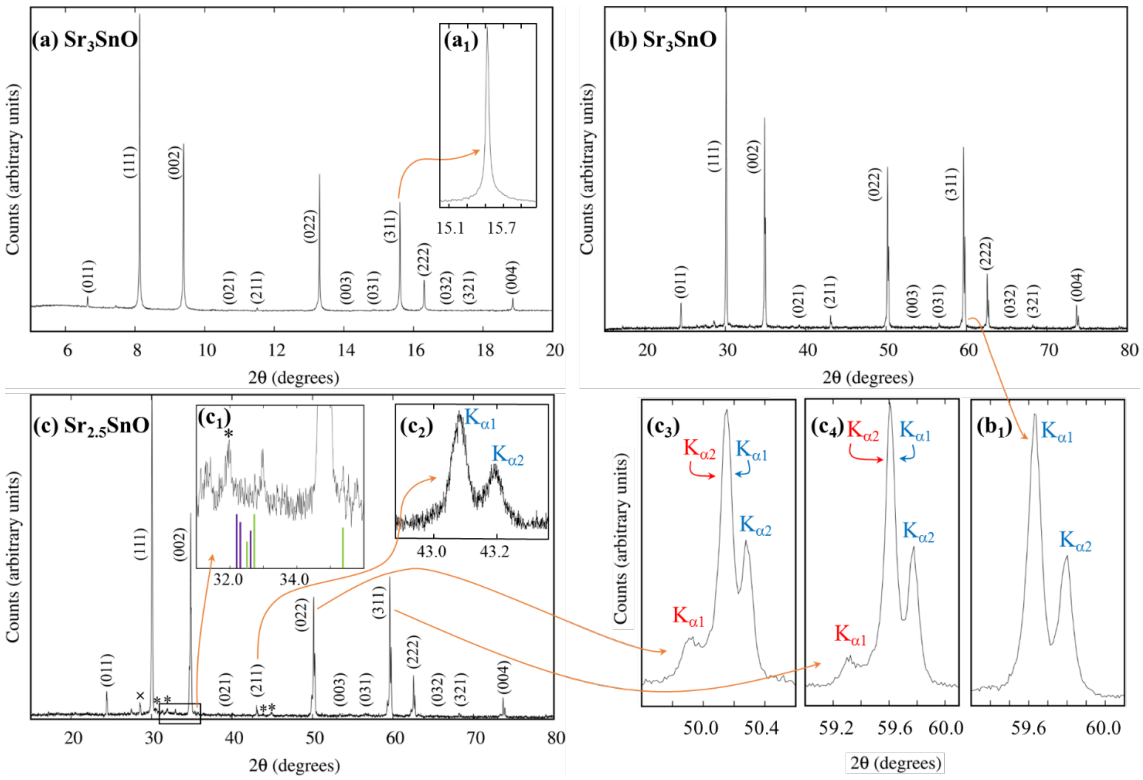

Figure 4.5: Powder X-ray diffraction patterns of $Sr_{3-x}SnO$ at room temperature [2]. The intensities are in linear scales. The diffraction pattern (a) was obtained at the synchrotron-radiation facility SPring-8 with an X-ray wavelength of $\lambda = 0.42073$ Å The diffraction patterns (b) and (c) were obtained with a laboratory-based diffractometer utilizing Cu-$K_{\alpha 1}$ ($\lambda = 1.54$ Å) radiation. (a) and (b) are for stoichiometric and non-superconductive Sr_3SnO of Sample C and B-1, respectively. (c) is for the superconductive $Sr_{2.5}SnO$ Sample B-2. The insets are magnifications of certain peaks or areas. The green and purple bars in inset (c 1) indicate the expected position and intensity (PDF-2 database: PDF010734901 for $SrSn_3$ and PDF010723942 for $SrSn_4$) of the three most pronounced peaks of the only two known superconducting Sr-Sn-alloys $SrSn_3$ and $SrSn_4$, respectively. For the diffraction patterns of the stoichiometric batches (a) and (b) only the primitive cubic Sr_3SnO phase can be observed. For (b) and (c) a splitting of the peaks due to $K_{\alpha 1}$ and $K_{\alpha 2}$ radiation is present. The additional splitting in the peaks of (c) is due to an additional face centered cubic SrO phase. The peaks originating from the SrO phase ($a = 5.160$ Å) are indicated by $K_{\alpha 1}$ or $K_{\alpha 2}$ in red in the insets (c3) and (c4). The ones originating of the $Sr_{2.5}SnO$ phase ($a = 5.137$ Å) are indicated by $K_{\alpha 1}$ or $K_{\alpha 2}$ in blue in the insets (c2), (c3), (c4) and (b1). In inset (c) peaks of a SnO and tin impurity (PDF-2 database: PDF000130111 for SnO and PDF030650296 for tin) are marked by an x and asterisks, respectively.

A diffraction pattern of such a new Sample B-2 is shown in Fig. 4.5(c). The lattice parameter of the main cubic phase is 5.137 Å and the one of the minor phase 5.160 Å. Recently, a lattice

parameter of 5.139 Å for Sr_3SnO single crystals was reported [14]. Hence, it was in agreement with our main phase. The lattice parameter of the minor phase agrees with 5.160 Å, reported for SrO [103]. Additionally, the peak intensity ratios of the (111), (200), (220) and (311) peaks are expected to be different in Sr_3SnO and SrO. The leftmost peak of the three peaks present for each of these four diffraction planes belongs exclusively to the minor phase (see the peaks marked with red $K_{\alpha 1}$ in Fig. 4.5(c3) and (c4) as an example for the (220) and (311) diffraction planes). The intensity ratios of these leftmost peaks fit to the one expected for SrO and the one of the rightmost peaks, originating exclusively from the major phase, to the one of Sr_3SnO. To gain further support for the presence of SrO, one of the low intensity peaks (211), expected to be only present in the primitive cubic Sr_3SnO and not in face-centered cubic SrO, was measured exclusively overnight (see magnified peak in Fig. 4.5(c2)). No splitting in two phases is present in this peak, indicating that no second primitive cubic, but a face-centered cubic phase is present. Furthermore, issues with alkaline earth oxide impurities is reported in literature known for the synthesis of bulk [71, 14] and thin film [74] antiperovskite oxides. Therefore, we conclude that the face-centered cubic phase is SrO.

One SnO (superconducting only under pressure) [104] and four very small tin (T_c = 3.7 K) [105] impurity peaks in Fig. 4.5(c) are marked with an x and asterisk, respectively (PDF-2 database: PDF000130111 for SnO and PDF030650296 for tin). However, due to the small intensity an unambiguous identification by p-XRD is not possible. The EDX results presented in Fig. 4.6(a) show a small area containing only tin. Additionally, the DC magnetization $M(T)$ curves occasionally show a very small anomaly around 3.7 K. Hence, we conclude a small tin impurity is very likely.

Due to the SrO and tin impurity the precise stoichiometry of the final AP oxide phase is challenging to determine. The strontium deficiency might be slightly bigger than expected from the initial strontium loading. Furthermore, an oxygen deficiency is possible. However, considering that Sr_3SnO without oxygen could not be synthesized despite attempts during work on Sr-Sn phase diagrams [15, 69], a significant oxygen deficiency is unlikely. It is possible that small amounts of oxygen are provided through a reaction with the alumina crucible or from another unknown source. Due to these uncertainties in the strontium deficient sample, its molecular formula is set into quotation marks in this report.

Two Sr-Sn-alloys are known to be superconducting: $SrSn_3$ (T_c = 5.4 K) [61] and $SrSn_4$ (T_c = 4.8 K) [62]. The green and purple bars in inset (c1) of Fig. 4.5 indicate the expected position and intensity (PDF-2 database: PDF010734901 for $SrSn_3$ and PDF010723942 for $SrSn_4$) of the three most pronounced peaks of $SrSn_3$ and $SrSn_4$, respectively. The peak positions do not match to those of the experimental p-XRD data. Hence, the presence of crystalline $SrSn_3$ and $SrSn_4$ can be excluded.

Scanning electron microscopy (SEM) and energy-dispersive X-ray (EDX) spectroscopy was performed on $Sr_{2.5}SnO$ of Sample B-2 , see Fig. 4.6(a). Unfortunately, during some parts of the procedure we did not succeed in protecting the samples from air. Therefore, we could not maintain flat surfaces and reliable quantitative results for the element ratios. However, the EDX

images clearly show that the distributions of oxygen (red), tin (blue) and strontium (green) are very similar in a major part of the samples surface, supporting the dominance of the $Sr_{3-x}SnO$ phase and excluding a significant amorphous impurity with a different composition. The orange circles mark an area containing only tin and the white circles an area containing strontium and oxygen. These EDX results are in accordance to our p-XRD data, see Fig. 4.5(b), which shows $Sr_{3-x}SnO$ as dominant phase with SrO oxide and tin as impurities. In general, much more areas containing only strontium and oxygen could be identified by EDX than areas containing only tin, as also expected from the p-XRD data.

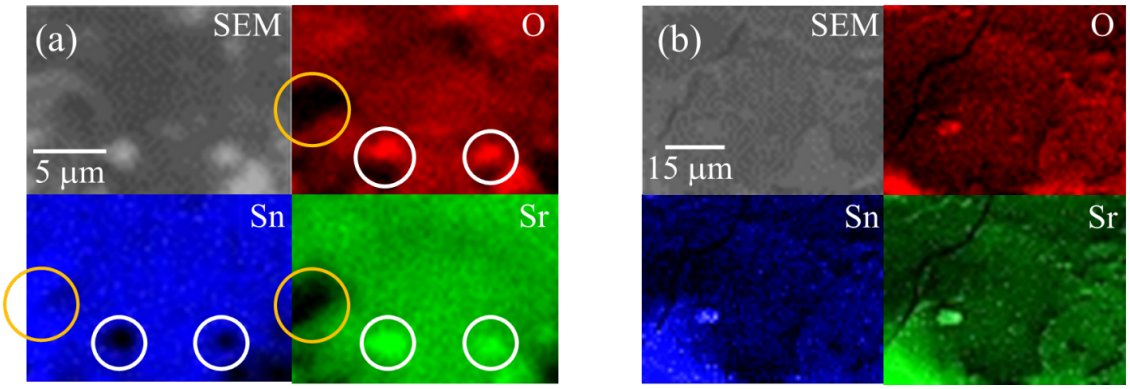

Figure 4.6: SEM and EDX images of $Sr_{2.5}SnO$ of Sample B-2 (a) and Sr_3SnO of Sample C (b) [2]. The air sensitive samples were exposed to air while vacuum was applied to the SEM/EDX chamber. Therefore, no flat surfaces and reliable quantitative analysis could be obtained. The grey image at the top left side of (a) and (b) is the SEM image and the other three are EDX images of the same area. The oxygen distribution is red, the tin is blue and the strontium is green. All three elements are distributed in a similar way in (a) and (b), indicating a strong dominance of the $Sr_{3-x}SnO$ phase. In (a) are some areas with different element ratios, indicating impurities. The white circles in (a) indicate a region containing only strontium and oxygen. The orange circles an area containing only tin.

A brief screening of reaction temperatures in the range of 800 °C to 1000 °C and reaction times from 1 h to 48 h was performed. No significant differences could be observed in the p-XRD and DC magnetization $M(T)$ data. We choose a maximum furnace temperature of 825 °C instead of 800 °C, as it guarantees the complete melting of the strontium (T_m = 777 °C) in our setup and a reaction time of 3 h seems most suitable.

The stoichiometric sample A-1 still shows a superconducting volume fraction of less than 1.5% at 2 K, indicating inhomogeneity of the strontium distribution with some deficient domains. To obtain more homogeneous materials with an improved crystallinity, Sr_3SnO was synthesized by heating the stoichiometric starting materials above T_m (Sr_3SnO) = 1080 °C and with an argon pressure of 22 kPa at room temperature. However, the molten Sr_3SnO reacted with the alumina

crucible, forming $Sr_x(Al_yO_z)$. Thus, tantalum crucibles were used instead. Initially, slow cooling through the melting point was attempted to grow single crystals. However, crystals with a sufficient size were not obtained and noticeable amounts of SrSn (T_m = 1140 °C) as well as SrO were present in all these samples. Therefore, a different method was used in which samples were water-quenched from 1200 °C and then sintered at 900 °C for 48 h to improve their crystallinity. Samples synthesized in this way with stoichiometric or slightly over stoichiometric strontium loadings did not show any superconductivity down to 0.15 K in alternating current (AC) susceptibility measurements, indicating a high homogeneity in the strontium distribution. A high energy p-XRD of such a sample C is shown in Fig. 4.5(a). It was free of any impurities and the peak shape indicates high crystallinity. Fig. 4.6(b) shows EDX images of the oxygen (red), tin (blue) and strontium (green) distribution. Unfortunately, as with sample B we did not succeed in protecting the samples from air during the whole procedure. Therefore, we could not obtain flat surfaces and reliable quantitative results for the element ratios. All three elements are distributed in the same way supporting the presence of a clean Sr_3SnO phase as indicated by the p-XRD data of Fig. 4.5(a).

Since quenching Sr_3SnO from above its melting point was successful for synthesizing stoichiometric samples with a homogeneous strontium distribution, we attempted the same method for the strontium deficient samples. However, we found that at temperatures above the melting point deficient $Sr_{3-x}SnO$ decomposes into Sr_xSn_y , SrO and stoichiometric Sr_3SnO. Hence, this procedure was not suitable for the synthesis of superconducting strontium deficient samples. Furthermore, this observation indicated that deficient $Sr_{3-x}SnO$ is meta-stable even under an inert atmosphere, making it challenging to synthesize. Another crucial aspect for the synthesis of superconducting $Sr_{3-x}SnO$ is the high purity of the strontium raw material, as discussed below.

Fig. 4.7 shows DC magnetization data $M(T)$ of stoichiometric Sr_3SnO (Sample B-1), of $Sr_{2.5}SnO$ with 99.9% purity of the strontium substrate (Sample B-2) and $Sr_{2.5}SnO$ with 99.99% purity of the strontium substrate (sample B-3). Despite the strontium purity, the synthesis method of B-2 and B-3 is identical and the p-XRD data showed no significant differences. The curve for the zero-field-cooling (ZFC) process of Sample B-2 shows a magnetic flux expulsion corresponding to an apparent superconducting volume fraction of 64% without demagnetization correction at 2 K with an onset of 4.8 K. The ZFC curve of Sample B-3 revealed a superconducting volume fraction of 105% with an onset of 5.2 K. Both superconducting volume fractions clearly indicate bulk superconductivity of the main $Sr_{2.5}SnO$ phase. A weak effect on the T_c and a significant dependency of the superconducting volume fraction on the strontium purity can be deduced. Remarkably, for $Sr_{2.5}SnO$ samples synthesized like B-2 and B-3, but with strontium of 99% purity 1 , no superconducting transition in the DC magnetization $M(T)$ down to 2 K can be observed. Such a high sensitivity towards nonmagnetic impurities is known for some unconventional superconductors such as Sr_2RuO_4 [106]. The field-cooling (FC) curves in Fig. 4.7 of the samples B-2 and B-3 are much less pronounced, as expected for a type-II superconductor due to flux pinning. In the ZFC curve of Sr_3SnO (Sample B-1) no sizeable diamagnetic transition is present down to 2 K. Furthermore, AC susceptibility measurements could not reveal a superconducting

transition down to 0.15 K. These results clearly indicate that only strontium deficient $Sr_{3-x}SnO$ is superconducting.

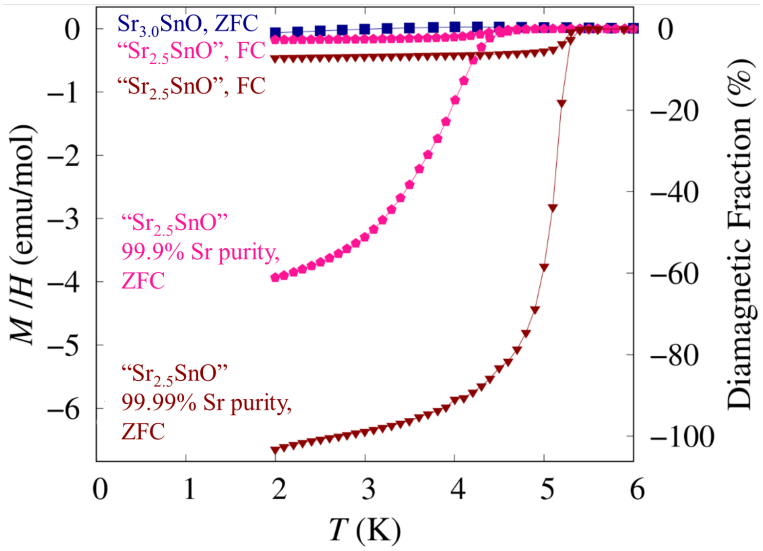

Figure 4.7: Magnetization under zero field cooling (ZFC) with an applied field of 2 mT of Sr_3SnO of Sample B-1 (blue square), and under ZFC as well as field cooling (FC) of $Sr_{2.5}SnO$ of Sample B-2 (pink pentagon) and Sample B-3 (brown triangles) [2]. The vertical scale on the right indicates the estimated diamagnetic volume fraction without demagnetization correction. Stoichiometric Sr_3SnO is not superconducting. The superconducting volume fraction of $Sr_{2.5}SnO$ increases significantly with increased purity of the strontium raw material.

Method A and 99.9% Sr were used in the synthesis of the first superconducting samples presented in the next chapter. For samples presented in Chapter 6, method B with 99.99% Sr were used to promote the appearance of superconductivity in $Sr_{3-x}SnO$. Furthermore, high energy XRD results are presented in Appendix A, which includes low and high temperature measurements of $Sr_{3-x}SnO$ samples. The low temperature measurements go down to 30 K. The high temperature measurements go up to 1,000 K, and were used to evaluate the volume coefficient of expansion for nearly stoichiometric $Sr_{3-x}SnO$. The decomposition of Sr_3SnO sample into Sr_2Sn, SrO, and an unidentified phase at around 700 K. The unidentified phase may contain some nitrogen, as the samples were sealed inside capillaries inside a nitrogen filled glovebox.

Chapter 5

Discovery of Antiperovskite Oxide Superconductivity

In this chapter, the initial results on early $Sr_{3-x}SnO$ samples showing superconductivity are presented first. This is followed by a report on the superconducting properties in three samples, where magnetization, resistivity, and Hall measurements are presented. The specific heat measurements were more challenging, and these results are discussed in a separate section to demonstrate the bulk nature of the superconductivity. Theoretical results demonstrating the Dirac point in the band structure, and the possible cooper pairing in the superconducting state of hole-doped Sr_3SnO are presented. Theoretical results in this chapter were performed by Prof. M. Sato, Dr. S. Kobayashi, and T. Fukumoto.

5.1 $Sr_{3-x}SnO$ Discovery Samples

The powder X-ray diffraction (p-XRD) of superconducting samples revealed cubic Sr_3SnO to be dominant, but with some splitting in the peaks (Fig. 5.1). The main phase has the lattice parameter a = 5.1222 Å and the minor phase a = 5.1450 Å. These values are compared to the reported value a = 5.12 Å for polycrystalline samples synthesized at 600–700°C (Ref. 4) and 5.1394 Å for single crystals synthesized at temperatures up to 1100°C (Ref. 6). Two cubic phases with a difference of 0.02 Å is perhaps the strongest conclusion of these initial samples, and the exact lattice parameter is determined more accurately in later samples (See Appendix A). Initially, we suspected that the phase splitting is likely due to different Sr-deficiencies in some parts of the sample, since Sr partially evaporates during the reaction. It is clarified in later samples (Presented in Chapters 4, Chapter 6, and Appendix A) that the peak splitting may originate from SrO impurity in forming in Sr-deficient environment. In addition, a very small amount of Sn and other impurity phases containing Sr are present (marked with asterisks in Fig. 5.1). These features in p-XRD are common in other batches. All the samples showing superconductivity had Sr deficiency, either caused by significant Sr evaporation during synthesis or by Sr-deficient starting composition (Details in Chapter 4). Since stoiciometric Sr_3SnO does not show superconductivity, we conclude that a deficiency in strontium leads to superconductivity in this compound.

The resistivity of Sr_3SnO exhibited a sharp drop with an onset of 4.9 K and zero resistivity below 4.5 K in zero field (Fig. 5.2a, batch C). Magnetic shielding of another sample from the same batch with an onset of 4.8 K is observed in the imaginary and real parts of the AC susceptibility χ''_{AC} and χ'_{AC} (Fig. 5.2b and c). The transition in the DC magnetization $M(T)$ obtained with zero-field-cooling processes is more pronounced than the curve for field-cooling process, and is typical for type-II superconductivity with flux pinning. A sizable magnetic-flux expulsion in M corresponding to the superconducting volume fraction of 32% at 2 K was observed for the same sample (Fig. 5.2d, Batch C). The $M(T)$ of another sample with the onset of 4.8 K exhibits a volume fraction of 62% at 2 K (Fig. 5.2d, Batch D). These results assure bulk superconductivity in Sr_3SnO. The field dependence of M reveals hysteretic behaviour again characteristic for a type-II superconductor (Fig. 5.6). After exposed to air overnight, the sample decomposes into $Sr(OH)_2$ and Sn metal as confirmed by p-XRD. Such sample exhibits a superconducting transition with T_c = 3.7 K as expected for pure Sn.

We note that the χ_{AC} curve obtained with adiabatic demagnetization cooling down to 0.15 K exhibits an additional transition at 0.8 K (Fig. 5.3b and c). Since the 0.8-K transition is reproducible in all superconducting batches that we investigated down to 0.15 K, it most likely originates from another superconducting phase of Sr_3SnO with different stoichiometry. The transition in the specific heat C_p is not as pronounced due to the inevitably large contribution of the phonon specific heat compared to the electronic contribution with the small Sommerfeld coefficient γ. Nevertheless, a tiny anomaly below 5.1 K is observed after subtraction of the phonon contribution. The expected specific-heat jump is about 1% of the total specific heat and is on the order of uncertainty in the present measurements.

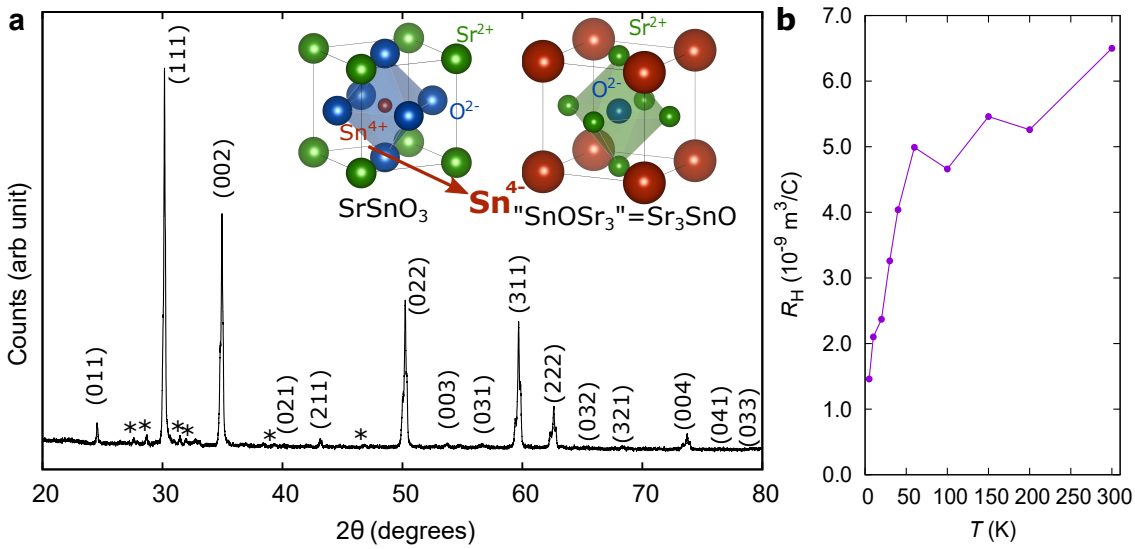

Figure 5.1: Structure and the sign of carriers in Sr_3SnO [1]. (a) Powder X-ray diffraction pattern of a superconductive Sr_3SnO batch-A sample. The spectrum was taken at room temperature using a lightly crushed sample with Kapton film and vacuum grease that protects it from air. Some impurity peaks can be seen and are marked with asterisks. The inset compares the perovskite $SrSnO_3$ and antiperovskite Sr_3SnO, emphasizing the change in oxidation states: Sr^{2+} corresponds to Sn^{4-}, Sn^{4+} to O^{2-}, and O^{2-} to Sr^{2+}. (b) Hall coefficient measured as a function of temperatures showing hole-like carriers for a batch-A sample.

The superconducting phase diagram is shown in Fig. 5.4. Here, T_c values were obtained from 10% and 50% resistivities shown in Fig. 5.2a. The upper critical field H_{c2} for $T \to 0$ is estimated to be $\mu_0 H_{c2}(0) = 0.44$ T, using the Wertheimer-Helfand-Hohenberg (WHH) relation $H_{c2}(0) = 0.72 T_c (dH_{c2}/dT)|_{T=T_c}$ [107]. This value corresponds to the Ginzburg-Landau (GL) coherence length $\xi_{GL}(0)$ of 27 nm.

The resistivity $R(T)$ shows metallic behaviour from room temperature with a relatively high residual resistivity ratio of ~16 and a small residual resistivity of 62 $\mu\Omega$cm for a polycrystalline sample (Fig. 5.5a). This contrasts with the semiconducting behaviour reported for Sr_3SnO thin films[66, 108]. The temperature dependence of the Hall coefficient R_H (Fig. 5.1b) indicates that holes are the dominant carriers in the whole temperature range. The estimated carrier density, if we assume a single hole band, is 4×10^{27} m^{-3} at 5 K and 1×10^{27} m^{-3} at 300 K.

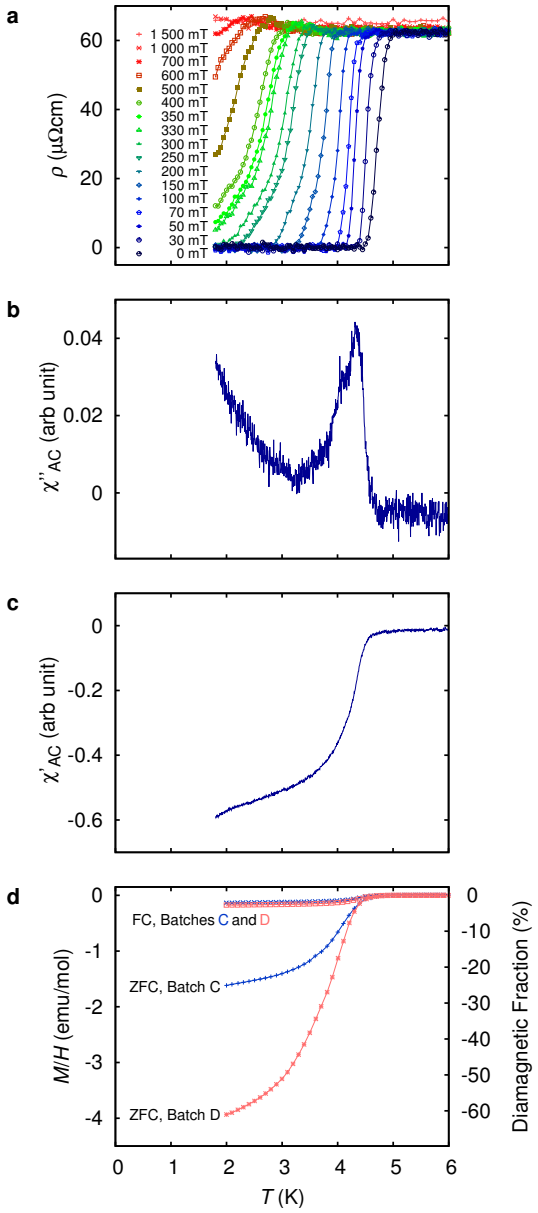

Figure 5.2: Superconducting transition of Sr_3SnO [1]. (a) Resistivity ρ of batch-C sample under zero and various magnetic fields. (b) and (c) Imaginary and real parts of AC susceptibility, χ''_{AC} and χ'_{AC}, under zero magnetic fields for a batch-C sample. (d) Magnetization under zero-field-cooling (ZFC) and field-cooling (FC) with an applied field of 0.5 mT of the same sample used in the χ_{AC} measurement (Batch C, blue crosses). Magnetization of a batch-D sample under ZFC and FC with an applied field of 1.0 mT is shown as well (red stars). The vertical scale on the right indicates the estimated diamagnetic volume fraction.

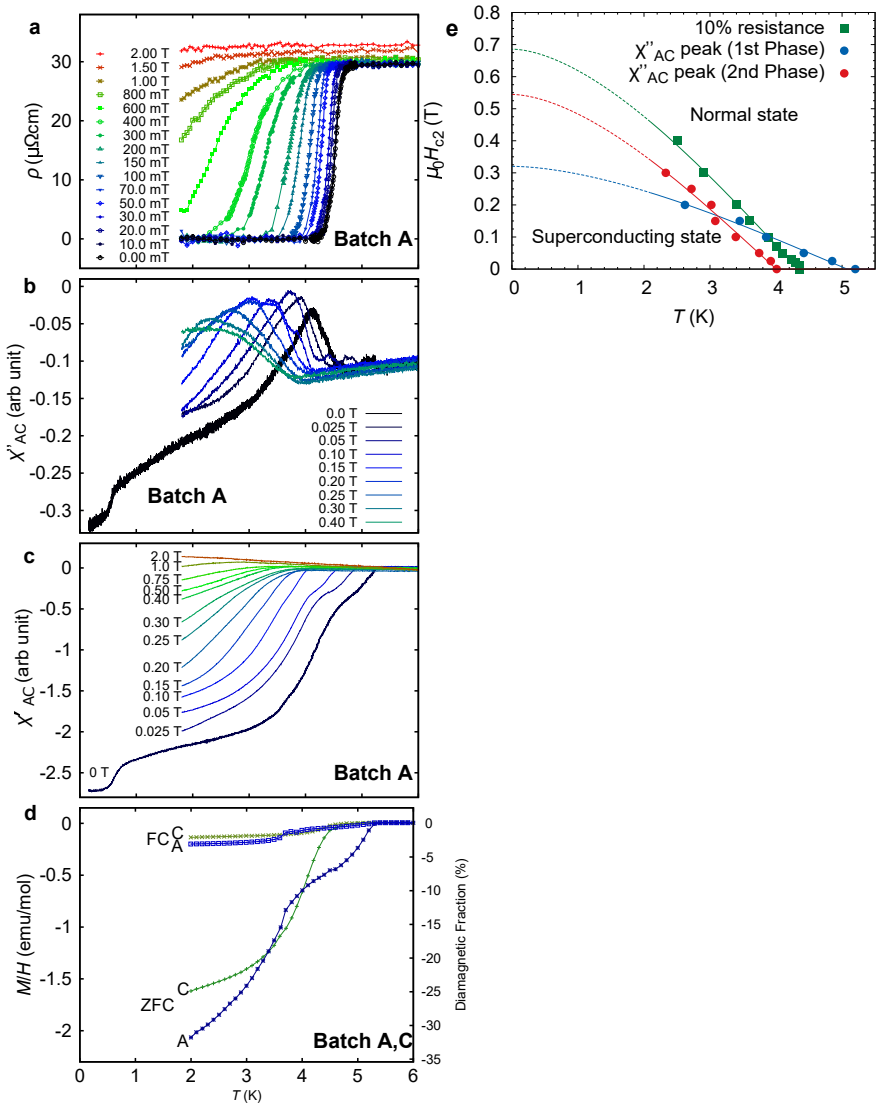

Figure 5.3: Superconducting properties of samples from different batches [1]. (a) Resistivity ρ under zero and various magnetic fields for batch A sample. (b) and (c) Imaginary and real parts of AC susceptibility χ'$_{AC}$ and χ"$_{AC}$ for batch A sample. (d) Magnetization under zero-field-cooling (ZFC) and field-cooling (FC) and with applied field of 0.5 mT for samples from batches A and C. The vertical scale on the right indicates the estimated diamagnetic volume fraction. The shoulder at around 3.7 K seen in the curve for the batch A is due to pure Sn contaminating the sample. (e) Field-temperature phase diagram of superconductivity in Sr_3SnO for batch-A sample. The upper critical field H_{c2} is extracted from both the 10% resistivity and the two transition features in AC susceptibility. The curves are results of fitting with the WHH relation [107].

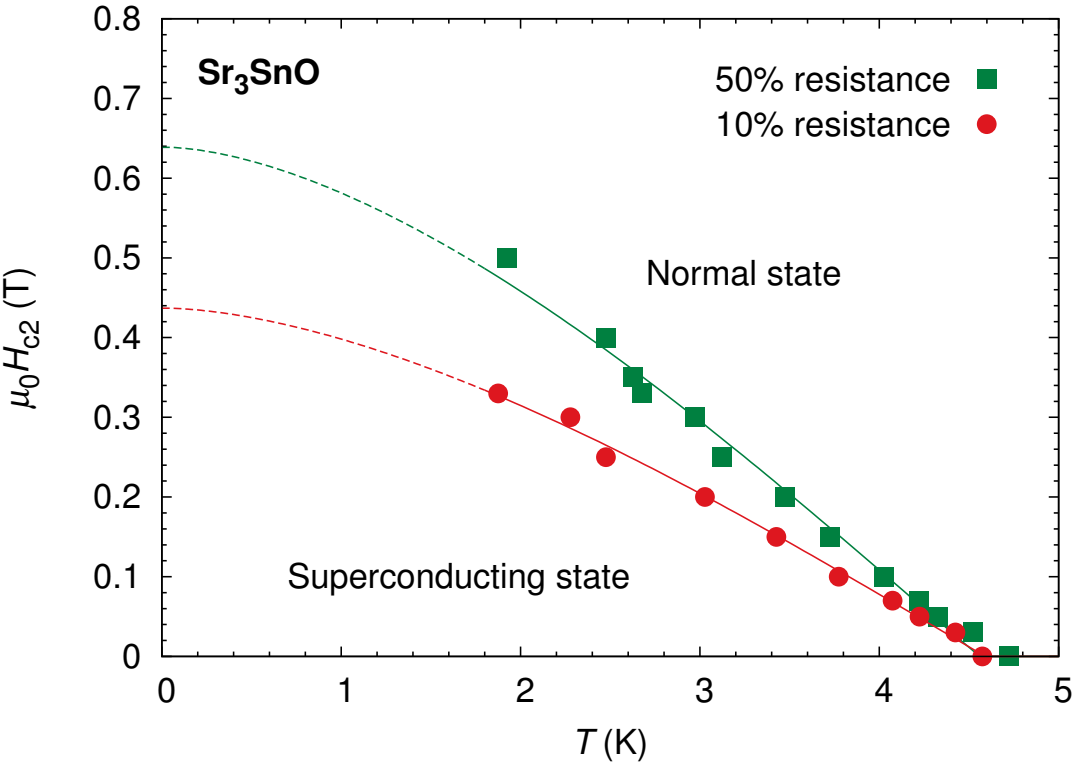

Figure 5.4: Field-temperature phase diagram of superconductivity in $Sr_{3-x}SnO$ [1]. The upper critical field H_{c2} is extracted from 10% and 50% resistivities for a batch-C sample. The curves are results of fitting with the WHH relation [107].

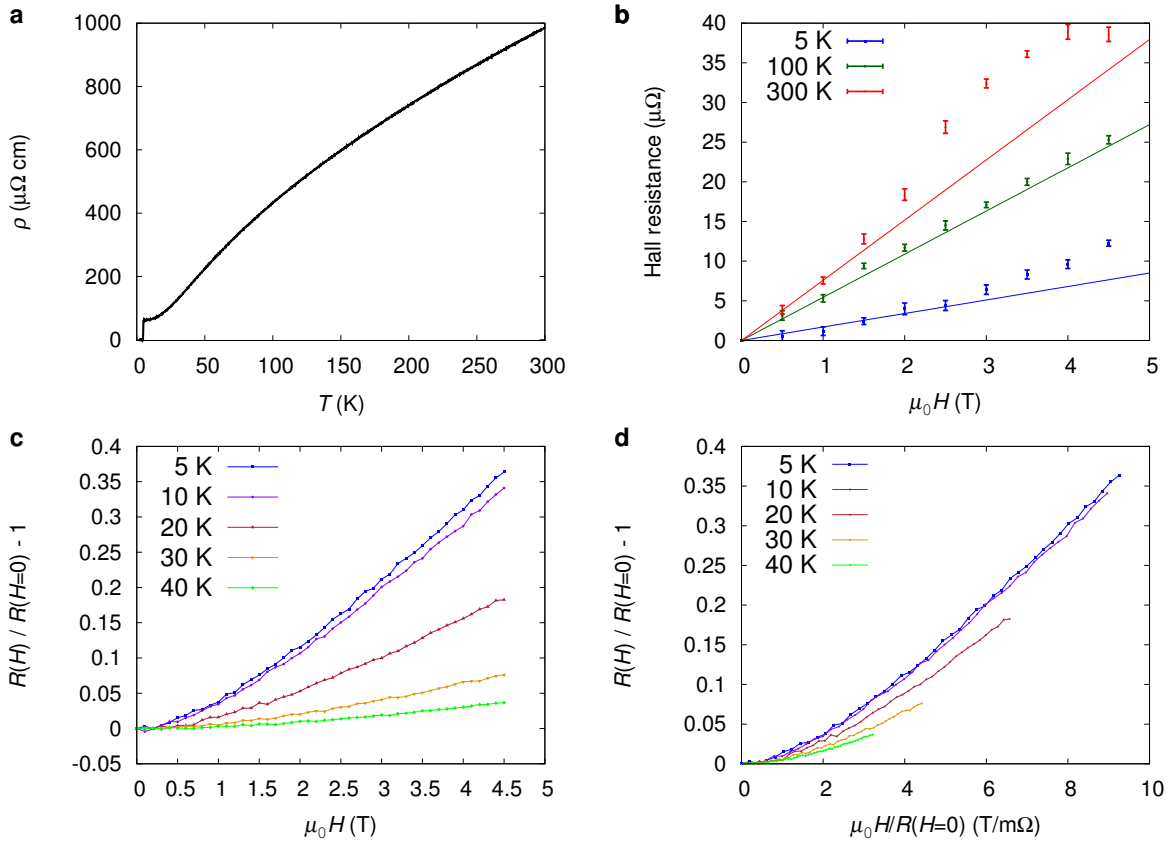

Figure 5.5: Transport properties of Sr_3SnO [1]. (a) Resistivity between 1.8 and 300 K for a batch-C sample. (b) Hall resistance as a function of applied field at various temperatures, indicating hole-like carriers for a batch-A sample. (c) Transverse magnetoresistance at various temperatures for a batch-A sample. (d) Kohler plot of normalized magnetoresistance vs. the magnetic field divided by the zero-field resistance for a batch-A sample.

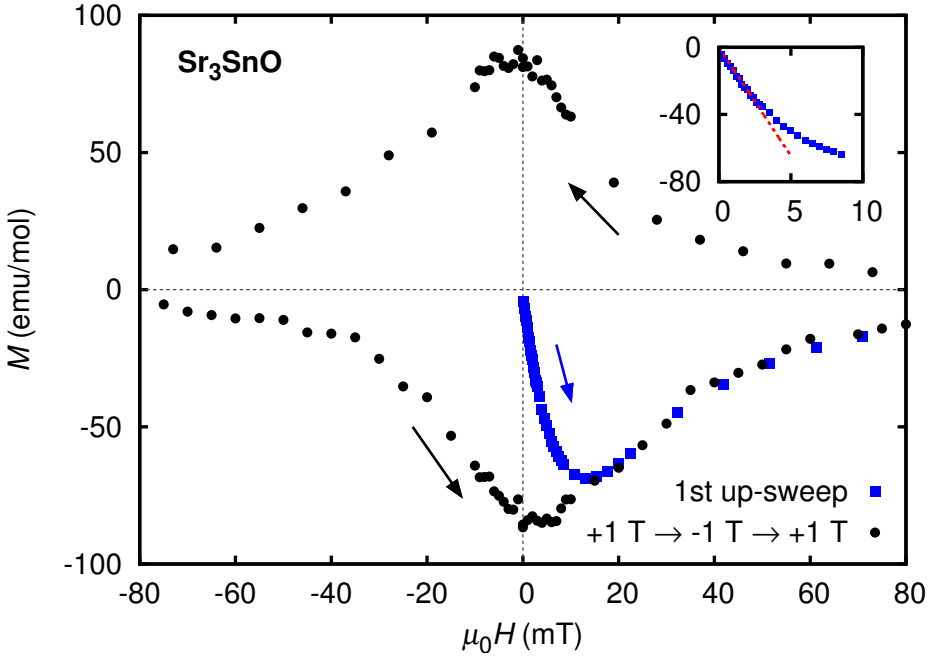

Figure 5.6: Magnetization curve of a Sr_3SnO sample at 2 K [1]. The curve was obtained for a batch-C sample in a field sweep loop: 0 T → 1 T → -1 T → 1 T. The inset shows a linear fitting to the initial up-sweep curve at a low field (red line). Deviation from linear behaviour was used to estimate H_{c1} and was approximately 2.4 mT.

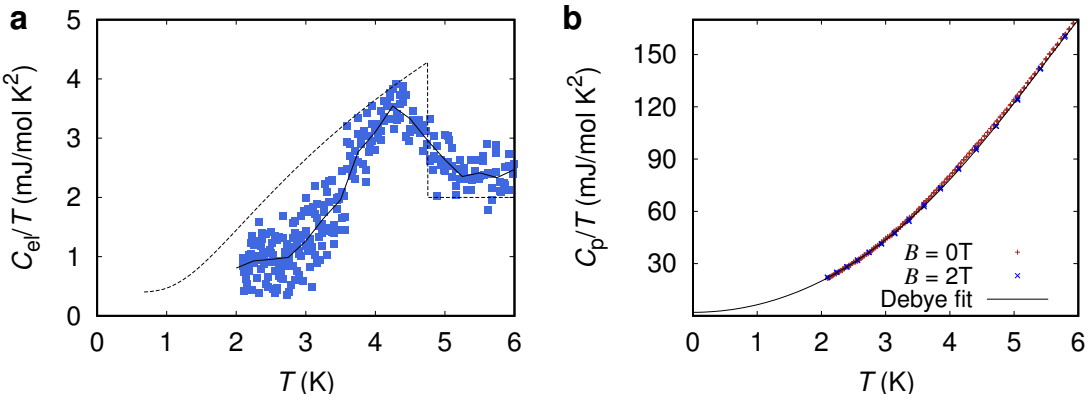

Figure 5.7: (a) Electronic part of specific heat, C_{el}, divided by temperature showing a peak-like feature near the T_c. The dotted curve is a fit based on BCS phonon prediction based on T_c= 5 K and γ = 2.0 mJ/molK^2. (b) The raw measured specific heat in the normal state (red +) and superconducting state (blue x) measured under a field of 0 and 2 T, respectively. The black curve is a polynomial fit to the normal state data. [Sample from Batch B.]

5.2 Specific Heat of $Sr_{3-x}SnO$

In this section, we present results of specific heat C_P measurement on the $Sr_{3-x}SnO$ samples synthesized under vacuum with uncontrolled evaporation. These are samples from Batch B and C from the discovery samples. The measurement on a sample from Batch B down to $\sim$ 2 K is presented in Fig. 5.7, where the normal state specific heat was measured under an applied field of 2 T, above H_{c2}. The C_P in the superconducting state was collected under 0 T. A sixth degree polynomial fit was applied to the normal state C_P, and this was subtracted from the C_P under 0 T to obtain the electronic specific heat C_{el}. The C_{el} divided by temperature is plotted in Fig. 5.7(a), where a small feature resembling a transition at T_c is observed. However, this feature is only visible under specific polynomial fittings to the normal state curve, therefore specific heat measurement should be repeated on new samples with a higher volume fraction.

C_P measurement on a sample from Batch C down to $\sim$ 0.40 K, using ^{3}He-option of PPMS, is presented in Fig. 5.8. Here, a more pronounced jump in C_P is observed at $\sim$ 0.9 K, reflecting that the low temperature superconductivity seen in χ_{AC} is dominant in this sample. In fact, this superconducting transition at $\sim$ 1 K is reproducible in all samples with $\sim$ 5 K transition and will be discussed in more detail in the next chapter.

The lack of specific heat may reflect the small γ value in these samples. If we calculate the expected specific heat jump based on γ and T_c, as shown in Fig. 5.9, we get a value that is on the order of the measurement error. The measurement at 5 K includes larger background contribution from phonons, which can mask this transition due to the lack of accurate fit to the background contribution. In comparison, the low phonon contribution at 1 K allows for a more

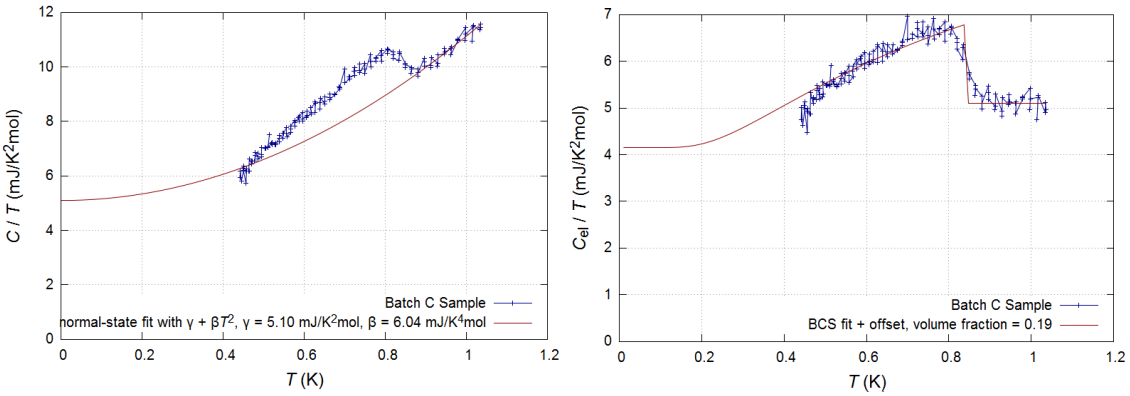

Figure 5.8: Specific heat at low temperature of $Sr_{3-x}SnO$ with transition at 0.9 K. [Sample from Batch C.]

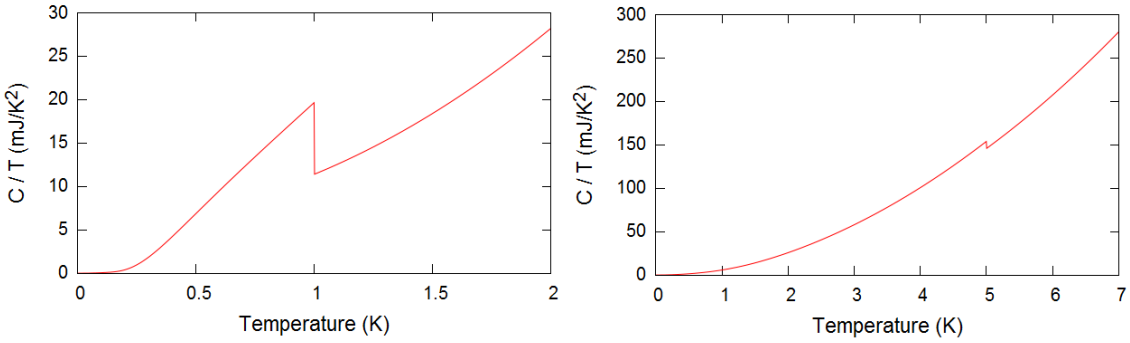

Figure 5.9: Simulation of expected jump in specific heat from a superconducting transition at 1.0 K (left) and 5.0 K (right).

accurate fit to the background data, and the jump in specific heat of the sample from Batch C was significant enough to be observed. Also, these initial samples had limited volume fraction, so this measurement should be repeated on one of the new samples with higher volume fraction.

5.3 Prediction of Topological Superconductivity

This theoretical work on Sr_3SnO is proposed by Prof. M. Sato, Dr. S. Kobayashi, and T. Fukumoto. The proposal of superconductivitiy originating from the topologically nontrivial part of the Fermi surface gives significance to the discovery of superconductivity.

Besides being the first superconductor among the antiperovskite oxides, Sr_3SnO has the prospect of topological superconductivity. As shown in Fig. 5.3a, the electronic states near the Fermi level for stoichiometric Sr_3SnO is influenced by the band inversion between Sr-4*d* and Sn-5*p* orbitals and the associated Dirac points near the Γ point [19]. Upon hole doping, a Fermi surface (FS) originating from these Dirac points merges into one FS around the Γ point. This FS with a deformed-octahedral shape has an unusual orbital texture, as shown in Fig. 5.3b. In addition, another hole pocket with orbital mixing centred at the Γ point appears inside (Fig. 5.12). We note that a first-principles band calculation utilizing the Heyd-Scuseria-Ernzerhof (HSE) screened Coulomb hybrid density functionals indicates yet another hole pocket around the R point [19]. In contrast, neither of our calculations based on the HSE functionals nor the Perdew-Burke-Ernzerhof generalized gradient approximation reproduces the R-point pocket (Fig. 5.11).

When Cooper pairs are formed in Sr_3SnO, their parity reflects the orbital texture of the underlying FS. Thus, electrons on the FS portion with strong orbital mixing favour forming odd-parity and correspondingly spin-triplet pairs. This odd-parity state belongs to the same representation as that of the fully gapped superfluid ^{3}He-B phase. As depicted in Fig. 5.3c, Cooper pairs can have either purely *p* or *d*-*p* mixed orbital character depending on the location on the outer and inner FSs. At present, we cannot deny the possibility that the hole FS around the R point, in the heavily hole-doped Sr_3SnO, is the main origin of the observed superconductivity. Even in that case, it is expected that pairing amplitude appears on the FS originating from the Dirac points and leads to unconventional properties related to topological superconductivity [117, 37]. Techniques used to observe Majorana zero modes on the surface of $In_{1-x}Sn_xTe$ [118], a leading candidate for 3D topological superconductors, may be adopted on Sr_3SnO to prove topological superconductivity.

From the orbital texture of the FS around the Γ point, a Cooper pair of Sr_3SnO may form between electrons in different orbitals, when the effective pairing interaction is dominated by an attractive inter-orbital interaction. The resultant inter-orbital Cooper pair realizes an odd parity superconducting state since Sn-5*p* and Sr-4*d* orbitals have opposite parity under inversion. Detailed theoretical analysis using the tight-binding model shows that the odd-parity pairing state is spin-triplet. The pairing symmetry is consistent with the Γ_1^- representation in the cubic point group, which is the same representation as the fully gapped ^{3}He-B phase. Thus, the odd-parity state is also fully gapped, although it has dips in the gap along the Γ-X direction due to suppres-

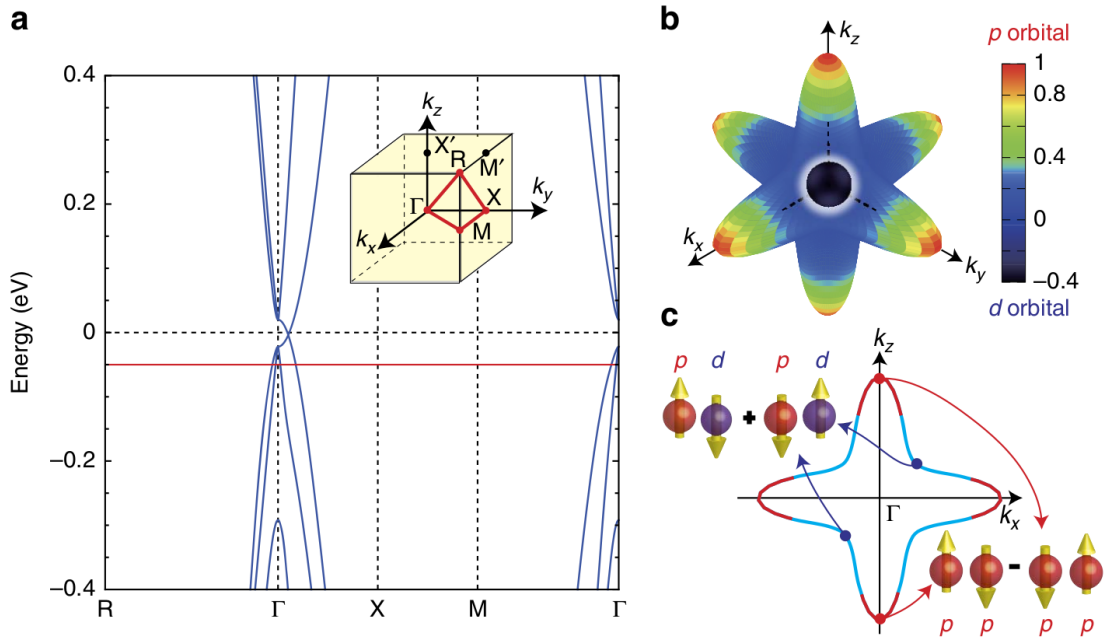

Figure 5.10: Orbital texture and possible Cooper pair symmetry of Sr_3SnO [1]. (a) Band structure of Sr_3SnO from tight-binding calculations with inverted orbital character and a Dirac point near the Γ point on each Γ-X line. Parameters are obtained by fitting to the first principles calculation [19]. Inset shows the cubic Brillouin zone. (b) Orbital texture of the FS around the Γ point, reflecting the band inversion. The colour represents mixing of Sn-5*p* and Sr-4*d* orbitals at each *k*-point on the FS, with red and black colours representing a pure *p* and dominant *d*, respectively. Orbital mixing on the outer FS is strongest along the Γ-M direction, while the *p* orbital dominates in the Γ-X direction. (c) Possible Cooper-pair symmetries. If superconducting symmetry is dictated by the pairing in the blue region on the FS, odd-parity spin-triplet pairing is favoured due to orbital mixing. In the case it is dictated by the red region, even-parity spin-singlet pairing is favoured.

sion of orbital mixing in this direction. From the transformation law under the mirror reflection and four-fold rotation, the mirror Chern numbers on the $k_i = 0$ planes ($i = x, y, z$) can be evaluated. It was found that the mirror Chern numbers are 2 (mod. 4), implying the topological crystalline superconductivity of Sr_3SnO.

Furthermore, if the hole FS exists around the R-point, as the first principles calculation suggests [19], the FS criterion of topological superconductivity [119, 120, 121] indicates that the odd-parity superconducting state is topological superconductivity. On the other hand, if the effective pairing interaction is dominated by an attractive intra-orbital interaction, an *s*-wave pairing symmetry may be realized. The orbital texture of the FS, however, is not compatible with an

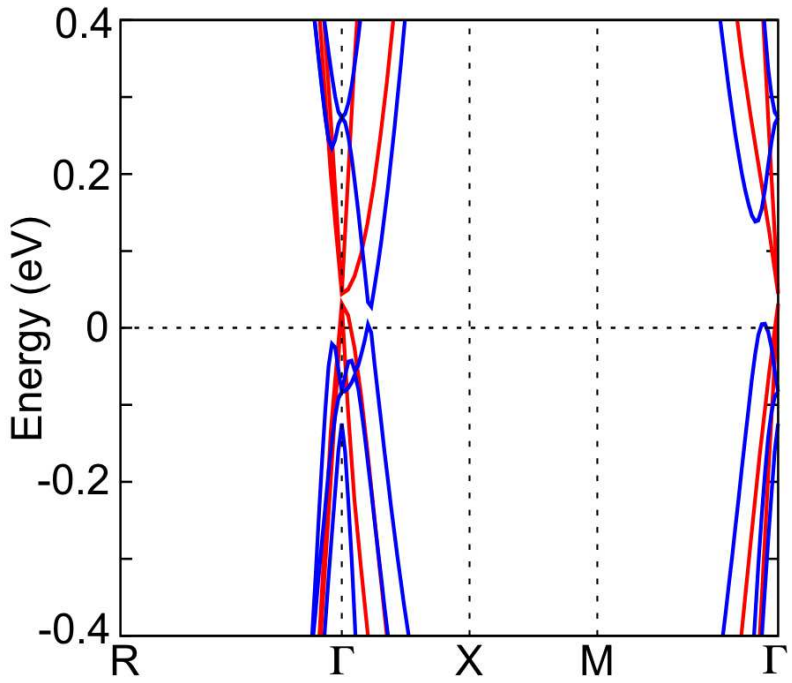

Figure 5.11: Band structures of Sr3SnO in the first principles calculation carried out with the WIEN2k package [78] (blue line) and the Vienna ab-initio simulation package (VASP) [109, 110, 111] (red line) [1]. Spin-orbit coupling is included in both calculations. For calculations with the WIEN2k package, the Perdew-Burke-Erzerhof generalized-gradient approximation [82] is used for the exchange-correlation function. The parameter (RK_{max}, G_{max})= (9.0, 14.0) [112] are chosen, and 20 x 20 x 20 momentum points in the irreducible Brillouin zone are used in the self-consistent cycle. The crystal parameters are taken from the experimental results [14]. The radii of the spherical atomic regions for Sr, Sn, O are chosen to be 2.33, 2.50, and 2.33 (a.u.), respectively. In the band structure obtained with the VASP, the Heyd-Scuseria-Ernzerhof (HSE) screened Coulomb hybrid density functionals [113] are employed to improve the underestimation of band gap. Besides, the projector augmented-wave potential [114, 115] and the 5 x 5 x 5 Monkhorst-Pack grid are used. The energy cutoff of the plane wave basis is 400 eV, and we performed structural relaxations with forces converged to less than 0.001 eV/Å. We note that for Sr_3SnO the band spectrum generated using the WIEN2k package is very different from that in ref. 5, where the HSE screened Coulomb hybrid density functionals were employed in the first principles calculation. First, details of the band structure near the Γ point are substantially different. Second, there is no hole FS around the R-point, whereas it is present in the result of ref.5. In contrast, the band spectrum generated using the VASP with the HSE method almost reproduces the band spectrum in ref. 5 near the Γ point, despite that there is no hole FS around the R-point again. Such method-dependence was discussed before by Vidal *et al.* [116], which concludes that the HSE method is more reliable. Thus we adopt the HSE result to parameterize our tight-binding band structure near the Γ point to obtain the orbital texture (Fig. 5.3 and Fig. 5.12).

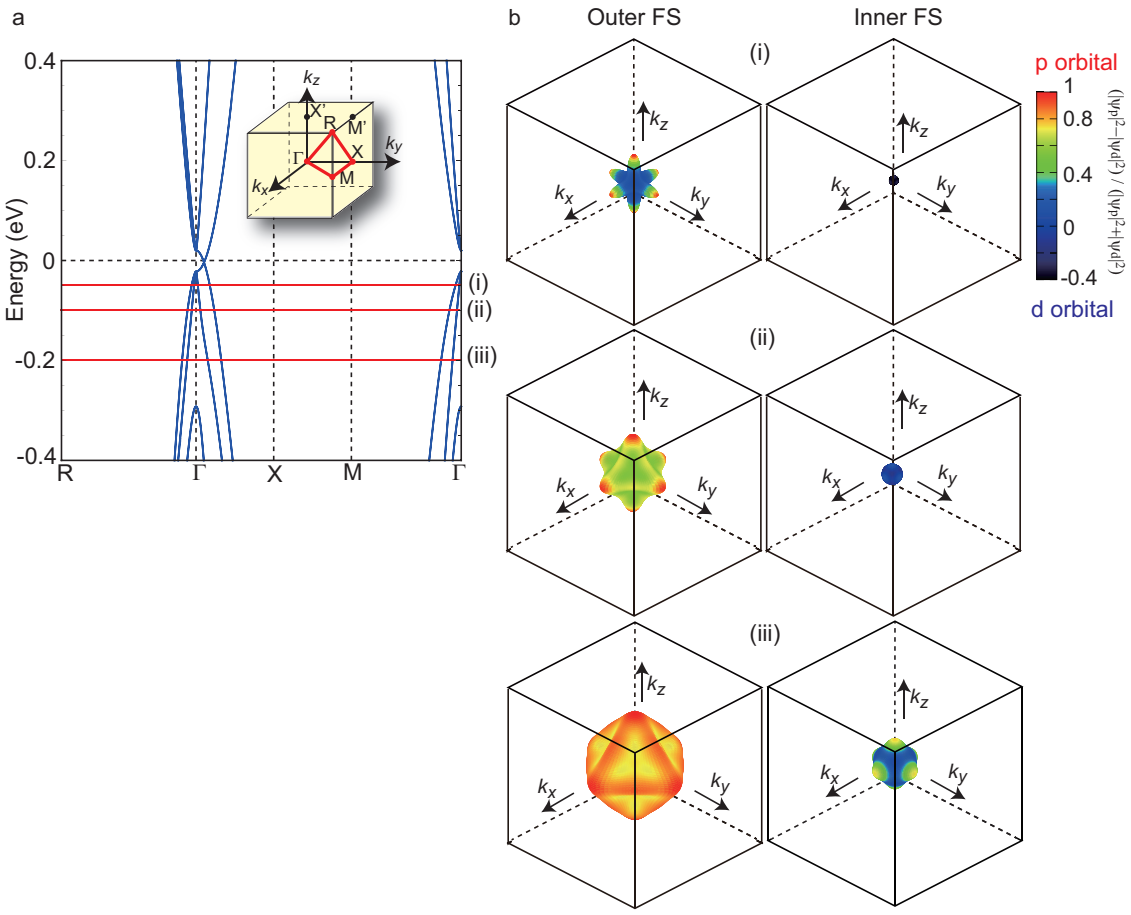

Figure 5.12: Fermi surface evolution and orbital texture from the tight-binding calculation [1]. (a) Tight-binding band structure with the red lines indicating the Fermi levels at (i) -0.05 eV, (ii) -0.1 eV, and (iii) -0.2 eV. (b) Orbital texture on the outer and inner FSs around the Γ point with the Fermi levels for (i), (ii), and (iii). The orbital mixing becomes stronger near the Dirac point.

isotropic *s*-wave pairing state. The superconducting gap would have dips along the Γ-M direction. The mismatch between orbital texture and pairing symmetry suppresses the critical temperature of the *s*-wave pairing state, causing a competition with the odd-parity pairing state. We note that a similar mismatch occurs in Cd_3As_2, where an odd-parity solution of the gap equation has the critical temperature comparable to that of the ordinary *s*-wave pairing state [122].

In this section, we report evidence for bulk superconductivity in Sr_3SnO at an onset of approximately 5 K, marking the first superconductivity among antiperovskite oxides. Mirroring the rich variety of properties in perovskite oxides, this work opens a door to superconductor as well as other interesting phenomena in antiperovskite oxides with unusual metallic anions.

Chapter 6

Deficiency Dependence of Properties

In this chapter, $Sr_{3-x}SnO$ samples synthesized with various deficiencies in Sr, x, are presented. The evolution of superconductivity in these samples with an increase in deficiency is clarified, and the strongest superconductivity signal is found in samples synthesized with the nominal composition ''$Sr_{2.5}SnO$". The Mössbauer spectra results for stoichiometric and deficient $Sr_{3-x}SnO$ samples are presented, and the isomer shift of the main peak suggests a Sn^{4-} state in $x = 0.0, 0.4, \& \ 0.5$ samples. The Mössbauer measurement was performed by S. Kitao.

6.1 p-XRD, EDX, and Mössbauer Spectra of $Sr_{3-x}SnO$

In the initial bulk superconducting $Sr_{3-x}SnO$ samples, it was proposed that hole doping due to Sr deficiency was necessary for the appearance of superconductivity. However, quantitative analysis of the deficiency was difficult due to the uncontrolled evaporation of Sr during the synthesis. After improving the synthesis, as shown in Chap. 4, we were able to suppress the evaporation with the addition of 0.3 atm of argon at room temperature. With this method, we produced a large number of $Sr_{3-x}SnO$ samples with varying x and examined their superconducting properties using DC magnetization and AC susceptibility χ_{AC} measurements. Superconducting samples with the highest volume fraction, of around 100%, were found in the vicinity of $x = 0.5$. Surprisingly, we observed two superconducting transitions for all investigated superconducting samples, one at 5 K and the other at 1 K, presented Sec. 6.2. In this section, the p-XRD, EDX, and Mössbauer spectra of some $Sr_{3-x}SnO$ samples are presented.

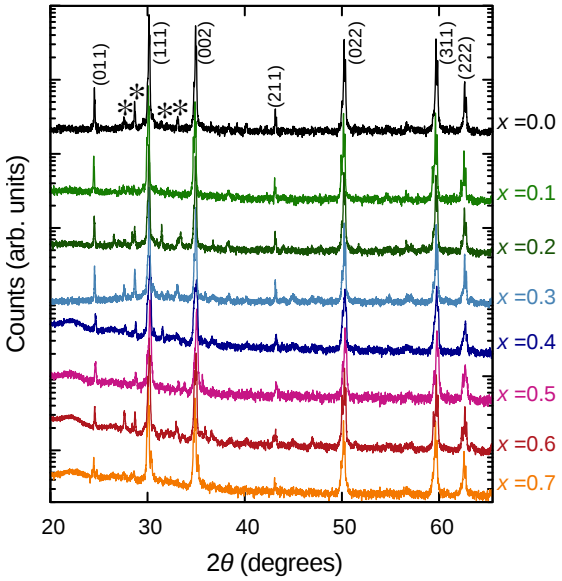

Figure 6.1: Powder XRD pattern of $Sr_{3-x}SnO$ with various nominal values of x plotted on a log scale. Minor impurity peaks from SrO phase are seen on the left of (111) and (002) peaks of the main phase. Additional weak impurities can be seen between the (011), (111), and (002) peaks.

In Fig. 6.1, we present the p-XRD patterns of $Sr_{3-x}SnO$ samples with the nominal x values in the range of 0.0 to 0.7. For $0.0 \leq x \leq 0.6$, the dominant phase is $Sr_{3-x}SnO$, with some amount of SrO (cubic, $a = 5.16$ Å). Indeed, shoulder peaks characteristic of SrO are seen on the left side of some of the main peaks, but this phase remains a minor one for $x \leq 0.6$. For $x > 0.6$, however, the peaks of SrO become rather substantial and peaks of additional unidentified impurity phases appear. Some of these minor impurity peaks, marked with asterisks in Fig. 6.1, likely originate from Sr-Sn alloys. From the p-XRD pattern, we evaluate the lattice constant a for each sample. Interestingly, a is found to be almost x independent, with $a = 5.139 \pm 0.002$ Å for all x. We comment here that, in order to avoid contact with air before physical property measurements, p-XRD is typically measured on a piece not used for other measurements. Neverless, we performed p-XRD on a piece after confirming its high superconducting volume fraction by magnetization measurements, as shown in Fig. 6.2. The obtained p-RD pattern in Fig. 6.3 demonstrates that the observed superconductivity is certainly not attributed to other known superconductors containing Sr and Sn: e.g. β-Sn ($T_c = 3.7$ K) [123], $SrSn_3$ ($T_c = 5.4$ K) [61], and $SrSn_4$ ($T_c = 4.8$ K) [62, 63]. We also performed EDX measurements on some samples as represented in Fig. 6.4. Regions with Sr/Sn ratio close to $3 - x$ are observed. In addition, some Sr-rich and Sn-rich regions exist, which likely originate from the SrO phase and pure Sn or Sr-Sn alloys, respectively.

We present the magnetization results for a superconducting sample with nominal $x = 0.5$ showing the volume fraction close to 100%, as presented in Fig. 6.2. We used a commercial superconducting quantum interference device (SQUID) magnetometer (Quantum Design, MPMS). In order to allow subsequent p-XRD measurement, this piece was placed in a plastic capsule sealed with Kapton tape, all within an argon glovebox, to protect it from decomposing in air. This a more challenging way of sealing the sample than covering the sample with grease, which we typically used. The sample was later removed from the plastic capsule, and crushed into powder for XRD measurement, collected using a commercial diffractometer (Bruker AXS, D8 Advance) utilizing the CuK_α radiation. The measured p-XRD pattern for this piece is presented in Fig. 6.3, together with the expected diffraction patterns of Sr_3SnO, insulating SrO, and other superconducting materials reported in the Sr-Sn-O systems: β-Sn, $SrSn_4$, and $SrSn_3$.

The p-XRD pattern we measure matches well with that expected for Sr_3SnO and small shoulder peaks characteristic of SrO can be seen. The simulated p-XRD patterns of the other compounds do not match the measured pattern. From this comparison, we can conclude that the superconductivity with the volume fraction closet to 100% most likely originates from $Sr_{3-x}SnO$.

Representative EDX results for $Sr_{3-x}SnO$ samples with $x = 0.5$ are presented in Fig. 6.4. We should comment that the surface of these samples is likely oxidized and decomposed during transfer from our glovebox to the EDX measurement chamber (a scanning electron microscope (Keyence, VE-9800) equipped with an X-ray detector (AMETEK, Element K)). This surface oxidization results in the high percentage of oxygen seen in EDX results, as seen in the panels (a), (f), and (k). However, we expect that the Sr/Sn ratio should not be drastically affected by this short exposure to air. This ratio is mapped in the panels (d), (i), and (n), where the white regions correspond to Sr/Sn = 2.5, expected for the $Sr_{3-x}SnO$ phase from the nominal value of $x = 0.5$

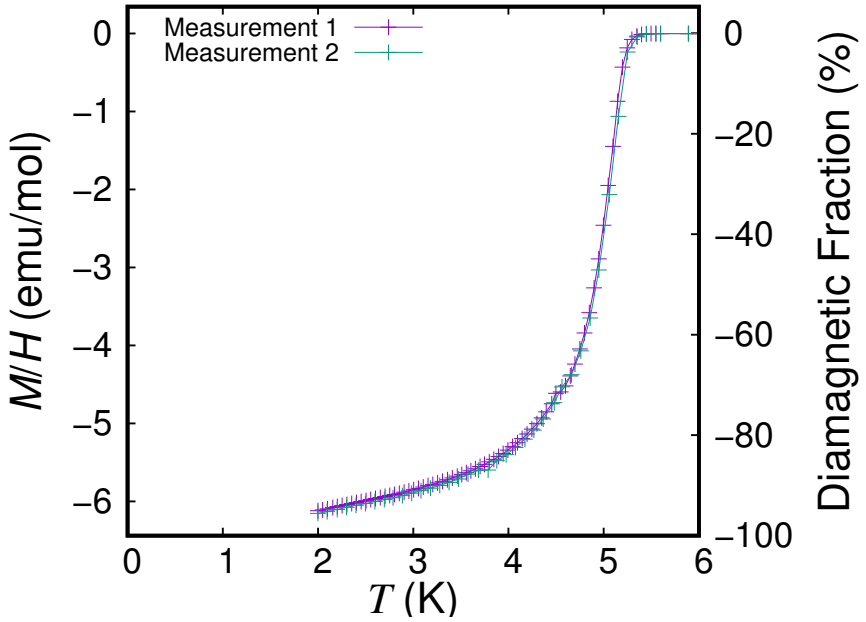

Figure 6.2: DC magnetization measured at 10 Oe as a function of temperature of a $Sr_{2.5}SnO$ sample (Batch No. AP164). Degaussing was performed between the two measurements, both reproducibly showing strong superconducting 5-K phase, close to 100% volume fraction. Demagnetization correction was not done. After these measurements, the remnant field was checked using a reference superconductor (Pb, 99.9999% purity) and found to be below 1 Oe.

in the sample. In these panels, we can also see some Sr-rich regions, likely originating from SrO phase in the sample. In the panel (n), we can see Sn-rich regions reflecting either an impurity formed during synthesis or decomposition on the surface during transfer to the chamber. The bottom panels show histograms of the distribution of the Sr/Sn ratio. In (e) and (j), the Sr/Sn ratio distribution in the investigated regions is centered around 2.5, in agreement with the $Sr_{2.5}SnO$ phase in these samples. In (o) the distribution is broader, but regions with ratio close to 2.5 are still visible.

In Fig. 6.5, we present Mössbauer spectra for $Sr_{3-x}SnO$ with $x = 0.0$, 0.4, and 0.5. The isomer shift, the peak position of the absorption spectra, represents the difference in the energies of the ground and excited states of the Sn nucleus with respect to those of the source material. It is closely related to the electronic density at the nucleus position. Thus, the isomer shift is most sensitive to the number of *s* electrons, whereas *p* and *d* electrons lead to opposite weaker shift compared to *s* electrons via the screening effect. In all samples, the isomer shift of the main peak is about +1.83 mm/s. This shift does not match those expected for ordinary valences Sn^{4+}, Sn^{2+}, and Sn^{0}; but is equal to that reported for Mg_2Sn [124], where the Sn^{4-} valence is expected

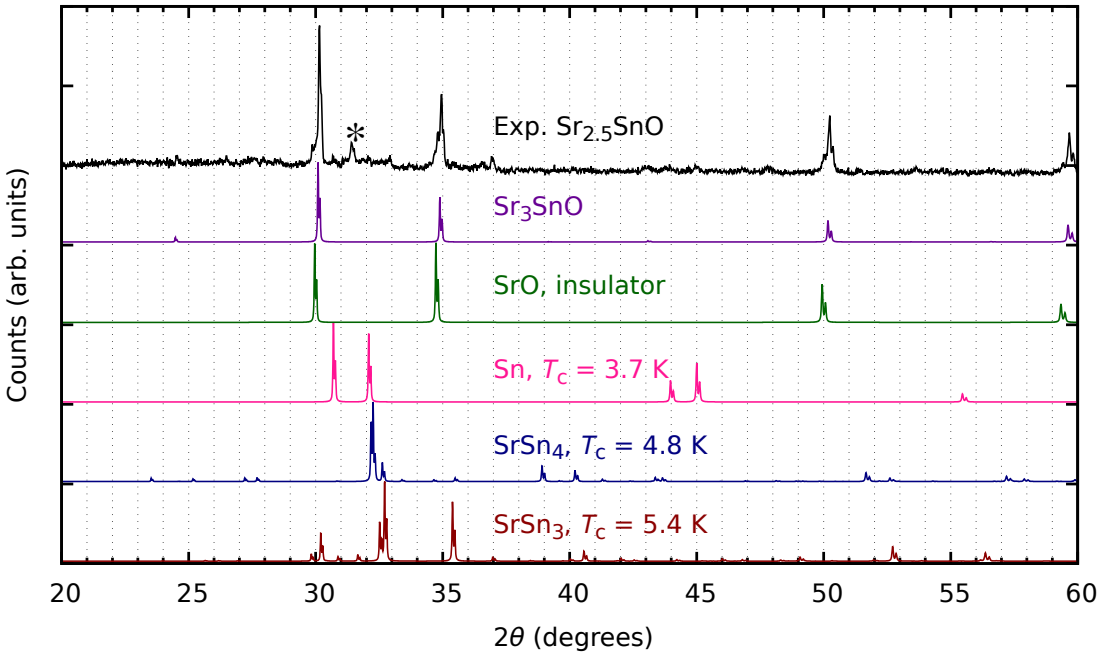

Figure 6.3: Powder XRD of the same superconductive $Sr_{2.5}SnO$ piece whose magnetization is shown in Fig. 6.2, compared with expected diffraction patterns of Sr_3SnO, SrO, β-Sn, $SrSn_3$, and $SrSn_4$ [16]. β-Sn, $SrSn_3$, and $SrSn_4$ are also superconducting with T_c's indicated in the figure [123, 61, 62, 63]. The peak marked with asterisk does not decrease in intensity even after $Sr_{2.5}SnO$ decomposes in air.

based on the charge balance consideration $(Mg^{2+})_2Sn^{4-}$. In deficient samples, a satellite peak is observed at +2.59 mm/s, which may originate from β-Sn or from Sn sites in $Sr_{3-x}SnO$ next to the Sr deficiency. Our result provides the first microscopic support for the presence of the unusual Sn^{4-} ions with fully occupied Sn-5p orbitals. Temperature dependence of Mössbauer spectra in $Sr_{3-x}SnO$ samples ($x = 0.0, 0.5$) are shown in Appendix B. Also, estimates of the Mössbauer isomer shift using WIEN2k calculations, and literature values of various Sn-containing compounds are presented in Appendix C.

6.2 M/H and χ_{AC} of $Sr_{3-x}SnO$

Here, we present the various magnetic properties of $Sr_{3-x}SnO$ samples down to 0.1 K, and highlight the evolution of these properties with varying x. Figure 6.6(a) shows the temperature dependence of DC magnetization down to 1.8 K of $Sr_{3-x}SnO$ with various x. Superconductivity appears

for some samples with $0.35 < x < 0.70$. However, T_c is observed to be commonly 5 K for such superconductive samples, and volume fraction at 1.8 K seems to vary even for samples prepared with the same nominal composition. These facts suggest some inhomogeniety in the samples. The volume fraction close to 100% in zero-field-cooling (ZFC) measurements observed in some samples provides strong evidence for the bulk superconductivity of $Sr_{3-x}SnO$, considering the sample purity demonstrated by p-XRD. In Figs. 3(b) and (c), the real and imaginary parts of the χ_{AC} signal normalized by the sample mass are presented for representative samples. Interestingly, a second superconducting transition appears at ~1 K for all superconducting samples. The magnitude of the superconducting signals of these two superconducting phases varies depending on the sample. In the examples shown in Figs. 3(b) and (c), the $x = 0.52$ sample exhibits a stronger transition at 5 K, while in the $x = 0.43$ sample the 5-K and 1-K transitions have similar magnitude. The splitting in the peak of the imaginary part at the 5-K transition is often seen, as previously reported [1].

The x dependence of superconducting properties, namely T_c and volume fractions, evaluated based on the DC magnetization and χ_{AC} measurements are summarized in Fig. 6.7. Superconductivity at about 5 K and 1 K appears in the range $0.35 \leq x \leq 0.65$, with almost no change of T_c, as shown in Fig 6.7.(a). This fact implies that a specific composition exhibits both superconducting phases. The volume fraction of the 5-K phase superconductivity calculated using the DC magnetization of the ZFC process at 10 Oe and 1.8 K are presented in Fig. 6.7(b). The volume fraction is strongly sample-dependent even among samples with similar x values. Nevertheless, there is a tendency that high volume fraction samples are more likely to be found around $x \sim 0.5$. To clarify this tendency more quantitatively, we evaluate the mass-weighted average of the volume fraction $\bar{v}$ of the range $x_0 - 0.025 < x < x_0 + 0.025$ as $\bar{v}_{x_0} = \sum_i m_i v_i / \sum_i m_i$, where m_i and v_i are the mass and volume fraction of the i-th sample and summation over i is taken for samples whose x value is in the range mentioned above. The results are presented in Fig. 4(c). Here, a dome-like shape appears for the volume fraction centered at $x \approx 0.55$; hinting at a specific phase favorable for superconductivity. The volume fractions of the 5-K and 1-K phases evaluated using χ_{AC} data normalized by the sample mass are summarized in Fig. 6.7(d). Here, the changes in the signal from 6 K to 2 K and from 2 K to 0.1 K are chosen to represent the volume fractions of the 5-K and 1-K phases, respectively. Some samples are dominated by the 1-K phase, while others have a stronger contribution from the 5-K phase. Nevertheless, we again observe a tendency that high volume fraction samples are found near $x \sim 0.5$. We comment here that the volume fraction presented in Fig. 6.7(b) may be an underestimate due to dominance of the 1-K phase in some of these samples, such as the $x = 0.45$ sample presented in Fig. 6.6(b).

The results presented in Fig. 6.7 suggest that there are two distinct superconducting phases. Since each T_c varies little, each superconducting phase corresponds to a specific composition of $Sr_{3-x}SnO$. Comparison between Figs. 6.7(c) and (d) implies that the x value for the 5-K phase is slightly higher than that for the 1-K phase. It may also happen that these two phases differ in the oxygen stoichiometry. Concurrency of the two superconducting phases may result from an intrinsic phase separation into these two phases. Carrier doping by methods other than deficiency,

such as substitution of Sr with K or Na, may provide hints toward clarifying this issue.

6.3 Band Structure of $Sr_{3-x}SnO$, where $x = 0.5$

In summary, we have reported comprehensive bulk and microscopic investigations of $Sr_{3-x}SnO$ samples with x varying from 0.0 to 0.7. We provided evidence for the unusual Sn^{4-} state with the filled $5p$ orbital in stoichiometric and deficient $Sr_{3-x}SnO$. We have demonstrated that superconductivity appears for samples with deficiency $0.35 < x < 0.70$. All superconducting samples exhibit two superconducting transitions, at about 5 K and 1 K. The present findings, clarifying the composition necessary for the appearance of superconductivity in $Sr_{3-x}SnO$, serve as important bases toward investigation of the proposed topological superconductivity in this system [1]. Also, we demonstrated that for $Sr_{3-x}SnO$, with $x = 0.5$, the band Dirac dispersion is preserved in the band structure, but appears 1 eV above the Fermi level, as shown in Fig. 6.10. These band calculations are based on ''$Sr_{2.5}SnO$" superlattice structures shown in Fig. 6.8. These superlattices result in simple tetragonal and body-centered tetragonal structures, and we compared p-XRD patterns of these structures with the experimental high-energy XRD data at 30 K, shown in Fig. 6.9. There is no clear evidence of either one of these superlattices in the experimental results, and further investigation is necessary to conclude any ordering of deficiencies in $Sr_{3-x}SnO$. Topological superconductivity in Sr_3SnO, described in Chap. 5, is may exist in deficient $Sr_{3-x}SnO$. Producing superconducting $Sr_{3-x}SnO$ single crystals or thin-films can be a next important step to the goal.

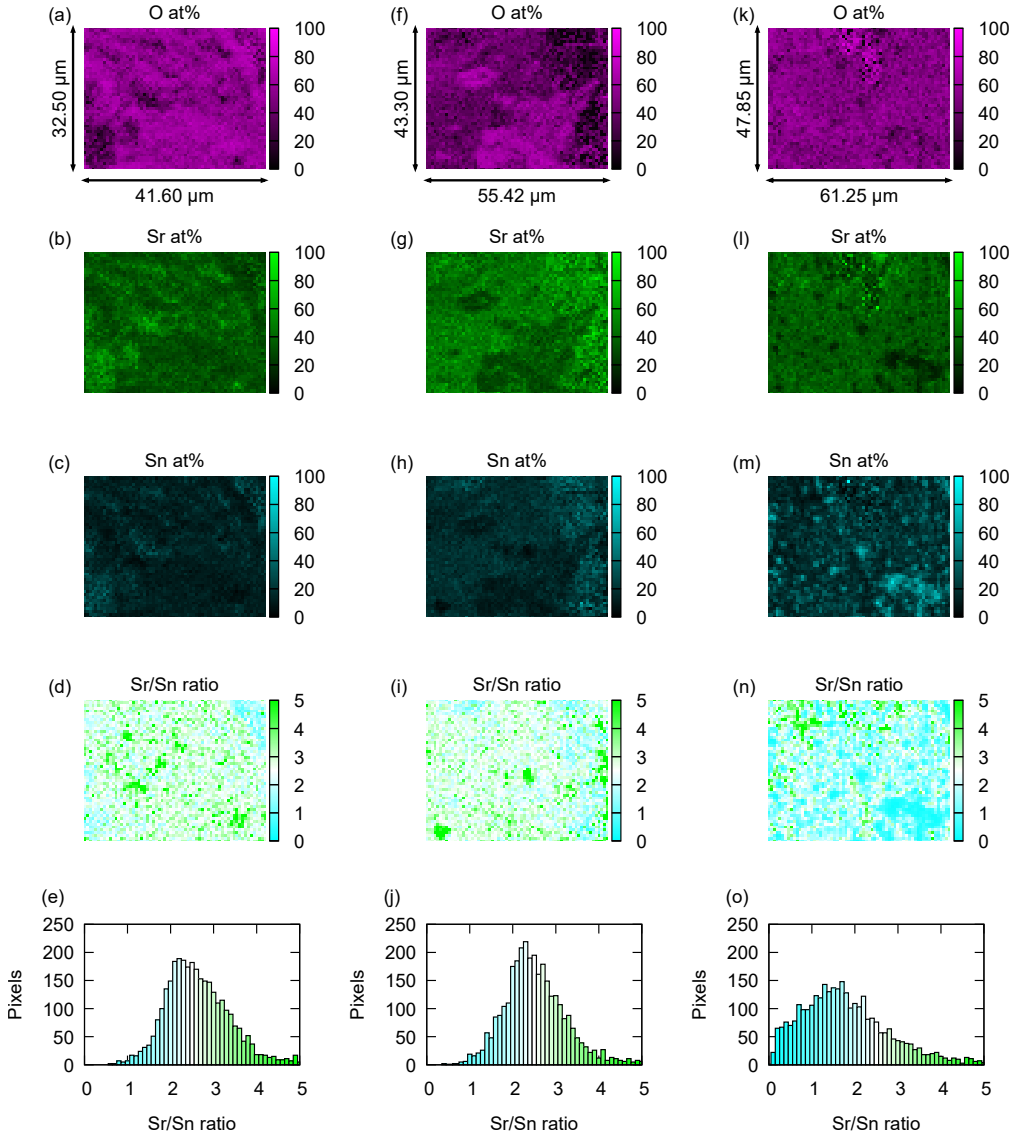

Figure 6.4: EDX results of various $Sr_{3-x}SnO$ samples with the nominal $x = 0.5$. The panels (a)–(c) respectively show mappings of the contents of O, Sr, and Sn atoms in at% value of a typical sample surface (Batch No. AP165). The ratio between Sr and Sn contents is mapped in the panel (d), and the distribution of this ratio is shown in the histogram in the panel (e). In (d) and (e), the white color correspond to the ratio Sr/Sn = 2.5, expected for the nominal x value, while the green and blue colors correspond to more Sr-rich and Sn-rich ratios, respectively. The panels (f)–(j) present similar information but for a different region of the same sample (Batch No. AP165), and the panels (k)–(o) for another sample (Batch No. AP210).

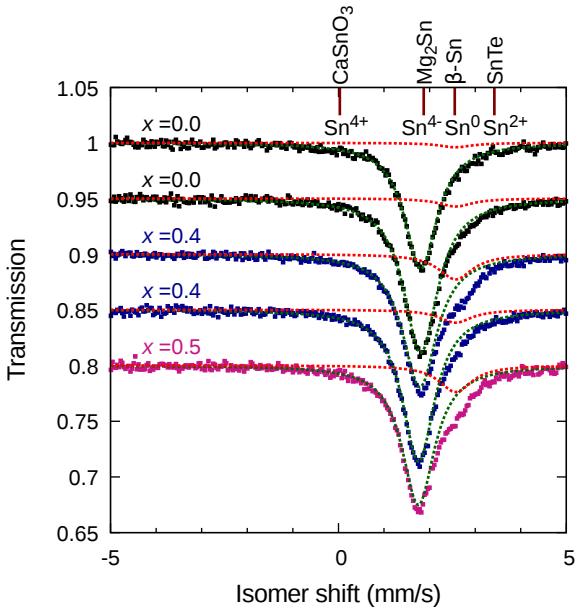

Figure 6.5: Mössbauer spectra of $Sr_{3-x}SnO$ with different values of x. The origin of the isomer shift is defined with respect to that of $BaSnO_3$, and isomer shifts of some reference materials with different Sn valencies are indicated. The dotted curves indicate Lorentzian fits for the main (green) and satellite (red) peaks.

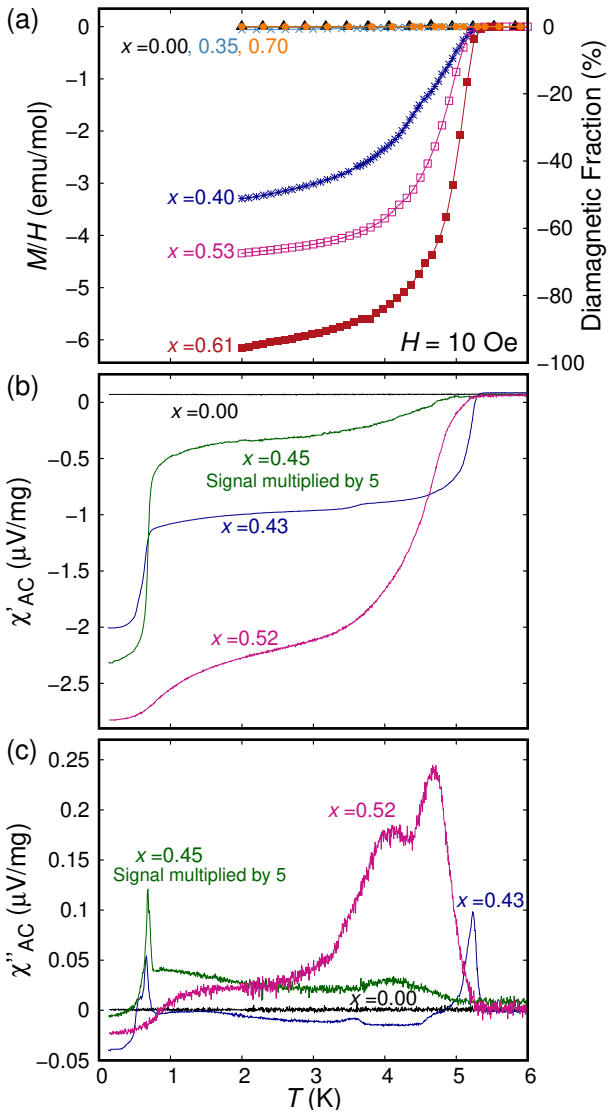

Figure 6.6: (a) DC magnetization as a function of temperature of $Sr_{3-x}SnO$ samples with various values of x. Superconductivity appears for $x > 0.35$ and becomes much weaker for $x \geq 0.7$. (b) Real and (c) imaginary parts of AC susceptibility, χ_{AC}, normalized by mass as a function of temperature. Two superconducting transitions appear for superconducting samples, at about 5 K and 1 K.

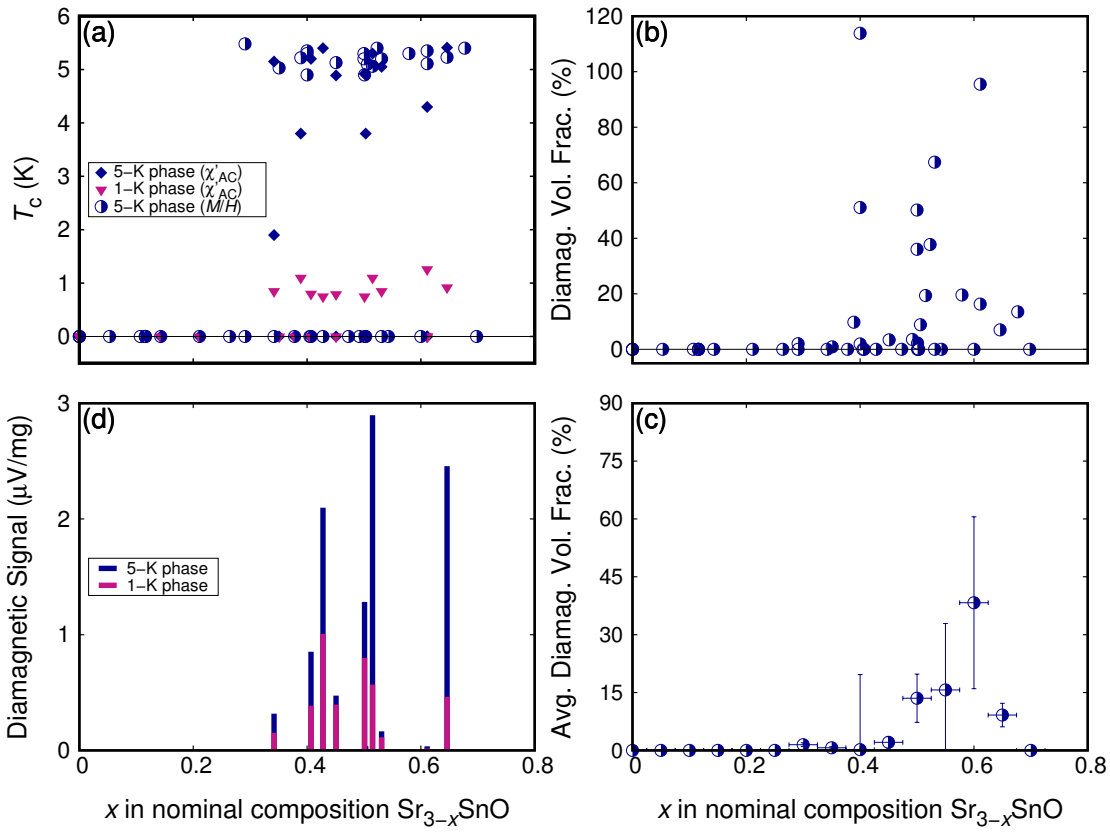

Figure 6.7: (a) T_c as a function of x based on the DC magnetization (down to 1.8 K) and the AC susceptibility (down to 0.1 K). (b) Diamagnetic volume fraction evaluated using DC magnetization data at 1.8 K, without demagnetization correction. (c) Mass-weighted average of the diamagnetic volume fraction in (b) taken over 0.05 intervals of x indicated by horizontal error bars. The vertical error indicates the weighted standard error. (d) Shielding volume fractions of the 5-K and 1-K phases evaluated from χ_{AC}.

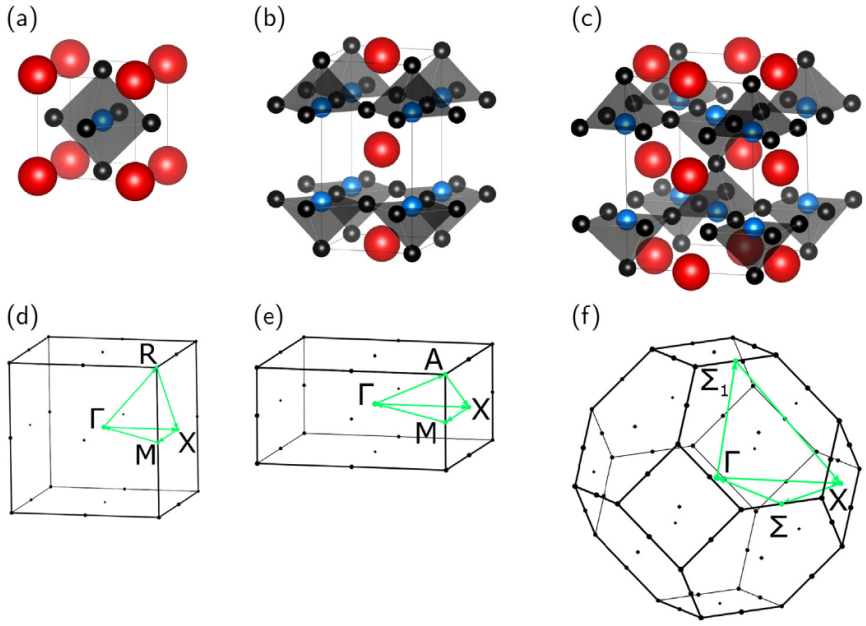

Figure 6.8: (a) Crystal structure of Sr_3SnO. The black, red, and blue spheres represent the strontium, tin, and oxygen atoms, respectively. The space group is $Pm3m$ (No. 221, O_h^1). (b, c) Hypothetical structures of strontium-deficient $Sr_{3-x}SnO$ ($x = 0.5$). The structure (b) has the layers of the strontium deficiency resulting in a simple tetragonal lattice with the space group $P4mmm$ (No. 124, D_{4h}^1). On the other hand, in the structure (c), the strontium atoms are vacant alternatively from different layers, resulting in a body-centered tetragonal lattice with the space group $I4mmm$(No. 139, D_{4h}^{17}). The figures of the crystal structures were prepared with the program VESTA [16]. Brillouin zones of the (d) simple cubic, (e) simple tetragonal, and (f) body-centered tetragonal lattices. The k paths for the band-structure plots in Figs. 6.10 $\Gamma - X - M - \Gamma - R - X$ for (d),$\Gamma - X - M - \Gamma - A - X$ for (e), and $\Gamma - X - \Sigma - \Gamma - \Sigma - X$ for (f). The figures of the Brillouin zones were drawn with the program XCrySDen [125].

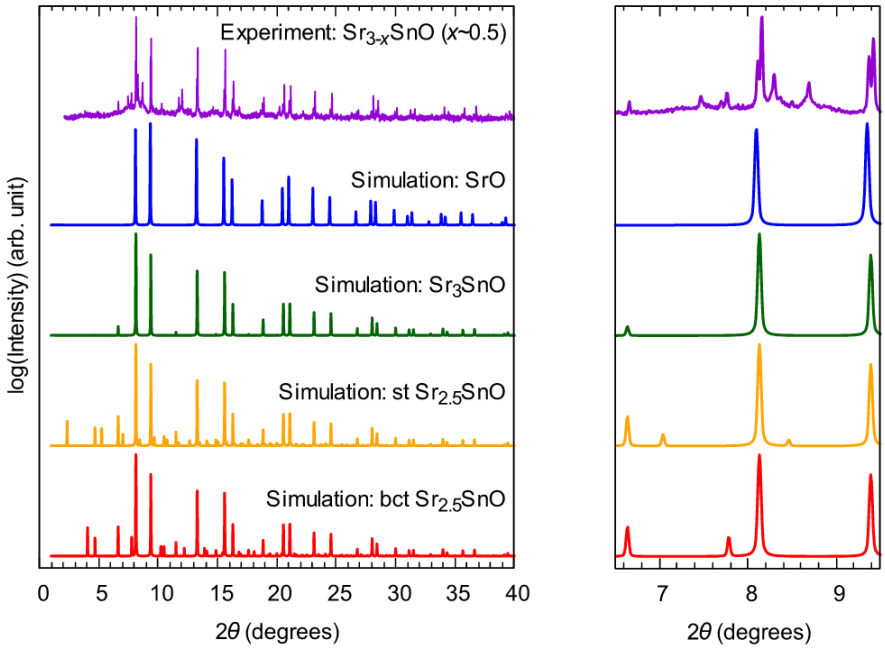

Figure 6.9: Observed and simulated powder-X-ray-diffraction spectra of $Sr_{3-x}SnO$ and SrO. The purple plot is the experimental data for the superconductive $Sr_{3-x}SnO$ ($x \sim 0.5$; $T_c \sim 5.2$ K) measured at 30 K and at SPring-8. The blue, green, yellow, and red plots are the simulated patterns for SrO, Sr_3SnO, the simple-tetragonal (st) $Sr_{3-x}SnO$ ($x = 0.5$) shown in Fig. 6.8(b), and the body-centered-tetragonal (bct) $Sr_{3-x}SnO$ ($x = 0.5$) shown in Fig. 6.8(c), respectively. The spectra were calculated using VESTA [16].) [4].

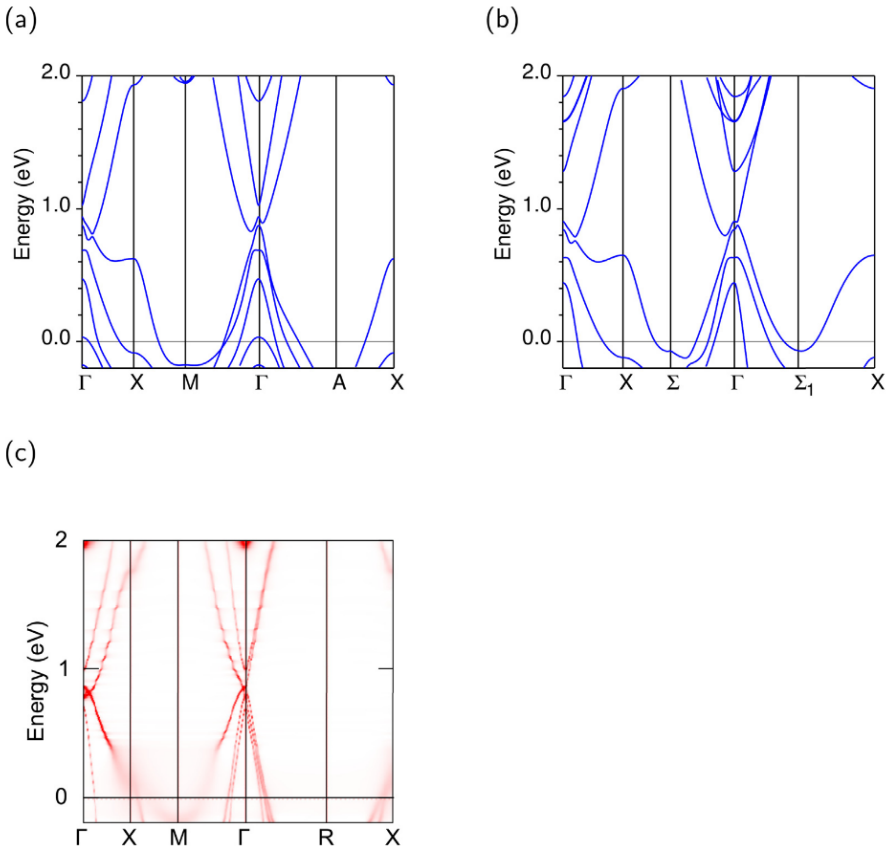

Figure 6.10: Band structures of $Sr_{3-x}SnO$ ($x = 0.5$) calculated using (a, b) WIEN2k [78] and (c) AkaiKKR (Machikaneyama) [79]. The panels (a) and (b) correspond to the hypothetical deficient structures presented in Figs. 6.8(a) and (b), respectively. (c) is the Bloch spectral function calculated using the coherent potential approximation [19,20] with a strontium deficiency of 17% ($x = 0.51$). In the blurred region, states have finite lifetime because of the scattering by the random deficiency [4].

Chapter 7

Additional Properties of $Sr_{3-x}SnO$

We include additional properties of $Sr_{3-x}SnO$ in this chapter. We observed paramagnetic Meissner effect in some $Sr_{3-x}SnO$ samples. Also, the NMR results showing unusual $1/T_1$ behavior, possibly originating from Dirac electrons, are discussed. The NMR measurements were performed by S. Kitagawa.

7.1 Paramagnetic Meissner Effect in $Sr_{3-x}SnO$

The paramagnetic Meissner effect is reported in field-cooling (FC) measurements of some superconductors, and the origin of this effect is attributed to vortex dynamics [126, 127, 128] or surface Andreev bound states [129, 130, 131, 132]. The paramagnetic Meissner effect arises in samples multiple superconducting phases, such as the case for In-Sn alloys [133]. The effect originating from surface Andreev bound states is an indication of odd-frequency Cooper pairs, and this has been shown to originate from small topological superconductors [130]. This paramagnetic Meissner effect is observed DC magnetization FC curves of $Sr_{3-x}SnO$ as shown in Fig. 7.2, and is not observed in the zero-field-cooling (ZFC) curves shown in Fig. 7.1. The samples were heated to 12 K between these measurements and field was removed before cooling back down to 2 K.

The onset of both diamagnetic and paramagnetic transitions in samples showing the paramagnetic Meissner effect is significantly higher than that of samples with 5 K transition presented in the previous Chapters. The transition starts at $\sim$ 10 K whenever it is observed, and it is much broader than that at 5 K. The ZFC curves in Fig. 7.1 for different applied magnetic fields shows the typical diamagnetic superconducting signal, but the magnitude of curves gets weaker with

higher applied magnetic fields. The FC curves in Fig. 7.2 show diamagnetic signal for fields up to 3 Oe, which flips to a paramagnetic effect for 4 Oe and a stronger paramagnetic signal for 5 Oe. Increasing the fields above 5 Oe up to 20 Oe, the paramagnetic signal persists and slowly decreases in magnitude. This effect was observed in many samples with similar onset, but the paramagnetic effect appears at varying magnetic fields.

These results may suggest that T_c of $Sr_{3-x}SnO$ may be increased to $\sim$ 10 K. In these samples the $\sim$ 10 K phase is a minor one, but altering the composition with different ratios of Sr:Sn:O or introducing new dopants may increase the bulk T_c. If we assume this effect originates from superconductivity in $Sr_{3-x}SnO$, then this may be related to exotic effects like surface Andreev bound states due to odd-frequency Cooper pairing [132, 130, 131], which may be topological in nature. However, the samples where this effect was measured contained phases below 5 K as evidenced by C_P and χ_{AC} measurements presented in earlier Chapters. The existence of another minor phase with a T_c of $\sim$ 10 K may explain these measurements and warrants further investigation in $Sr_{3-x}SnO$ samples. It should be noted that both diamagnetic and paramagnetic signals with onset of $\sim$ 10 K in these samples are not observed in χ_{AC} measurements. χ_{AC} measurements with various current frequency and heating/cooling were performed on these $Sr_{3-x}SnO$ samples, but the signal at $\sim$ 10 K was not observed. Further investigation on this higher transition is likely to reveal interesting physics in $Sr_{3-x}SnO$, and warrants further investigation.

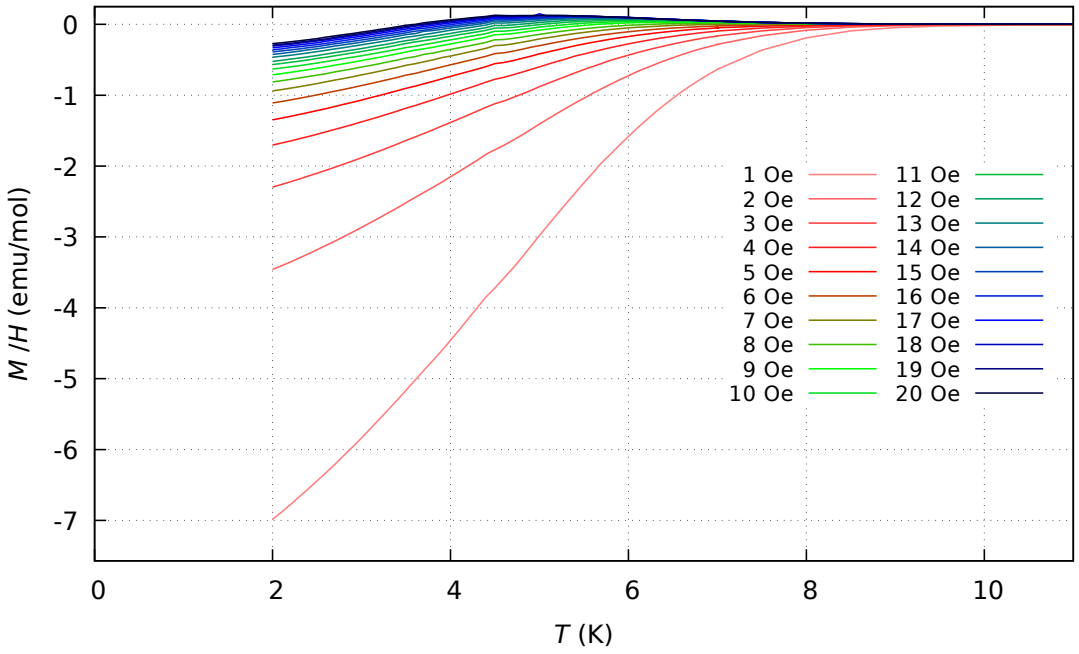

Figure 7.1: Zero-field-cooling DC magnetization as a function of temperature in $Sr_{3-x}SnO$.

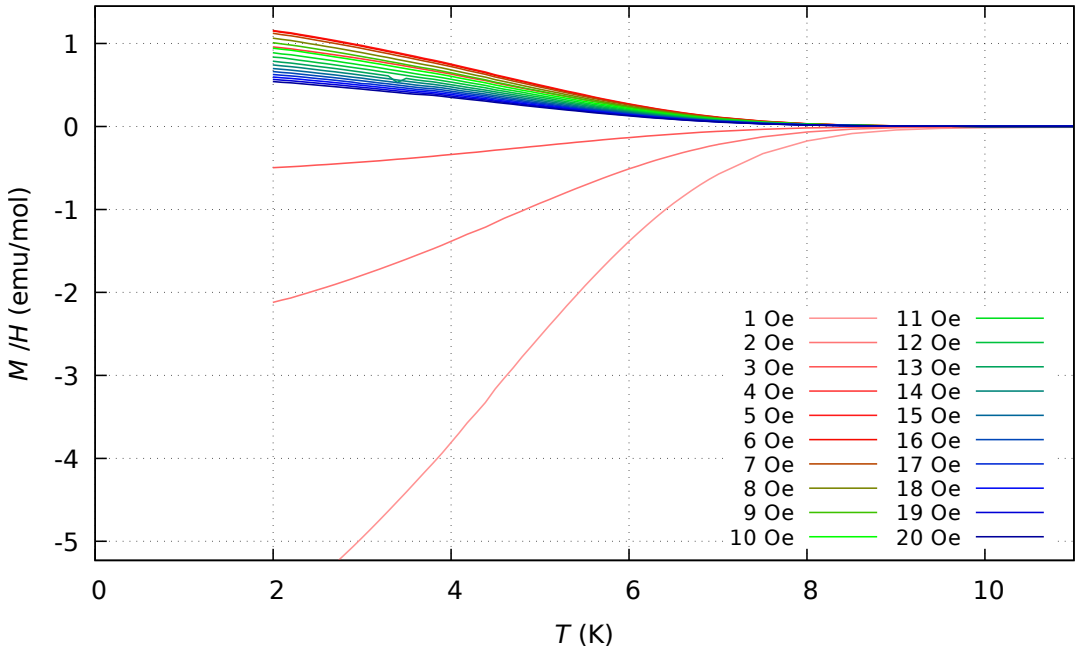

Figure 7.2: Field-cooling DC magnetization as a function of temperature in $Sr_{3-x}SnO$.

7.2 NMR on $Sr_{3-x}SnO$

NMR spectroscopy can give us information about microscopic nature of phases containing a specific element in our samples. We performed NMR measurement of ^{119}Sn, and the NMR spectra at $T = 5$ K in all measured samples is shown in Fig. 7.4. The intensity of each spectrum was normalized by the total area. In NMR spectrum measurements, a resonance magnetic field $\mu_0 H_{\rm res}$ is shifted as a function of Knight shift K. All spectra contained the signal of a Sn metal with $K = 0.717$ % originated from an impurity phase and/or the decomposition of samples during preparation for measurement. Other than the signal of Sn metal, a two-peaks structure was observed in all samples, indicating that all samples contain two phases containing Sn. The intensity ratio of the two peaks was similar between the samples with similar x and was different between samples with different x. Since the intensity of left peak in sample A and B was relatively higher than that in sample C and D, the left and right peaks correspond to the Sr deficiency and nearly stoichiometric phases, respectively.

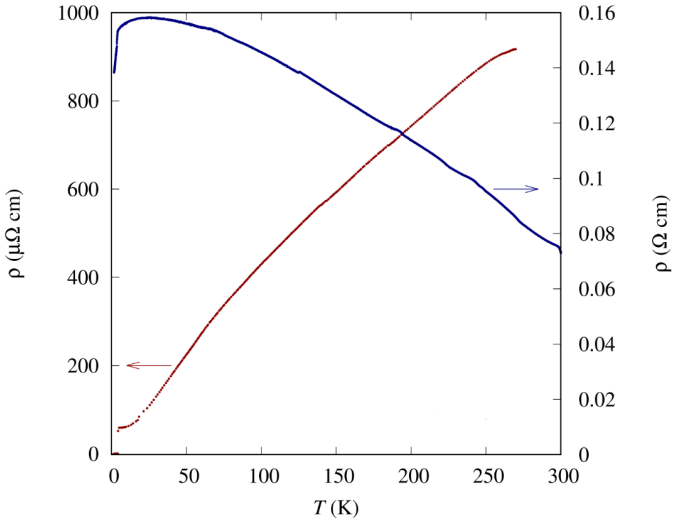

Figure 7.3: Resistivitiy as a fucntion of temperature of $Sr_{3-x}SnO$ for $x = 0.0$ (blue) and $x = 0.5$ (red).

To investigate the electronic properties of each peak, we measured the temperature dependence of $1/T_1T$ as shown in Fig 7.5. $1/T_1T$ at left peak was independent of temperature between 1.5 K and 150 K, which is a typical behavior of a conventional metal. In addition, the value of $1/T_1T$ was comparable to that in Sn metal. This led us to conclude that the left peak originates from a conventional metallic phase. The value of $1/T_1T$ at the left peak in sample C was almost the same as that in sample A, indicating that the left peak originates from the same phase in both samples. In contrast, $1/T_1T$ at the right peak was 400 times smaller than that at the left peak. In

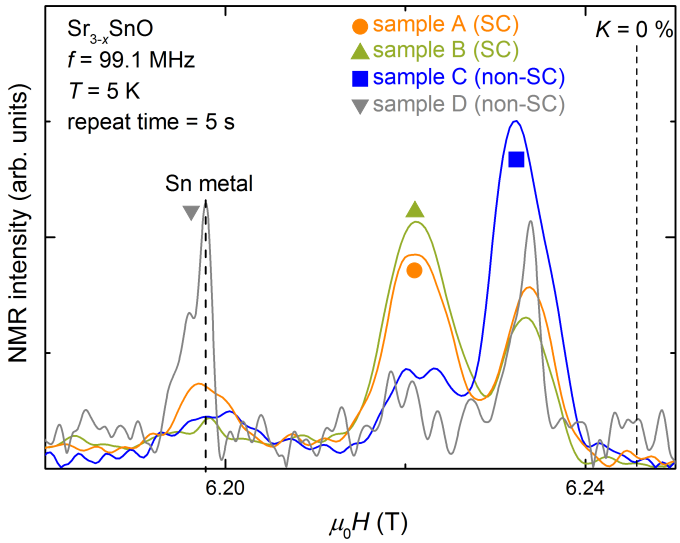

Figure 7.4: ^{119}Sn-NMR spectra at $T = 5$ K and $f = 99.1$ MHz in all measured samples. The repetition time of NMR pulse was 5 seconds, which is shorter than T_1 at left peak. The intensity of each spectrum was normalized by the total area. The positions of $K = 0$ % and Sn metal ($K = 0.717$ %) were represented by broken lines. SC and non-SC indicate whether the sample shows superconductivity. [Figures by S. Kitagawa]

the case of conventional metals, $1/T_1T$ is proportional to $D(E_F)^2$ where $D(E_F)$ is the density of states (DOS) at Fermi energy. Therefore, naively, we expect the small value of $1/T_1T$ to indicate a low density of states around Fermi energy in the nearly stoichiometric phase. Furthermore, the temperature dependence of $1/T_1T$ at right peak was unusual; $1/T_1T$ stays constant below 120 K and is almost proportional to T above 150 K. In a conventional semiconductors or insulators, $1/T_1T$ typically shows exponential decay when the excitation energy k_BT gets smaller than an activation energy Δ, where k_B is Boltzmann constant. Therefore, the nearly stoichiometric phase is not semiconducting based on NMR results, although resistivity shows weakly semiconducting behavior as shown in Fig. 7.3.

We performed ^{119}Sn-NMR measurements to investigate the difference in the ground state between stoichiometric non-superconducting to Sr-deficient superconducting samples. In all measured samples, two-peaks structure was observed in the NMR spectrum, indicating that the amount of Sr deficiency does not change continuously but is stabilized only at certain x values discontinuously. This supports the idea of a superconducting phase, stabilized at a specific values of x, giving rise to one of the two superconducting transitions at 5 and 1 K. Furthermore, the $1/T_1$ measurements suggest that a conventional metallic state induced by high level of hole-doping shows superconductivity, supporting the resistivity data of superconducting $Sr_{3-x}SnO$ samples. On the other hand, the non-superconducting phase shows an unusual temperature dependence of

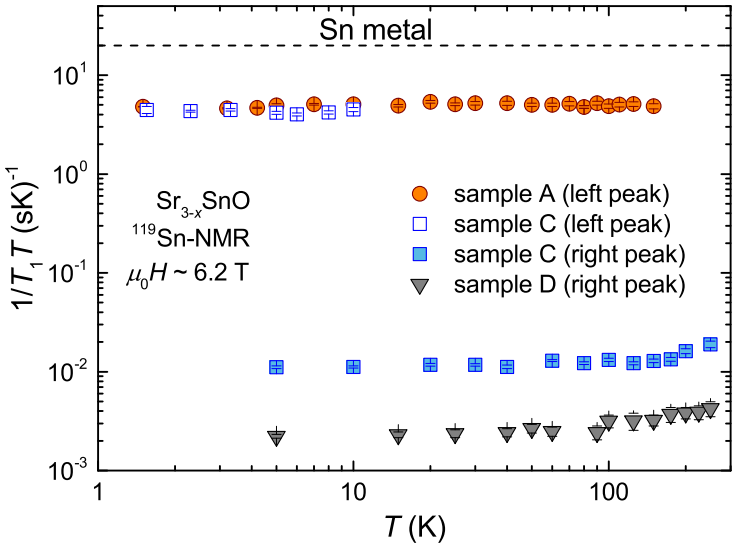

Figure 7.5: Temperature dependence of $1/T_1T$ at different positions and samples, which is plotted on a logarithmic scale. $1/T_1T$ was measured around 6.2 T. The broken line represent the value of $1/T_1T$ on Sn metal. [Figures by S. Kitagawa]

$1/T_1$ above 150 K, which can be understood by considering the band structure. A similar temperature dependence is observed in the Weyl semimetal TaP above 30 K [134], explained by the Dirac dispersion in this material. The unusual behavior in $Sr_{3-x}SnO$ may originate from the Fermi level being in the vicinity to the Dirac crossing in stoichiometric non-superconducting samples.

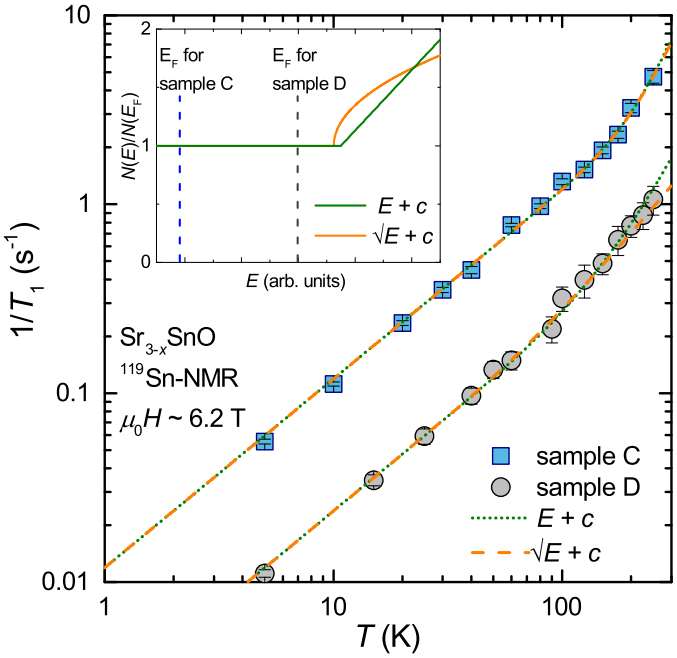

Figure 7.6: Temperature dependence of $1/T_1$ calculated by two models. To compare with the experimental data, we also show $1/T_1$ measured at right peak in sample C and D. (Inset)The schematic images of the energy dependence of DOS in two models. [Figures by S. Kitagawa]

Chapter 8

Conclusions

8.1 Summary and Conclusions

We have provided evidence for bulk superconductivity in Sr_3SnO with an onset of about 5 K, Fig. 8.1(b), marking the first superconductivity among antiperovskite oxides. The evidence for superconductivity included diamagnetic signal from DC magnetization, χ_{AC}, and zero resistivity. The synthesis of the first few superconducting samples suffered from uncontrolled evaporation of Sr. These samples were sealed under vacuum, Sr with 99.9% purity was used, and the reaction was carried out at 825°C.

After optimization of various synthesis parameters, we found that addition of argon with pressure of 30 kPa at room temperature allowed us to suppress Sr evaporation. A molar Sr:SnO ratio of 2.5 and Sr of 99.99% purity allowed us to produce bulk polycrystalline $Sr_{3-x}SnO$ with a superconducting volume fraction of around 100%. With these improved synthesis conditions, we carried a thorough investigation of the superconductivity in $Sr_{3-x}SnO$ on deficiency x.

We performed a comprehensive bulk and microscopic investigation of $Sr_{3-x}SnO$ samples with x varying from 0.0 to 0.7. From Mössbauer spectra, we found evidence for the unusual Sn^{4-} state with the filled $5p$ orbital in stoichiometric and deficient $Sr_{3-x}SnO$. We have demonstrated that superconductivity appears for samples with deficiency $0.35 < x < 0.70$. All superconducting samples exhibit two superconducting transitions, at about 5 K and 1 K, as shown in Fig. 8.1(a). The T_c of these transitions seems to not change as a function of x, as shown in Fig. 8.1(c). The volume fraction of the 5 K phase seems to be highest in the vicinity of $x = 0.5$. The present findings clarify the composition necessary for the appearance of superconductivity in $Sr_{3-x}SnO$, and push forward this material for further investigation of its unconventional properties.

We propose topological superconductivity in this compound reflecting the topological nature of the band structure in the normal state. Also, our theoretical investigation of deficient $Sr_{3-x}SnO$ reveals that the topological nature the band structure is preserved even for $x = 0.5$. NMR measurements reveal an unusual behavior of $1/T_1$ at low temperature in non-superconducting compounds,

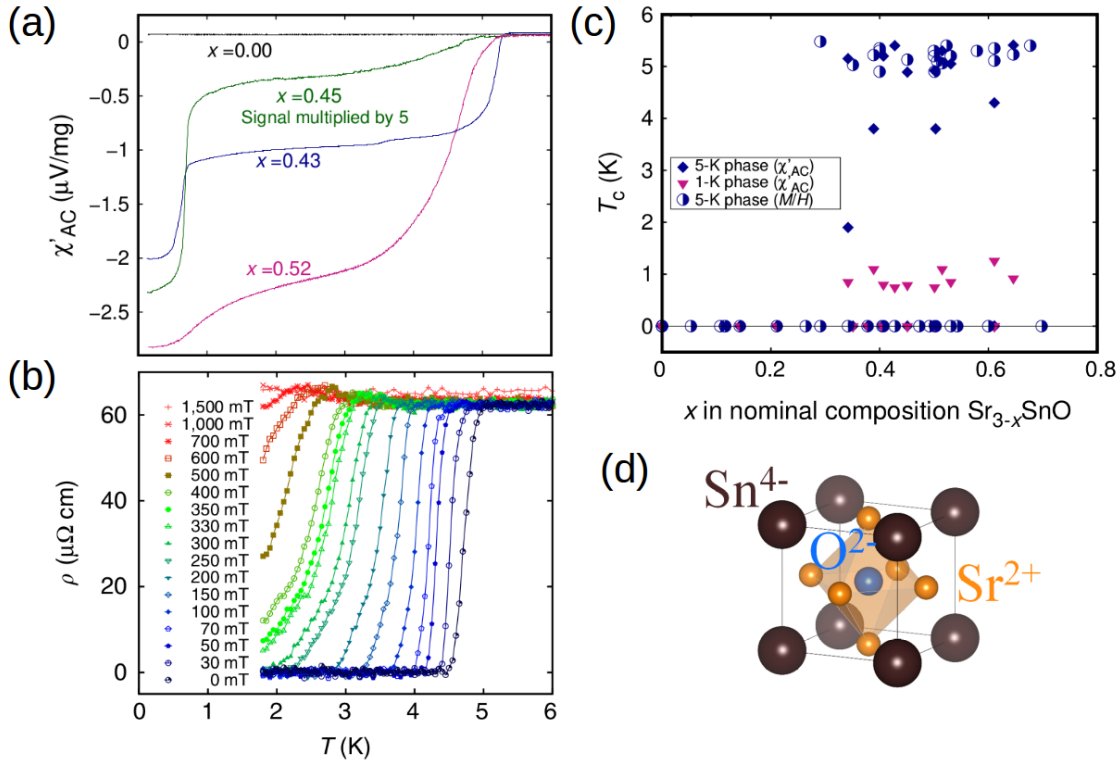

Figure 8.1: (a) χ_{AC} of $Sr_{3-x}SnO$ with various x, showing transitions at 5 and 1 K. (b) Resistivity of $Sr_{3-x}SnO$ at low temperature under different magnetic fields. (c) T_c of 5 and 1 K phases as a function of x in "$Sr_{3-x}SnO$". (d) Crystal structure of Sr_3SnO with oxidation state of ions. Figure produced with VESTA [16].

which has implications for the linear dispersion near the Dirac point. Also, we observed paramagnetic Meissner effect in some samples with an onset of approximately 10 K, suggesting the existence of another phase with this higher T_c.

Mirroring the rich variety of properties in perovskite oxides, the present work opens a door to superconductivity as well as other interesting phenomena in antiperovskite oxides with unusual metallic anions. Clarifying the dependence of superconductivity on x in $Sr_{3-x}SnO$, enabled by optimization of the synthesis conditions, serves as an important basis toward investigation of the proposed topological superconductivity in this class of materials.

8.2 Suggestions for Future Work

Investigation of the band structure of Sr_3SnO using ARPES is an important next step towards realizing the topological nature of this compound. To achieve this, producing single crystals is desirable and should be the next goal of this antiperovskite oxides project. Also, making thin-films of antiperovskite oxides can allow for ARPES measurements and may reveal interesting properties different from those observed in the polycrystalline or single crystals.

Producing superconducting single crystals or thin-films is the next step towards investigating the possibility of topological superconductivity in these compounds. Inducing superconductivity with doping and/or substituion, rather than deficiency, in the bulk polycrystalline Sr_3SnO may lead to a viable route to producing superconducting single-crystals or thin-films in the future.

After superconducting single-crystals or thin-films are achieved, some clever technique should be developed to prove the topological nature of the superconductivity itself, rather than the topological nature of the normal state.

Acknowledgement

First of all, I would like to express the greatest gratitude to Prof. Y. Maeno, my supervisor, for his guidance, support, long discussions throughout my three years in this laboratory. Next, I would like to thank Assis. Prof. S. Yonezawa for countless technical help and for teaching me about various theoretical concepts. I acknowledge Prof. M. Sato, Dr. S. Kobayashi, T. Fukumoto for a fruitful theory collaboration. I thank Prof. G. Bednorz, Prof. Y. Asano, Prof. M. Franz, Prof. M. Sigrist, and Prof. J. Checkelsky for valuable discussions.

I would like to thank Prof. Y. Matsuda, Prof. Y. Yanase, Assis. Prof. Y. Kasahara, Assis. Prof. S. Kasahara, Dr. T. Watashige, Dr. Yamashita for discussions and sharing various equipments throughout my PhD years. I thank Prof. H. Akai and the members of Computational Materials Design Workshop at Osaka University for teaching me about the AkaiKKR method of band structure calculation. I am grateful to Dr. H. Takatsu, Assoc. Prof. C. Tessel, and Prof. H. Kageyama for allowing me to join them for XRD experiment at SPring-8. I appreciate the contribution of Assoc. Prof. S. Kitao and Prof. M. Seto in performing Mössbauer spectroscopy experiments.

I acknowledge Prof. K. Ishida and Assis. Prof. S. Kitagawa for all of their support both for scientific activity and for my student life in Laboratory. A special thanks to Assis. Prof. S. Kitagawa for performing NMR measurements on $Sr_{3-x}SnO$ samples. I appreciate all the other members, former and present, of the Quantum Materials Laboratory at Kyoto University. Especially I thank A. Ikeda and J.N. Haussmann for their significant contribution to the antiperovskite oxide project, they played an essential role in pushing forward the physics and chemistry, respectively. Also, I would like to thank the other group members Dr. A. Shahbaz, Dr. C. Sow, Dr. M.P. Jimenez-Segura, Dr. T. Yamanka, I. Kostylev, A. Shi, Y. Yasui, M. Manago, D. Nishimiya, Y. Sugimoto, T. Higuchi, K. Tajiri, R. Takaki, T. Kawamura, M. Kunieda, G. Nakamine, H. Suwa, R. Numasaki, and K. Yonekawa who have taught me various experimental techniques, theoretical concepts, and computer skills. I thank the exchange students in the group who have brought unique perspective on the research, and have made time at the group more enjoyable; namely, H.G. Lee, I. Marković, and C. Palomares-Garcia. Also, I want to thank T. Kodama for computer help, and K. Takamiya for endless administrative help throughout the three years.

My PhD course study at Kyoto University is supported by Research Scholarship from Ministry of Education, Culture, Sports, Science and Technology (MEXT) of Japan. This work is supported

by Grants-in-Aids from Japan Society for the Promotion of Science (JSPS) and MEXT, and by Izumi Science and Technology Foundation.

I want to thank the many friends who have supported me throughout my PhD years in Kyoto. Especialy, I would like to thank my friends Iyas, Yaman, Jasper, Shinichi, Shinya, Miki, and Reimi. Also, I would like to thank members of the Kyoto University Badminton Club and members of SSDS team for making my time in Kyoto enjoyable outside of the lab.

Finally, I sincerely thank my parents, Ramadan & Faiza, and my sister Rawa for their support and encouragement to always achieve more in life.

Appendix A

Temperature Dependence of High Energy X-ray Diffraction

A.1 Low T XRD Measurement of $Sr_{3-x}SnO$

A Sr-deficient $Sr_{3-x}SnO$ sample was examined at SPring-8, which was synthesized with starting composition of $Sr_{2.5}SnO$. This sample was synthesized by heating to 825°Cfor 3 hours, and showed superconductivity. The volume fraction for one piece is 100% at 2 K from DC magnetization measurement, and another piece shows a volume fraction of over 30% at 2 K from both AC and DC magnetization measurements. This sample was deemed a good representative of a superconducting $Sr_{3-x}SnO$ sample, and developed the interest for investigating the structure at SPring-8 despite the not so clean XRD measured using Bruker D8 machine.

Performing Rietveld refinement on this sample was challenging due to multiple phases, and an estimate of lattice parameter was done using the three peaks at 111, 200, and 220, and the average was used to identify the two main phases in synchrotron measurement. The lattice parameters of 5.1391 Å and 5.1620 Å are identified for the major and minor phases, where the major phase is identical to that in other $Sr_{3-x}SnO$ samples, but the minor phase differs slightly from the one typically seen in $Sr_{3-x}SnO$ samples with lattice parameter 5.1598 Å. As for the multiple impurities in this sample, the strongest peaks between (111) and (200) peaks of the main phase may belong to Sr_2SnO_4. We measured the XRD at low T in this sample, to examine if any changes in the crystal structure occur with cooling. As seen in Fig. A.1, no clear small angle diffraction peak emerges as we lower the temperature. The position of the peaks is slightly shifted to the right open cooling, which reflects the shrinking of the unit cell.

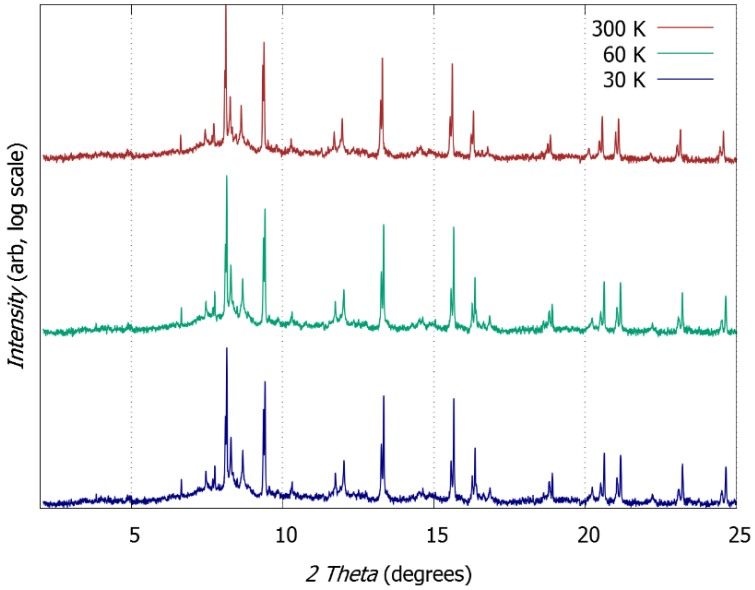

Figure A.1: Low temperature, 60 and 30 K, and room temperature XRD measurement of $Sr_{3-x}SnO$ with $x = 0.5$ performed at SPring-8. A log scale is used to emphasize small peaks.

A.2 High T XRD Measurement of Sr_3SnO

A stoiciometric Sr_3SnO sample (AP119) was examined at SPring-8, which was synthesized with starting composition of $Sr_{3.1}SnO$. This sample was synthesized using a two-step synthesis of 2.5 hours at 1200°Cfollowed by 48 hours at 900°C, and showed no evidence of superconductivity. This sample showed the cleanest X-ray diffraction from Bruker D8 machine. Performing Rietveld refinement on this sample was fairly easy, and the lattice parameter found from Rietveld refinement and compared to the value calculated using the three peaks at 111, 200, and 220. The lattice parameters of 5.1368 Å is identified for the only phase in this sample, which is slightly smaller than the major phase observed in other samples with some deficiency. This result is interesting, and can be due to a small tolerance for deficiency in $Sr_{3-x}SnO$. If this is true, then a large volume fraction superconducting sample may be possible with much less deficiency in the starting composition, as long as the sample is homogenous after the reaction. Furthermore, the phase diagram currently estimated with large value of deficiency $0 < x < 0.8$ is an exaggeration due to the inhomogeneity of the samples. As for the multiple impurities in this sample, the peaks are very small and difficult to accurately identify. The result from SPring-8, and comparison with Bruker D8 data is presented in Fig. A.2.

The diffraction pattern as temperature is raised in 100 K intervals between 300 K and 1,000 K are shown in Fig. A.4, on a logarithmic scale. The appearance of a shoulder peak at about

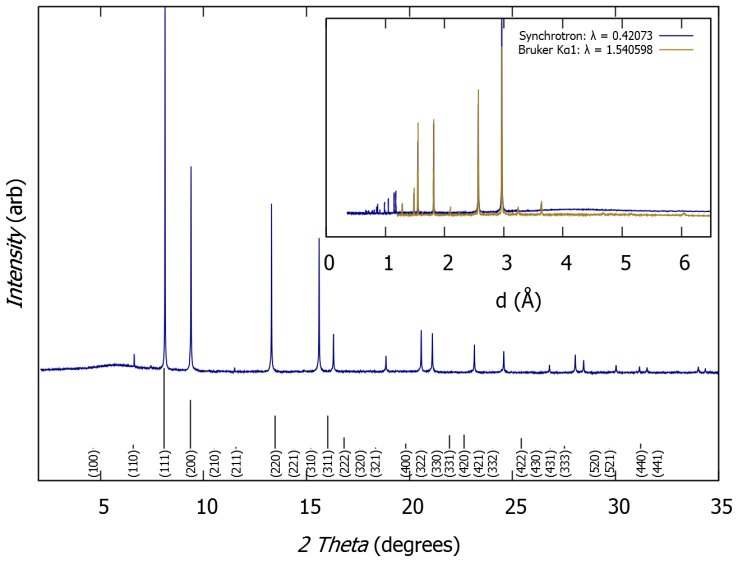

Figure A.2: High energy XRD measurement of Sr_3SnO. The inset shows the diffraction pattern as function of d spacing, comparing the SPring-8 (blue) and Bruker D8 results (gold).

13.1 degrees is perhaps most noticeable, and appears at a temperature of 600 K. At 700 K and above, peaks start to appear around 7.5 and 9.5 degrees, and these peaks become at the highest temperature of 1,000 K. These peaks double at 7.5 are characteristic of Sr_2Sn and can be explained by the decomposition of Sr_3SnO into Sr_2Sn and another phase. To identify this phase, it is perhaps best to observe the diffraction pattern of the sample after cooling to 300 K from 1,000 K, and comparing to the original diffraction pattern at 300 K, shown in the Fig. A.3. In this figure, we can clearly see that the peaks observed during the heating are due to permanent decomposition of the sample. Also, the decrease in the main peaks after heating is another indication that some of the initial Sr_3SnO is no longer present. It should be mentioned that the measurement time for these two measurements are 180 s and 120 s for the before and after heating respectively, so the diffractions in the figure were normalized accordingly. The most interesting aspect of the two diffraction patterns is perhaps the shift in the position of the main peak, and the split of the main peak into two phases, one major phase and one minor phase with the lattice parameters 5.0920 Å and 5.1084 Å. I propose that this difference may result from one of two situations. One the shift in the capillary during the cooling from 1,000 K to 300 K, and two the difference in cooling rate to room temperature. In the initial synthesis, the samples are quenched with water down to room temperature, while in the X-ray diffraction experiment they are cooled down at a slower rate by leaving the capillary in contact with air. Further investigation on the effect of cooling rate on properties is needed to clarify this suspicion. Further analysis into this diffraction will be needed

before definitive conclusion on the nature of these two phases is made.

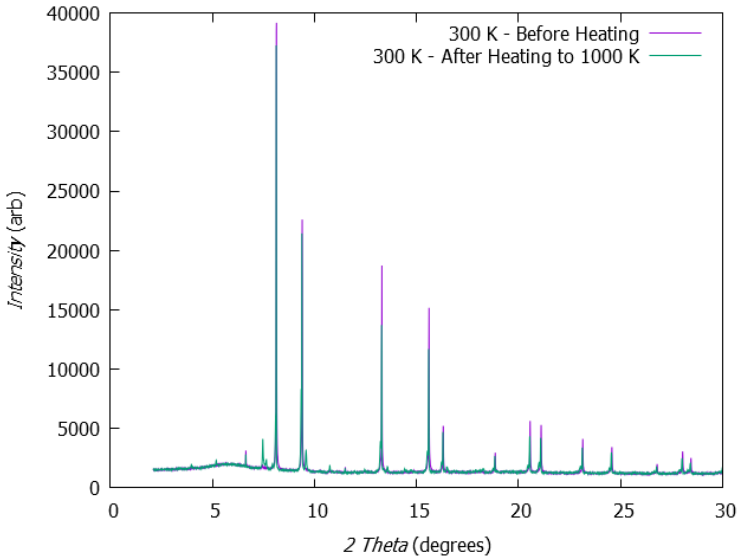

Figure A.3: High energy XRD measurements of Sr_3SnO at 300 K before (purple) and after (green) heating to 1000 K.

The change in position of the (111) and (220) peaks as a function of temperature is shown in Fig. A.5, and the lattice parameter at each temperature is calculated based on the position of these two peaks. The total unit cell volume, calculated based on the lattice parameter estimated from the (111) and (220) peak positions, as a function temperature is shown in Fig. A.6. A linear fit to the unit cell volume as a function of temperature is used to estimate $\mathrm{d}V/\mathrm{d}T$, which is then used to calculate the volume coefficient of expansion of Sr_3SnO. A coefficient of expansion, α_V, of 5.073×10^{-5} K^{-1} and 5.021×10^{-5} K^{-1} is estimated based on the (111) and (220) peaks, respectively.

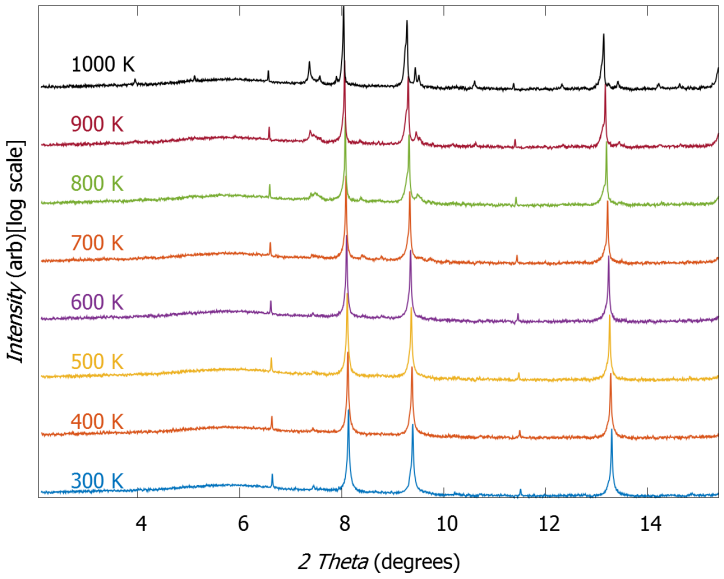

Figure A.4: High energy XRD measurements of Sr_3SnO at different temperatures between 300 to 1000 K.

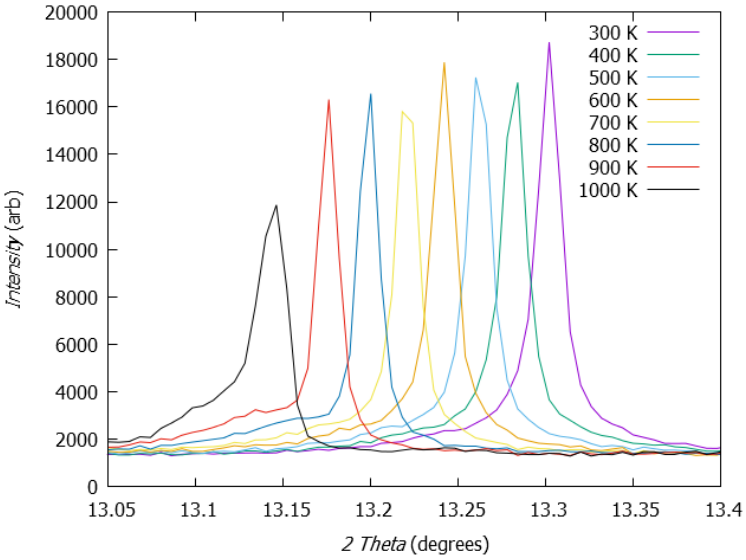

Figure A.5: High energy XRD measurement of (022) peak of Sr_3SnO at different temperatures between 300 to 1000 K.

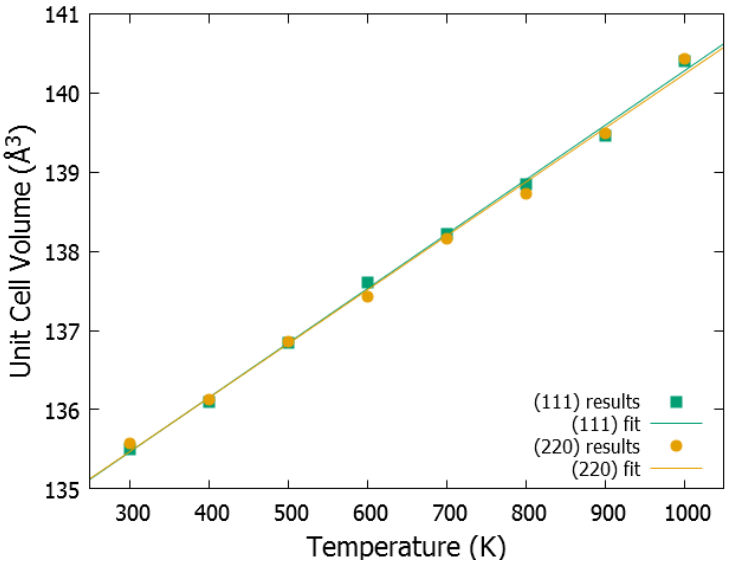

Figure A.6: Unit cell volume of Sr_3SnO at different temperature based on (111) and (022) peaks from high energy XRD measurement.

Appendix B

Temperature Dependence of Mössbauer Spectra

B.1 Low T Mössbauer Spectra of $Sr_{3-x}SnO$

Mössbauer spectra at low temperatures down to 6 K was performed on $Sr_{3-x}SnO$ samples with $x = 0.0$ and 0.5, presented in Figs. C.1 and B.2, respectively. The Mössbauer spectra at low temperature for $Sr_{3-x}SnO$ with $x = 0.0$ reveal that a satellite peak similar to the one observed in the $x = 0.5$ sample. Fitting for two curves allows us to estimate the position of both of these peaks in the $Sr_{3-x}SnO$ samples measured, and the peak change in peak position as a function of temperature is shown in Fig. B.3.

The temperature dependence of the two phases is the same in both samples, with $x = 0.0$ and $x = 0.5$. This indicates that the same phases are present in both samples, but with varying intensities as seen in the stronger signal of the shoulder peak in deficient sample (Fig B.2) compared with close to stoichiometric sample (Fig. C.1). These results are consistent with the two phases observed in NMR results in samples with different x values, discussed in Chapter 7. Also, if we consider the strength of the two signals other than that of pure β-Sn, we may conclude that the signals from Mössbauer originate from phases other than Sn. The possibility of the shoulder peak to originate from Sn sites in deficient $Sr_{3-x}SnO$ is discussed in Appendix C.

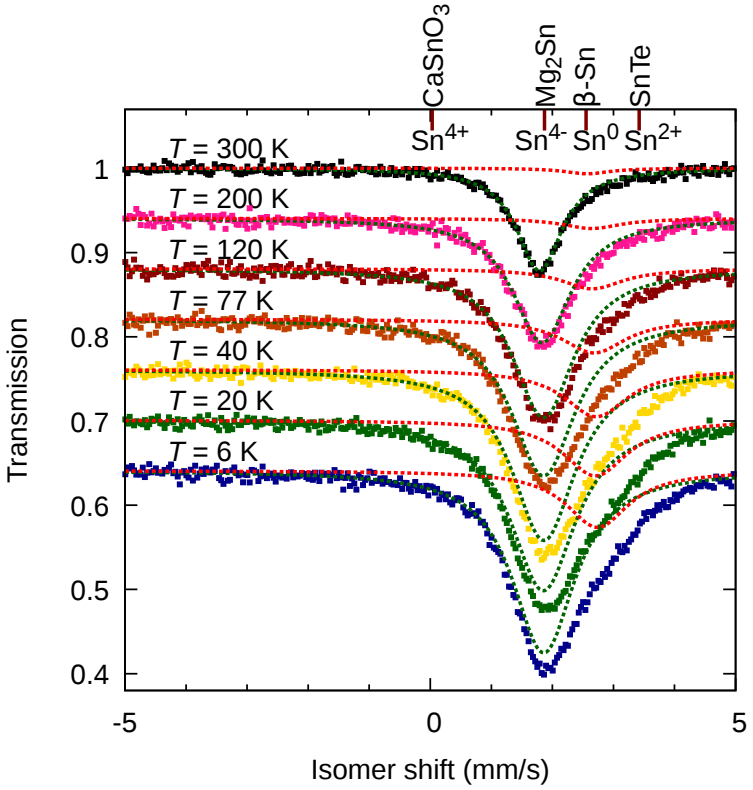

Figure B.1: Mössbauer spectra of $Sr_{3-x}SnO$ with $x = 0.0$ sample at various temperatures.

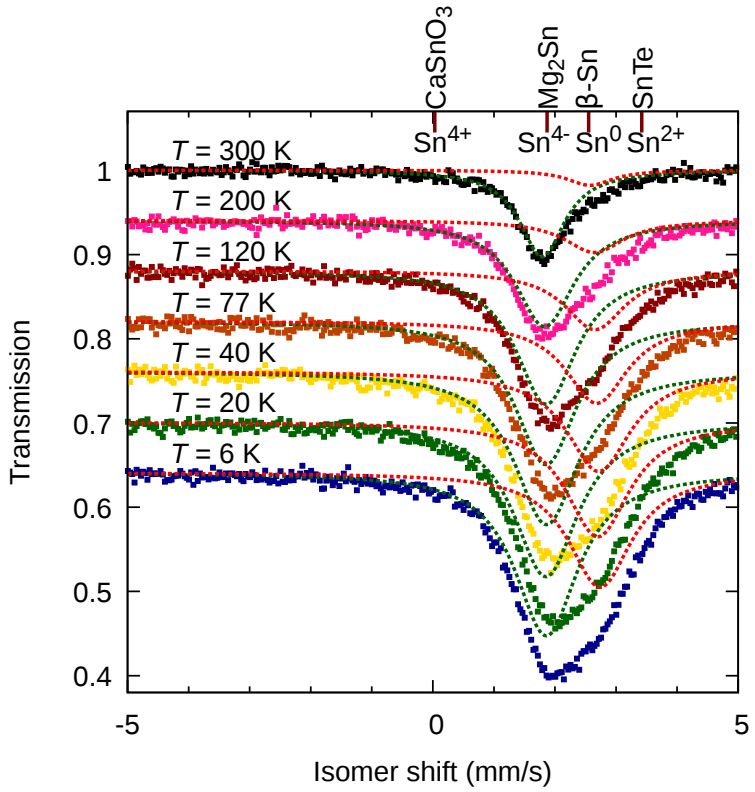

Figure B.2: Mössbauer spectra of $Sr_{3-x}SnO$ with $x = 0.5$ sample at various temperatures.

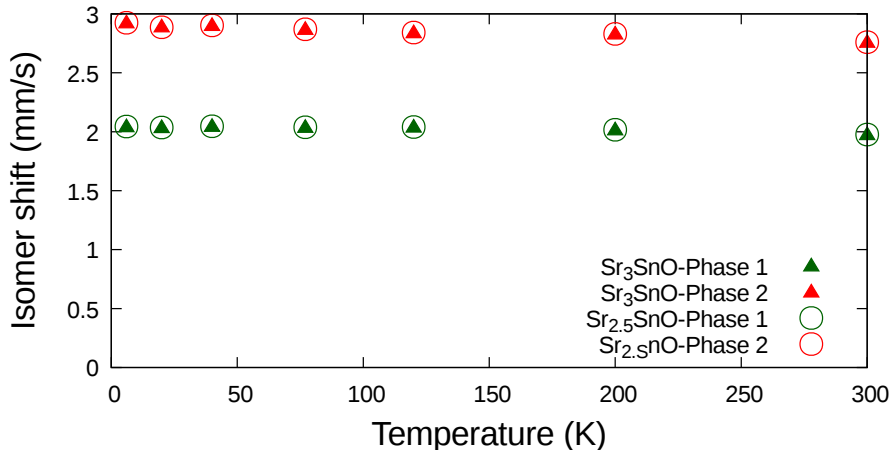

Figure B.3: Mössbauer isomer shift peak position of $Sr_{3-x}SnO$ with $x = 0.0, 0.5$ samples at various temperatures.

Appendix C

Theoretical Calculations of Mössbauer Isomer Shift

C.1 WIEN2k Caculations of Sr_3SnO and "$Sr_{2.5}SnO$"

The Mössbauer isomer shift is sensitive to electrons near the nucleus, and density functional theory (DFT) calculations can give some information about the electronic density at an atomic nucleus. It has been demonstrated that the electron density at the nucleus from DFT calculations, such as those carried out with WIEN2k, can be related to the isomer shift observed in Mössbauer spectroscopy [135, 136, 137]. The experimentally measured Mössbauer isomer shift and the electron density at the nucleus are linearly correlated, as shown in Fig. C.1. WIEN2k calculations were performed, radius R of the muffin-tin sphere of each atom was set as the following: $R_{Sr} = R_O = 2.41$ bohr and $R_{Sn} = 2.50$ bohr. We set the plane-wave cut off $RK_{max} = 8.0$, the highest angular momentum plus one $l_{max} = 10$, maximum magnitude of the largest vector in charge density Fourier expansion $G_{max} = 18$, and separation energy between the valence and core states -7 Ry. The k meshes used for Sr_3SnO and other Sn-containign compounds calculations are $12 \times 12 \times 12$, while for "$Sr_{2.5}SnO$" a k mesh of $12 \times 12 \times 6$ was used.

We performed our own calculations on β-Sn, Mg_2Sn, and $BaSnO_3$ using WIEN2k. The experimentally reported isomer shift of these compounds, with a $CaSnO_3$ source and $BaSnO_3$ chosen as origin, against the electron density at the nucleus from our calculations. A linear fit of our data points is similar to the one illustrated in Fig. C.1. If we consider the electron density at Sn nucleus in Sr_3SnO we have an estimated isomer shift of 1.77 mm/s based on WIEN2k calculation, which is comparable to the 1.83 mm/s observed experimentally. If we consider the density of electrons at the nuclei of the two Sn sites in $Sr_5Sn_2O_2$ ($Sr_{2.5}SnO$) simple tetragonal superlattice, we get an estimated isomer shifts of 1.84 and 2.41 mm/s for the sites away from and next to the Sr deficient site, respectively. The minor phase that increases with deficiency has an experimental isomer shift of 2.59 mm/s, which differs from the our estimated value of 2.41 mm/s from WIEN2k calculation

of this superlattice structure. Perhaps further calculations on other Sr-deficient structures can reveal the origin of this shoulder peak in the Mössbauer spectra. It is not clear whether the shoulder peak originates from a β-Sn impurity, although the expected isomer shift is 2.55 mm/s, if we consider the NMR data. A Sn metal peak is observed in the NMR measurement, but this peak has small intensity in all $Sr_{3-x}SnO$ relative to the two other peaks observed in all samples. The two peaks observed in Mössbauer experiment may have the same origin as the two peaks observed in NMR results shown in Chapter 7.

The main peak of the Sn isomer shift in $Sr_{3-x}SnO$ is similar to that of Mg_2Sn, which supports the 4− state in this compound. Also, WIEN2k calculations showing band structure with filled Sn-5p band in Sr_3SnO result in a predicted isomer shift of similar value to the one observed experimentally by us, which provides more evidence for the Sn^{4-} state in Sr_3SnO.

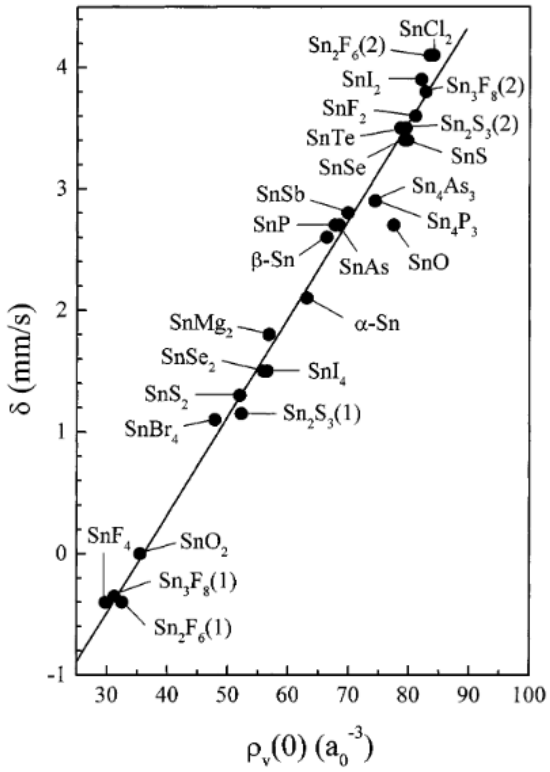

Figure C.1: Mössbauer isomer shift δ of ^{119}Sn in various compounds plotted against the valence electron density at the nucleus $\rho_V(0)$ [137].

Bibliography

[1] M. Oudah, A. Ikeda, J. N. Hausmann, S. Yonezawa, T. Fukumoto, S. Kobayashi, M. Sato, and Y. Maeno. Superconductivity in the antiperovskite Dirac-metal oxide $Sr_{3-x}SnO$. *Nature Commun.*, 7:13617, 2016.

[2] J. N. Hausmann, M. Oudah, A. Ikeda, S. Yonezawa, and Y. Maeno. Controlled synthesis of the antiperovskite oxide superconductor $Sr_{3-x}SnO$. *arXiv preprint arXiv:1712.09484*. Submitted to *Supercond. Sci. Technol.*, 2017.

[3] M. Oudah, J. N. Hausmann, S. Kitao, A. Ikeda, S. Yonezawa, M. Seto, and Y. Maeno. Evolution of Superconductivity with Sr-Deficiency in Antiperovskite Oxide $Sr_{3-x}SnO$. Submitted to *Phys. Rev. B: Rapid Communications*, LN15215BR, 2018.

[4] A. Ikeda, T. Fukumoto, M. Oudah, J. N. Hausmann, S. Yonezawa, S. Kobayashi, M. Sato, C. Tassel, F. Takeiri, H. Takatsu, et al. Theoretical band structure of the superconducting antiperovskite oxide $Sr_{3-x}SnO$. *Physica B*, 2017.

[5] J. G. Bednorz and K. A. Müller. Possible high T_c superconductivity in the Ba-La-Cu-O system. *Z. Phys. B*, 64(2):189–193, 1986.

[6] Y. Maeno, H. Hashimoto, K. Yoshida, S. Nishizaki, T. Fujita, J. G. Bednorz, and F. Lichtenberg. Superconductivity in a layered perovskite without copper. *Nature*, 372(6506):532–534, 1994.

[7] Y. Kamihara, T. Watanabe, M. Hirano, and H. Hosono. Iron-based layered superconductor $La[O_{1-x}F_x]FeAs$ (x = 0.05 - 0.12) with T_c = 26 K. *J. Am. Chem. Soc.*, 130(11):3296–3297, 2008.

[8] Y. Tokura. Critical features of colossal magnetoresistive manganites. *Rep. Prog. Phys.*, 69(3):797, 2006.

[9] S.-W. Cheong and M. Mostovoy. Multiferroics: a magnetic twist for ferroelectricity. *Nature Mater.*, 6(1):13–20, 2007.

[10] R. Cava, B. Batlogg, J. Krajewski, R. Farrow, L. Rupp, A. White, K. Short, W. Peck, and T. Kometani. Superconductivity near 30 K without copper: the $Ba_{0.6}K_{0.4}BiO_3$ perovskite. *Nature*, 332(6167):814–816, 1988.

[11] J. Jorgensen, B. Dabrowski, S. Pei, D. Hinks, L. Soderholm, B. Morosin, J. Schirber, E. Venturini, and D. Ginley. Superconducting phase of $La_2CuO_{4+\delta}$: A superconducting composition resulting from phase separation. *Phys. Rev. B*, 38(16):11337, 1988.

[12] H. Takahashi, K. Igawa, K. Arii, Y. Kamihara, M. Hirano, and H. Hosono. Superconductivity at 43 K in an iron-based layered compound $LaO_{1-x}F_xFeAs$. *Nature*, 453(7193):376–378, 2008.

[13] H. Luetkens, H.-H. Klauss, M. Kraken, F. Litterst, T. Dellmann, R. Klingeler, C. Hess, R. Khasanov, A. Amato, C. Baines, et al. The electronic phase diagram of the $LaO_{1-x}F_xFeAs$ superconductor. *Nature Mater.*, 8(4):305–309, 2009.

[14] J. Nuss, C. Mühle, K. Hayama, V. Abdolazimi, and H. Takagi. Tilting structures in inverse perovskites, M_3TtO (M= Ca, Sr, Ba, Eu; Tt= Si, Ge, Sn, Pb). *Acta Cryst. B*, 71(3):300–312, 2015.

[15] A. Widera and H. Schäfer. Übergangsformen zwischen zintlphasen und echten salzen: Die verbindungen A_3BO (mit A= Ca, Sr, Ba und B= Sn, Pb). *Mater. Res. Bull.*, 15(12):1805–1809, 1980.

[16] K. Momma and F. Izumi. VESTA 3 for three-dimensional visualization of crystal, volumetric and morphology data. *J. Appl. Crystallogr.*, 44(6):1272–1276, 2011.

[17] T. Kariyado and M. Ogata. Three-dimensional Dirac electrons at the Fermi energy in cubic inverse perovskites: Ca_3PbO and its family. *J. Phys. Soc. Jpn.*, 80(8):083704, 2011.

[18] T. Kariyado and M. Ogata. Low-Energy Effective Hamiltonian and the Surface States of Ca_3PbO. *J. Phys. Soc. Jpn.*, 81(6):064701, 2012.

[19] T. H. Hsieh, J. Liu, and L. Fu. Topological crystalline insulators and Dirac octets in antiperovskites. *Phys. Rev. B*, 90(8):081112, 2014.

[20] T. Kariyado and M. Ogata. Evolution of band topology by competing band overlap and spin-orbit coupling: Twin Dirac cones in Ba_3SnO as a prototype. *Phys. Rev. Materials*, 1:061201, Nov 2017.

[21] L. M. Schoop, L. S. Xie, R. Chen, Q. D. Gibson, S. H. Lapidus, I. Kimchi, M. Hirschberger, N. Haldolaarachchige, M. N. Ali, C. A. Belvin, et al. Dirac metal to topological metal transition at a structural phase change in Au_2Pb and prediction of Z_2 topology for the superconductor. *Phys. Rev. B*, 91(21):214517, 2015.

[22] L. He, Y. Jia, S. Zhang, X. Hong, C. Jin, and S. Li. Pressure-induced superconductivity in the three-dimensional topological Dirac semimetal Cd_3As_2. *npj Quantum Mater.*, 1:16014, 2016.

[23] L. Aggarwal, A. Gaurav, G. S. Thakur, Z. Haque, A. K. Ganguli, and G. Sheet. Unconventional superconductivity at mesoscopic point contacts on the 3D Dirac semimetal Cd_3As_2. *Nature Mater.*, 15(1):32–37, 2016.

[24] Z. Liu, B. Zhou, Y. Zhang, Z. Wang, H. Weng, D. Prabhakaran, S.-K. Mo, Z. Shen, Z. Fang, X. Dai, et al. Discovery of a three-dimensional topological Dirac semimetal, Na_3Bi. *Science*, 343(6173):864–867, 2014.

[25] "The 2016 Nobel Prize in Physics - Press Release". Nobelprize.org.

[26] K. v. Klitzing, G. Dorda, and M. Pepper. New method for high-accuracy determination of the fine-structure constant based on quantized Hall resistance. *Phys. Rev. Lett.*, 45(6):494, 1980.

[27] R. B. Laughlin. Quantized Hall conductivity in two dimensions. *Phys. Rev. B*, 23(10):5632, 1981.

[28] D. Thouless, M. Kohmoto, M. Nightingale, and M. Den Nijs. Quantized Hall conductance in a two-dimensional periodic potential. *Phys. Rev. Lett.*, 49(6):405, 1982.

[29] L. Fu and C. L. Kane. Topological insulators with inversion symmetry. *Phys. Rev. B*, 76(4):045302, 2007.

[30] J. E. Moore and L. Balents. Topological invariants of time-reversal-invariant band structures. *Phys. Rev. B*, 75(12):121306, 2007.

[31] F. D. M. Haldane. Model for a quantum Hall effect without Landau levels: Condensed-matter realization of the "parity anomaly". *Phys. Rev. Lett.*, 61(18):2015, 1988.

[32] A. AA, , and S. Beneslavski. Possible existence of substances intermediate between metals and dielectrics. *JETP*, 32:699, 1970.

[33] S. M. Young, S. Zaheer, J. C. Teo, C. L. Kane, E. J. Mele, and A. M. Rappe. Dirac semimetal in three dimensions. *Phys. Rev. Lett.*, 108(14):140405, 2012.

[34] J. E. Moore. The birth of topological insulators. *Nature*, 464(7286):194–198, 2010.

[35] J. C. Teo, L. Fu, and C. Kane. Surface states and topological invariants in three-dimensional topological insulators: Application to $Bi_{1-x}Sb_x$. *Phys. Rev. B*, 78(4):045426, 2008.

[36] G. Sharma, P. Goswami, and S. Tewari. Nernst and magnetothermal conductivity in a lattice model of Weyl fermions. *Phys. Rev. B*, 93(3):035116, 2016.

[37] L. Fu and C. L. Kane. Superconducting proximity effect and Majorana fermions at the surface of a topological insulator. *Phys. Rev. Lett.*, 100(9):096407, 2008.

[38] Y. S. Hor, A. J. Williams, J. G. Checkelsky, P. Roushan, J. Seo, Q. Xu, H. W. Zandbergen, A. Yazdani, N. Ong, and R. J. Cava. Superconductivity in $Cu_xBi_2Se_3$ and its implications for pairing in the undoped topological insulator. *Phys. Rev. Lett.*, 104(5):057001, 2010.

[39] H. Wang, H. Wang, H. Liu, H. Lu, W. Yang, S. Jia, X.-J. Liu, X. Xie, J. Wei, and J. Wang. Observation of superconductivity induced by a point contact on 3D Dirac semimetal Cd_3As_2 crystals. *Nature Mater.*, 15(1):38–42, 2016.

[40] X.-C. Pan, X. Chen, H. Liu, Y. Feng, Z. Wei, Y. Zhou, Z. Chi, L. Pi, F. Yen, F. Song, et al. Pressure-driven dome-shaped superconductivity and electronic structural evolution in tungsten ditelluride. *Nature Commun.*, 6, 2015.

[41] M. Bianchi, D. Guan, S. Bao, J. Mi, B. B. Iversen, P. D. King, and P. Hofmann. Coexistence of the topological state and a two-dimensional electron gas on the surface of Bi_2Se_3. *Nature Commun.*, 1:128, 2010.

[42] A. Nikitin, Y. Pan, Y. Huang, T. Naka, and A. de Visser. High-pressure study of the basal-plane anisotropy of the upper critical field of the topological superconductor $Sr_xBi_2Se_3$. *Phys. Rev. B*, 94(14):144516, 2016.

[43] N. F. Yuan, W.-Y. He, and K. T. Law. Superconductivity-induced ferromagnetism and Weyl superconductivity in Nb-doped Bi_2Se_3. *Phys. Rev. B*, 95(20):201109, 2017.

[44] S. Yonezawa, K. Tajiri, S. Nakata, Y. Nagai, Z. Wang, K. Segawa, Y. Ando, and Y. Maeno. Thermodynamic evidence for nematic superconductivity in $Cu_xBi_2Se_3$. *Nature Phys.*, 13(2):123–126, 2017.

[45] K. Matano, M. Kriener, K. Segawa, Y. Ando, and G.-q. Zheng. Spin-rotation symmetry breaking in the superconducting state of $Cu_xBi_2Se_3$. *Nature Phys.*, 12(9):852–854, 2016.

[46] M. Klintenberg. The search for strong topological insulators. *arXiv preprint arXiv:1007.4838*, 2010.

[47] K. Haddadi, A. Bouhemadou, L. Louail, and S. Bin-Omran. Inverse-perovskite oxides with, Ge, Sn, Pb: Structural, elastic and thermal properties. *Solid State Commun.*, 150(41):1995–2000, 2010.

[48] D. Cherrad, M. Maouche, M. Maamache, and L. Krache. Influence of valence electron concentration on elastic, electronic and optical properties of the alkaline-earth tin oxides A_3SnO (A= Ca, Sr and Ba): A comparative study with $ASnO_3$ compounds. *Physica B*, 406(14):2714–2722, 2011.

[49] M. Neupane, S.-Y. Xu, R. Sankar, N. Alidoust, G. Bian, C. Liu, I. Belopolski, T.-R. Chang, H.-T. Jeng, H. Lin, et al. Observation of a three-dimensional topological Dirac semimetal phase in high-mobility Cd_3As_2. *Nature Commun.*, 5:3786, 2014.

[50] C. L. Kane and E. J. Mele. Z_2 topological order and the quantum spin Hall effect. *Phys. Rev. Lett.*, 95(14):146802, 2005.

[51] X. Yan, B. Poudel, Y. Ma, W. Liu, G. Joshi, H. Wang, Y. Lan, D. Wang, G. Chen, and Z. Ren. Experimental studies on anisotropic thermoelectric properties and structures of n-type $Bi_2Te_{2.7}Se_{0.3}$. *Nano Lett.*, 10(9):3373–3378, 2010.

[52] M. Z. Hasan and C. L. Kane. Colloquium: topological insulators. *Rev. Mod. Phys.*, 82(4):3045, 2010.

[53] M. Tinkham. *Introduction to superconductivity*. Courier Corporation, 1996.

[54] S. Bud'Ko, G. Lapertot, C. Petrovic, C. Cunningham, N. Anderson, and P. Canfield. Boron isotope effect in superconducting MgB_2. *Phys. Rev. Lett.*, 86(9):1877, 2001.

[55] M. Sato and Y. Ando. Topological superconductors: a review. *Rep. Prog. Phys.*, 80(7):076501, 2017.

[56] S. Yonezawa. Bulk topological superconductors. *AAPPS Bulletin*, 26(3):3–11, 2016.

[57] A. P. Schnyder and P. M. Brydon. Topological surface states in nodal superconductors. *J. Phys.: Condens. Matter*, 27(24):243201, 2015.

[58] P. J. Ray. *Structural Investigation of $La_{(2-x)}Sr_{(x)}CuO_{(4+y)}$: Following a Staging as a Function of Temperature*. Niels Bohr Institute, Copenhagen University, 2015.

[59] Y. Kamihara, H. Hiramatsu, M. Hirano, R. Kawamura, H. Yanagi, T. Kamiya, and H. Hosono. Iron-based layered superconductor: LaOFeP. *J. Am. Chem. Soc.*, 128(31):10012–10013, 2006.

[60] H. G. Smith and J. O. Wilhelm. Superconductivity. *Rev. Mod. Phys.*, 7(4):237, 1935.

[61] T. Fässler and S. Hoffmann. $SrSn_3$–eine supraleitende Legierung mit freien Elektronenpaaren. *Z. Anorg. Allg. Chem.*, 626(1):106–112, 2000.

[62] S. Hoffmann and T. F. Fässler. $SrSn_4$: a superconducting stannide with localized and delocalized bond character. *Inorg. Chem.*, 42(26):8748–8754, 2003.

[63] X. Lin, S. L. Budko, G. D. Samolyuk, M. S. Torikachvili, and P. C. Canfield. Physical properties of $SrSn_4$ single crystals. *J. Phys.: Condens. Matter*, 23(45):455703, 2011.

[64] D. Di Sante, P. K. Das, C. Bigi, Z. Ergönenc, N. Gürtler, J. Krieger, T. Schmitt, M. Ali, G. Rossi, R. Thomale, et al. Three-Dimensional Electronic Structure of type-II Weyl Semimetal WTe_2. *Phys. Rev. Lett.*, 119(2):026403, 2017.

[65] J. Batool, S. M. Alay-e Abbas, A. Ali, K. Mahmood, S. Akhtar, and N. Amin. The role of intrinsic vacancy defects in the electronic and magnetic properties of Sr_3SnO: a first-principles study. *RSC Adv.*, 7(12):6880–6888, 2017.

[66] Y. Lee, F. Wu, R. Kumar, F. Hunte, J. Schwartz, and J. Narayan. Epitaxial integration of dilute magnetic semiconductor Sr_3SnO with Si (001). *Appl. Phys. Lett.*, 103(11):112101, 2013.

[67] Y. Lee, F. Wu, J. Narayan, and J. Schwartz. Oxygen vacancy enhanced room-temperature ferromagnetism in Sr_3SnO/c-YSZ/Si (001) heterostructures. *MRS Commun.*, 4(1):7–13, 2014.

[68] E. Haque and M. A. Hossain. First-principles study of mechanical, thermodynamic, transport and superconducting properties of Sr_3SnO. *J. Alloys Compd.*, 730:279–283, 2018.

[69] A. Widera and H. Schäfer. Das Zustandsdiagramm Sr-Sn und die verbindung Sr_3SnO. *J. Less-Common Met.*, 77(1):29–36, 1981.

[70] M. Aljarrah, A. Alkhazali, S. Obeidat, A. Almagableh, and M. Rababah. On Phase Equilibria of Sn-Sr and Mn-Sn-Sr Systems. *Jordan J. Mech. Ind. Eng.*, 8(6), 2014.

[71] A. Velden and M. Jansen. Zur Kenntnis der inversen Perowskite M_3TO (M= Ca, Sr, Yb; T= Si, Ge, Sn, Pb). *Z. Anorg. Allg. Chem.*, 630(2):234–238, 2004.

[72] M. Kirchner, W. Schnelle, and R. Niewa. Inverse Perovskites $(Eu_3O)E$ with E= Sn, In– Preparation, Crystal Structures and Physical Properties. *Z. Anorg. Allg. Chem.*, 632(4):559–564, 2006.

[73] Y. Okamoto, A. Sakamaki, and K. Takenaka. Thermoelectric properties of antiperovskite calcium oxides Ca_3PbO and Ca_3SnO. *J. Appl. Phys.*, 119(20):205106, 2016.

[74] D. Samal, H. Nakamura, and H. Takagi. Molecular beam epitaxy of three-dimensional Dirac material Sr_3PbO. *APL Mater.*, 4(7):076101, 2016.

[75] M. Minohara, R. Yukawa, M. Kitamura, R. Kumai, Y. Murakami, and H. Kumigashira. Growth of Antiperovskite Oxide Ca_3SnO Films by Pulsed Laser Deposition. *arXiv preprint arXiv:1710.03406*, 2017.

[76] Y. Obata, R. Yukawa, K. Horiba, H. Kumigashira, Y. Toda, S. Matsuishi, and H. Hosono. ARPES studies of the inverse perovskite Ca_3PbO: Experimental confirmation of a candidate 3D Dirac fermion system. *Phys. Rev. B*, 96(15):155109, 2017.

[77] S. Yonezawa, T. Higuchi, Y. Sugimoto, C. Sow, and Y. Maeno. Compact AC susceptometer for fast sample characterization down to 0.1 K. *Rev. Sci. Instrum.*, 86(9):093903, 2015.

[78] P. Blaha, K. Schwarz, G. K. H. Madsen, D. Kvasnicka, and J. Luitz. *WIEN2K, An Augmented Plane Wave + Local Orbitals Program for Calculating Crystal Properties*. Karlheinz Schwarz, Techn. Universität Wien, Austria, 2001.

[79] K. Sato, M. Ogura, H. Akai, Band Structure Calculation Using KKR-Greens Function Method, Aug 2008, URL http://kkr.issp.u-tokyo.ac.jp/.

[80] J. Korringa. On the calculation of the energy of a Bloch wave in a metal. *Physica*, 13(6-7):392–400, 1947.

[81] W. Kohn and N. Rostoker. Solution of the Schrödinger equation in periodic lattices with an application to metallic lithium. *Phys. Rev.*, 94(5):1111, 1954.

[82] J. P. Perdew, K. Burke, and M. Ernzerhof. Generalized gradient approximation made simple. *Phys. Rev. Lett.*, 77(18):3865, 1996.

[83] H. Shiba. A reformulation of the coherent potential approximation and its applications. *Progr. Theor. Phys*, 46(1):77–94, 1971.

[84] P. Soven. Application of the coherent potential approximation to a system of Muffin-Tin potentials. *Phys. Rev. B*, 2(12):4715, 1970.

[85] C. Michel, M. Hervieu, M. Borel, A. Grandin, F. Deslandes, J. Provost, and B. Raveau. Superconductivity in the Bi-Sr-Cu-O system. *Z. Phys. B*, 68(4):421–423, 1987.

[86] M.-K. Wu, J. R. Ashburn, C. Torng, P. H. Hor, R. L. Meng, L. Gao, Z. J. Huang, Y. Wang, and a. Chu. Superconductivity at 93 K in a new mixed-phase Y-Ba-Cu-O compound system at ambient pressure. *Phys. Rev. Lett.*, 58(9):908, 1987.

[87] H. Maeda, Y. Tanaka, M. Fukutomi, and T. Asano. A new high-T_c oxide superconductor without a rare earth element. *Jpn. J. Appl. Phys.*, 27(2A):L209, 1988.

[88] K. Ishida, H. Mukuda, Y. Kitaoka, K. Asayama, Z. Mao, Y. Mori, and Y. Maeno. Spin-triplet superconductivity in Sr_2RuO_4 identified by ^{17}O Knight shift. *Nature*, 396(6712):658–660, 1998.

[89] Y. Maeno, S. Kittaka, T. Nomura, S. Yonezawa, and K. Ishida. Evaluation of spin-triplet superconductivity in Sr_2RuO_4. *J. Phys. Soc. Jpn.*, 81(1):011009, 2011.

[90] E. Zintl and W. Morawietz. Orthosalze von Sauerstoffsäuren. *Z. Anorg. Allg. Chem.*, 236(1):372–410, 1938.

[91] H. Sabrowsky, K. Paszkowski, D. Reddig, and P. Vogt. Na_3OCl and Na_3OBr, the First Alkali Metal Chalcogenide Halides. *Z. Naturforsch. B Chem. Sci*, 19(19), 1988.

[92] M. Jansen. Neue Untersuchungen an Na_3NO_3. *Z. Anorg. Allg. Chem.*, 435(1):13–20, 1977.

[93] S. Sitta, K. Hippler, P. Vogt, and H. Sabrowsky. Kristallstruktur von gelbem K_3OBr. *Z. Anorg. Allg. Chem.*, 597(1):197–200, 1991.

[94] H. Sahrowsky, P. Vogt, K. Hippler, and S. Sitla. Crystal structure of K_3OI. *Z. Kristallogr. Cryst. Mater.*, 196(1-4):193–196, 1991.

[95] C. Feldmann and M. Jansen. Darstellung und Kristallstruktur von Cs_3ClO/Preparation and Crystal Structure of Cs_3ClO. *Z. Naturforsch. B*, 50(9):1415–1416, 1995.

[96] C. Feldmann and M. Jansen. Zur kristallchemischen Ähnlichkeit von Aurid-und Halogenid-Ionen. *Z. Anorg. Allg. Chem.*, 621(11):1907–1912, 1995.

[97] H. Sabrowsky, E. Feldbaum-Möller, K. Fischer, S. Sitta, P. Vogt, and V. Winter. Die Kristallstrukturen von α-und β-K_3OCl. *Z. Anorg. Allg. Chem.*, 622(1):153–156, 1996.

[98] C. Feldmann and M. Jansen. Zur Kenntnis Neuer ternärer Oxide mit anionischem Gold. *Z. Anorg. Allg. Chem.*, 621(2):201–206, 1995.

[99] Y. Zhao and L. L. Daemen. Superionic conductivity in lithium-rich anti-perovskites. *J. Am. Chem. Soc*, 134(36):15042–15047, 2012.

[100] C. Rohr. Crystal structure of calcium germanide oxide, Ca_3GeO. *Z. Kristallogr.*, 210(10):781–781, 1995.

[101] B. Huang and J. D. Corbett. Orthorhombic Inverse Perovskitic Ba_3TtO (Tt= Ge, Si) as Zintl Phases. *Z. Anorg. Allg. Chem.*, 624(11):1787–1790, 1998.

[102] C.-K. Chiu, Y.-H. Chan, X. Li, Y. Nohara, and A. Schnyder. Type-II Dirac surface states in topological crystalline insulators. *Phys. Rev. B*, 95(3):035151, 2017.

[103] L.-g. Liu and W. A. Bassett. Changes of the crystal structure and the lattice parameter of SrO at high pressure. *J. Geophys. Res.*, 78(35):8470–8473, 1973.

[104] P.-J. Chen and H.-T. Jeng. Phase diagram of the layered oxide SnO: GW and electron-phonon studies. *Sci. Rep.*, 5:16359, 2015.

[105] W. De Haas, J. De Boer, and G. Van den Berg. The electrical resistance of cadmium, thallium and tin at low temperatures. *Physica*, 2(1):453–459, 1935.

[106] A. Mackenzie, R. Haselwimmer, A. Tyler, G. Lonzarich, Y. Mori, S. Nishizaki, and Y. Maeno. Extremely strong dependence of superconductivity on disorder in Sr_2RuO_4. *Phys. Rev. Lett.*, 80(1):161, 1998.

[107] N. Werthamer, E. Helfand, and P. Hohenberg. Temperature and purity dependence of the superconducting critical field, H_{c2}. III. Electron spin and spin-orbit effects. *Phys. Rev.*, 147(1):295, 1966.

[108] Y. Lee, J. Narayan, and J. Schwartz. Tunable electronic structure in dilute magnetic semiconductor Sr_3SnO/c-YSZ/Si (001) epitaxial heterostructures. *J. Appl. Phys.*, 116(16):164903, 2014.

[109] G. Kresse and J. Hafner. Ab initio molecular dynamics for open-shell transition metals. *Phys. Rev. B*, 48(17):13115, 1993.

[110] G. Kresse and J. Furthmüller. Efficiency of ab-initio total energy calculations for metals and semiconductors using a plane-wave basis set. *Comput. Mater. Sci.*, 6(1):15–50, 1996.

[111] G. Kresse and J. Furthmüller. Efficient iterative schemes for ab initio total-energy calculations using a plane-wave basis set. *Phys. Rev. B*, 54(16):11169, 1996.

[112] G. K. Madsen, P. Blaha, K. Schwarz, E. Sjöstedt, and L. Nordström. Efficient linearization of the augmented plane-wave method. *Phys. Rev. B*, 64(19):195134, 2001.

[113] A. V. Krukau, O. A. Vydrov, A. F. Izmaylov, and G. E. Scuseria. Influence of the exchange screening parameter on the performance of screened hybrid functionals. *J. Chem. Phys*, 125(22):224106, 2006.

[114] P. E. Blöchl. Projector augmented-wave method. *Phys. Rev. B*, 50(24):17953, 1994.

[115] G. Kresse and D. Joubert. From ultrasoft pseudopotentials to the projector augmented-wave method. *Phys. Rev. B*, 59(3):1758, 1999.

[116] J. Vidal, X. Zhang, L. Yu, J.-W. Luo, and A. Zunger. False-positive and false-negative assignments of topological insulators in density functional theory and hybrids. *Phys. Rev. B*, 84(4):041109, 2011.

[117] M. Sato. Non-Abelian statistics of axion strings. *Phys. Lett. B*, 575(1):126–130, 2003.

[118] C. Fang, M. J. Gilbert, and B. A. Bernevig. New class of topological superconductors protected by magnetic group symmetries. *Phys. Rev. Lett.*, 112(10):106401, 2014.

[119] M. Sato. Topological properties of spin-triplet superconductors and Fermi surface topology in the normal state. *Phys. Rev. B*, 79(21):214526, 2009.

[120] M. Sato. Topological odd-parity superconductors. *Phys. Rev. B*, 81(22):220504, 2010.

[121] L. Fu and E. Berg. Odd-parity topological superconductors: theory and application to $Cu_xBi_2Se_3$. *Phys. Rev. Lett.*, 105(9):097001, 2010.

[122] S. Kobayashi and M. Sato. Topological superconductivity in Dirac semimetals. *Phys. Rev. Lett.*, 115(18):187001, 2015.

[123] B. T. Matthias, T. H. Geballe, and V. B. Compton. Superconductivity. *Rev. Mod. Phys.*, 35(1):1, 1963.

[124] B. Sahoo, W. Adeagbo, F. Stromberg, W. Keune, E. Schuster, R. Peters, P. Entel, S. Lüttjohann, A. Gondorf, W. Sturhahn, et al. Electronic transport and atomic vibrational properties of semiconducting $Mg_2{}^{119}Sn$ thin film. *Phase Transitions*, 79(9-10):839–852, 2006.

[125] A. Kokalj. Computer graphics and graphical user interfaces as tools in simulations of matter at the atomic scale. *Comput. Mater. Sci.*, 28(2):155–168, 2003.

[126] D. Wollman, D. Van Harlingen, W. Lee, D. Ginsberg, and A. Leggett. Experimental determination of the superconducting pairing state in YBCO from the phase coherence of YBCO-Pb dc SQUIDs. *Phys. Rev. Lett.*, 71(13):2134, 1993.

[127] D. J. Thompson, M. Minhaj, L. Wenger, and J. Chen. Observation of paramagnetic Meissner effect in niobium disks. *Phys. Rev. Lett.*, 75(3):529, 1995.

[128] A. Geim, S. Dubonos, J. Lok, M. Henini, and J. Maan. Paramagnetic Meissner effect in small superconductors. *Nature*, 396(6707):144–146, 1998.

[129] H. Walter, W. Prusseit, R. Semerad, H. Kinder, W. Assmann, H. Huber, H. Burkhardt, D. Rainer, and J. Sauls. Low-Temperature Anomaly in the Penetration Depth of $YBa_2Cu_3O_7$ Films: Evidence for Andreev Bound States at Surfaces. *Phys. Rev. Lett.*, 80(16):3598, 1998.

[130] S.-I. Suzuki and Y. Asano. Paramagnetic instability of small topological superconductors. *Phys. Rev. B*, 89(18):184508, 2014.

[131] S.-I. Suzuki and Y. Asano. Effects of surface roughness on the paramagnetic response of small unconventional superconductors. *Phys. Rev. B*, 91(21):214510, 2015.

[132] A. Di Bernardo, Z. Salman, X. Wang, M. Amado, M. Egilmez, M. G. Flokstra, A. Suter, S. L. Lee, J. Zhao, T. Prokscha, et al. Intrinsic Paramagnetic Meissner Effect Due to s-Wave Odd-Frequency Superconductivity. *Phys. Rev. X*, 5(4):041021, 2015.

[133] S. Chu, A. J. Schwartz, T. B. Massalski, and D. E. Laughlin. Extrinsic paramagnetic Meissner effect in multiphase indium-tin alloys. *Appl. Phys. Lett.*, 89(11):111903, 2006.

[134] H. Yasuoka, T. Kubo, Y. Kishimoto, D. Kasinathan, M. Schmidt, B. Yan, Y. Zhang, H. Tou, C. Felser, A. Mackenzie, et al. Emergent Weyl Fermion Excitations in TaP Explored by ^{181}Ta Quadrupole Resonance. *Phys. Rev. Lett.*, 118(23):236403, 2017.

[135] A. Svane and E. Antoncik. Theoretical investigation of the isomer shifts of the ^{119}Sn Mössbauer isotope. *Phys. Rev. B*, 35(10):4611, 1987.

[136] P. Lippens. Interpretation of the ^{119}Sn Mössbauer isomer shifts in complex tin chalcogenides. *Phys. Rev. B*, 60(7):4576, 1999.

[137] P. Lippens, J. Olivier-Fourcade, and J. Jumas. Interpretation of the 119 Sn Mössbauer parameters. *Hyperfine Interact.*, 126(1-4):137–141, 2000.